The Dissertation Committee for Jeong-Heon Shin Certifies that this is the approved version of the following dissertation:

Scale effects on the latent heat of phase change & the effect of dynamic contact angles on dynamic capillary pressure

Committee:

Mark R. Deinert, Supervisor

David G. Bogard

Li Shi

David DiCarlo

Halil Berberoglu

Scale effects on the latent heat of phase change & the effect of dynamic contact angles on dynamic capillary pressure

by

Jeong-Heon Shin, B.E.; M.S.E.

Dissertation

Presented to the Faculty of the Graduate School of

The University of Texas at Austin

in Partial Fulfillment

of the Requirements

for the Degree of

Doctor of Philosophy

The University of Texas at Austin

December 2014

Dedication

To my parents

Acknowledgements

I would like to express my gratitude and appreciation to Dr. Mark R. Deinert, my advisor and the chair of my Ph.D. committee. He has been resourceful, generous, and always encouraged me. In addition, his professional experience and knowledge has guided me to study profoundly and to be an engineer and scientist.

I would also like to express thank my committee members: Drs. David Bogard, Li Shi, David DiCarlo, and Halil Berberoglu for their valuable advice and help. Their input has helped to make my Ph.D. work stronger and more valuable.

Appreciation is also expressed to my lab members, Dr. Andrew Osborne, Dr. Geoff Recktenwald, Carlos Rios Perez, Andrew Gilbert, Brady Stoll, Tim Smith and Taehyung Kim whom I could talk with for constructive discussions of my research and theirs.

Lastly, I would like to thank my father, Dong-Young Shin and mother, Tae-Joo Suh who supported and encouraged me to keep working without hesitation. They also have showed endless love and have been sacrificing at all levels for me to complete my Ph.D. study. My sisters have been also been supporters and filled my role in my family.

Scale effects on the latent heat of phase change
& the effect of dynamic contact angles on dynamic capillary pressure

Jeong-Heon Shin, Ph.D.
The University of Texas at Austin, 2014

Supervisor: Mark R. Deinert

Surface tension is an important material property that affects the behavior of micro/nano size thermal-fluid systems. In this dissertation, I investigate how surface tension affects the latent heat of a phase change in nanoscale systems as well as on the movement of water in microstructures.

Classical thermodynamic models were developed to describe how the latent heat of melting in nano-pores depends on scale and were extended to the melting of metallic nano-particles. The results from these models were verified by comparison with experimental data from the open literature for hydrocarbons and water in nano-size pores, as well as for free standing metallic nano particles.

A classical thermodynamic model was also developed to describe how the latent heat of vaporization depends on scale. This was verified experimentally

using a Thermogravimetric Analysis/Differential Scanning Calorimeter available in the core facilities of the Texas Materials Institute. This verified that the latent heat of vaporization for water confined nano-pores decreases with pore size.

A model for dynamic capillary pressure in porous media was analyzed using experimentally derived data for the velocity dependent contact angle of water on SiO_2 glass. The data were derived from images of microfluidic flows in capillary tubes, obtained using high speed digital microscopy.

Table of Contents

List of Tables ..... **x**
List of Figures ..... **xiii**
Chapter 1. Introduction **1**
Chapter 2. Scale effects in the latent heat of melting in nanopores **5**
2.1. Abstract 5
2.2. Introduction 5
2.3. Methods 8
2.4. Results and Discussion 13
Appendix: Heat of melting for a droplet in a closed system at constant pressure 17
Supplemental Information 18
Chapter 3. A model for the latent heat of melting in free standing metal nanoparticles **39**
3.1. Abstract 39
3.2. Introduction 39
3.3. Methods 41
3.4. Results and discussion 48
Supplemental Information 52
Chapter 4. Water's latent heat of vaporization changes with scale **64**
4.1. Abstract 64
4.2. Introduction 64
4.3. Method 70
4.4. Results and Discussion 73
Supplemental information 76
Chapter 5. Non-equilibrium capillary pressures and flow field stability in porous media **94**
5.1. Abstract 94

5.2. Introduction 95
5.3. Capillary pressure in a porous medium with moving contact lines 97
5.4. dependence of capillary pressure on contact line velocity 101
5.5. Results and discussion 107
Supplemental information 112
Chapter 6. Conclusion 122
Bibliography 124

List of Tables

Table 2.S1. Ratios of molar surface tension to molar heat of melting and molecular weight (MW) [62]. 19

Table 2.S2. Surface tension of benzene as a function of temperature. The heat of melting was given in [63], molar solid density (or specific volume) are from [64]. The surface tension is calculated by using Equation (2.S1). The curve fit of the surface tension for heptane is given by $\sigma_{sl} = -2.58x10^{-4}T + 9.49x10^{-2}$. **..... 20**

Table 2.S3. Surface tension of heptane as a function of temperature. The heat of melting was given in [65], molar solid density (or specific volume) are from [64]. The surface tension is calculated by using Equation (2.S1). The curve fit of the surface tension for heptane is given by $\sigma_{sl} = -2.11x10^{-4}T + 6.21x10^{-2}$**. 21**

Table 2.S4. Surface tension of naphthalene as a function of temperature. Heat of melting was given in [66], solid density (or specific volume) are from [67]. The curve fit of the surface tension for naphthalene is given by $\sigma_{sl} = -3.06x10^{-4}T + 1.39x10^{-2}$. **..... 22**

Table 2.S5. Solid-liquid surface tension of Ice as a function of temperature [68]..... 23

Table 2.S6. Change in the heat of melting for benzene: The theoretical values calculated by Eq. (2.10) and the adjusted experimental results [69] change as the diameter of droplet varies. Both values at $100*10^{-9}$ (m) are shifted to 0 under the assumption that 100nm pore has the same latent heat of melting as bulk state. **.. 25**

Table 2.S7. Change in the heat melting for heptane: The theoretical change in heat of melting calculated by Equation (2.10) and the adjusted experimental results [69] change as the diameter of droplet varies. Both values at $100*10^{-9}$ (m) are

shifted to 0 under the assumption that 100nm pore has the same latent heat of melting as bulk state. **26**

Table 2.S8. Change in the heat of melting for naphthalene: Theoretical values calculated by Equation (2.10) and the adjusted experimental results [69] change as the diameter of droplet varies. Both values at $100*10^{-9}$ (m) are shifted to 0 under the assumption that 100nm pore has the same latent heat of melting as bulk state**.** **28**

Table 2.S9. Change in the heat of melting for ice (H_2O): Theoretical values calculated by Equation (2.10) and the experimental results for small pore diameter [6] and for large pore diameter [74] change as the diameter of droplet varies. Both values at $100*10^{-9}$ (m) are shifted to 0 under the assumption that 100nm pore has the same latent heat of melting as bulk state..... **30**

Table 2.S10. Several necessary parameters used in Eq. (2.S3). h is C-H bond length [76], and S_b is entropy with E_o and T_b, bulk solid-vapor transition enthalpy and temperature..... **32**

Table 3.S1. Solid, liquid density and specific volume for Aluminum and Tin [97-103]. **55**

Table 3.S2. Surface energies with temperature variation. Here σ_{lv} is the liquid-vapor surface tension for aluminum metal and is computed using Eq. (3.S15). The solid-vapor surface tension for Al_2O_3, σ_{sv}, is computed using Eq. (3.S16). The surface tension of the solid-liquid metal interface, σ_{ol}, is calculated using Eq. (3.S14). Equation (3.S13) is used to compute *W*. **58**

Table 3.S3. Properties for aluminum, tin, and aluminum oxide for Eq. (3.S17). Here *IR* is the atomic diameter [106, 107], H_{LV} is the latent heat of vaporization [108, 109], T_b is boiling point, and S_b is the entropy..... **59**

Table 3.S4. Latent heat of melting of tin particle: Theoretical values calculated by Eqs. (3.9, 11) and the experimental results [7]. **62**

Table 3.S5. Latent heat of melting of aluminum particle: Theoretical values calculated by Eqs. (3.9,12) and the experimental results [8]. **63**

Table 4.S1. Properties for water for Eq. (4.S17). IR is the atomic diameter, H_{LV} is the latent heat of vaporization of bulk water, T_b is boiling temperature, and S_b is the entropy. **79**

Table 4.S2. The specifications for CPG. **81**

Table 4.S3. Specific heat of water [124]. **88**

Table 4.S4. Specific heat of glass [103]. **89**

Table 4.S5. Latent heats of vaporization and error. This table shows experimental results for the latent heats of vaporization and calculated errors for five different sizes of radii. **93**

List of Figures

Figure 2.1 Experimental values and theoretical best fit graphs for heptane, benzene, naphthalene and water. Experimental data from [5] and the best fit of Eq. (2.9). The R^2 values for heptane, benzene, naphthalene and water are 0.96, 0.99, 0.98, and 0.94 respectively. The corresponding Tolman lengths are $7.5x10^{-11}$, $1.5x10^{-10}$, $2.1x10^{-10}$ and $-1.9*10^{-10}$ respectively. **16**

Figure 2.S1. R^2 value for benzene according to Tolman length: A value of d= $3.0*10^{-10}$ yields the highest R^2 = 0.99. ..... **25**

Figure 2.S2. R^2 value for heptane according to Tolman length: A value of d= $1.5*10^{-10}$ (m) yields the highest R^2 =0.96. ..... **27**

Figure 2.S3. R^2 value for naphthalene according to Tolman length: A value of d=$4.1x10^{-11}$, yields the highest R^2 =0.98. ..... **29**

Figure 2.S4. R^2 value for water/ice according to Tolman length: A value of d=-$3.7\ x10^{-10}$, yields the highest R^2 =0.94. ..... **31**

Figure 2.S5. Tolman length of Benzene as a function of pore diameter. The averaged Tolman length is 1.09×10^{-10} **33**

Figure 2.S6. Tolman length of Heptane as a function of pore diameter. The averaged Tolman length is 1.11×10^{-10}. **34**

Figure 2.S7. Tolman length of Naphthalene as a function of pore diameter. The averaged Tolman length is 1.09×10^{-10}. **35**

Figure 2.S8. This figure shows the change in latent heat for Benzene with the calculated Tolman length, 1.09×10^{-10}, and R^2 = 0.92. ..... **36**

Figure 2.S9. This figure shows the change in latent heat for Heptane with the calculated Tolman length, 1.11×10^{-10}, and R^2 = 0.97. ..... **37**

Figure 2.S10. This figure shows the change in latent heat for Naphthalene with the calculated Tolman length, 1.09 x 10^{-10}, R^2 =0.70. ..... **38**

Figure 3.1. This schematic shows solid particle and its liquid layer. Figure (a) is for Tin particle. Tin particle is covered with its liquid layer, 1.6 nm [18] and Figure (b) is for aluminum particle. Aluminum particle is covered with aluminum oxide layer (Al_2O_3) and liquid aluminum exists between aluminum core and aluminum oxide. **43**

Figure 3.2. Experimental data for tin is from S.L. Lai et al [18] and calculated result fit well. The averaged Tolman length is 3.73 x 10^{-10} computed using Eq. (3.10). **49**

Figure 3.3. Experimental data for aluminum is from Sun and Simon (2007) [19] calculated result fit well. The average Tolman length of aluminum is 3.11x10^{-11} and the averaged Tolman length of aluminum oxide is 5.03x10^{-11}, computed with Eq. (3.10). **50**

Figure 3.S1. Tolman length as a function of particle diameter. The figure shows how the parameter *d* varies with particle diameter for aluminum metal, α-Al_2O_3, and tin as a function of particle diameter. Dashed lines show the predictions of Eq. (3.S18), solid lines show the average value over the diameter range. The diameter ranges correspond to the ranges in the data for tin and aluminum particles in [9,10]. Here Tolman lengths, *d* are 3.11 x10^{-10}, 5.03 x10^{-11}, and 3.73 x10^{-10} for aluminum, α-Al_2O_3, and tin, respectively. **60**

Figure 4.1. Nanoporous matrix. (a) Scanning Electron Micrograph of 130 nm nanoporous glass. The pores are capillary channels of a given diameter. (b) Schematic of water confined in a capillary. Evaporation takes place from the ends. **66**

Figure 4.2. Heat fluxes given to the sample. This graph shows the heat flux supplied to the sample, 33nm CPG. For the calculation of $h_{lv,confined}$, in Eq. 4.10, the heat after about 900 seconds was used where bulk and confined water vaporize together. **73**

Figure 4.3. Experimental result and theoretical model. Tolman length is -4.7x10^{-11} [123] and liquid thickness is 2.75x10^{-10}. **75**

Figure 4.S1. Tolman length as a function of pore diameter. This figure shows the variation of the Tolman length of water with the pore diameter change. Equation (4.S17) is used to calculate Tolman length with properties in Table 4.S1. ..... **80**

Figure 4.S2. Simple chamber to induce water condensation in pores of CPG. In the chamber, distilled water was vaporized by heating to make high humidity in the chamber at one side and dried CPG was put in small beaker cooling to induce the condensation in the pores and around them for 5 hours. **82**

Figure 4.S3. This figure shows x93901 magnified images for evaporation from 130 nm CPG. By changing pressure from 4.85 Torr. To 4.70 Torr. at 4C, the relative humidity changes from 98.5 % to 95.6 %. From this image, it is possible to see in-situ evaporation from the CPG particle. (VP: Vapor Pressure, RH: Relative Humidity)..... **83**

Figure 4.S4. Schematic of the sample with prepared CPG. The 70 ml alumina crucible was filled with the CPG with water (confined and bulk water). **84**

Figure 4.S5. Mass change of water in the crucible in percentage (%). The slope is not straight because of the change of the exposed area of water being vaporized. This data is for 33 nm CPG. **86**

Figure 4.S6. Reference temperature (^{o}C) in red and sample temperature (^{o}C) in blue in the chamber of the TGA system. Red line, setting temperature

increases linearly and maintains set temperature. Blue line, sample temperature follows the trend of the setting temperature, but there is a gap between two temperatures because of the conductivity, and vaporization process of the sample. This data is for 33 nm CPG. **87**

Figure 5.1. Interfacial movement. The projected area, A_p, is shown. Here the contact line force is in the *i* direction and the movement of the interface is in the *k* direction. **96**

Figure 5.2. Experimental set up to measure the interface angle of water flow in micro glass tube. **101**

Figure 5.3. Interface angle vs. velocity of water front from the capillary glass experiment. The curve fit is ø = 30 + 50.08 v $^{0.13}$, where v is in {cm/s}. **102**

Figure 5.4. This figure shows the data from Hoffman [139], advance model [153] and measured angle. For the comparison, viscosity h is 0.001 {Pa.s}, surface tension of water s is 0. 072 {N/m}. And 0.04 was used for $F(q_s)$ of measured angle and advanced model [153]. **104**

Figure 5.5. Wetting front profile in a constant velocity finger. The saturation profile for a finger that was moving through 20/30 sieve SiO_2 sand at 0.19 cm/sec. **105**

Figure 5.6. Dynamic and equilibrium capillary pressures. The dynamic capillary pressure was determined using numerical integration of Darcy's law along the centerline of a preferential flow field that was infiltrating into dry SiO_2 sand at constant velocity. Wetting front velocity and flow field moisture content were measured non-invasively using real-time neutron radiography, as was the hydraulic conductivity of the medium. The dynamic capillary pressure drops abruptly across the leading edge of the wetting front, reaches a minimum at between S ~

0.5, and then begins to rise again. The equilibrium capillary pressure drops monotonically. 109

Figure 5.7. Interfacial velocity as a function of saturation. 110

Figure 5.8. Dynamic Capillary pressure. Predicted dynamic capillary pressure and measured capillary pressure shows agreement. Predicted capillary is the sum of equilibrium capillary and dynamic term. 111

Figure 5.S1. Equilibrium capillary pressure and the best fit of the van Genutchen model graphs. Equilibrium capillary pressure data from [19]. 113

Figure 5.S2. Cross sectional pore area distribution. The cross section area distribution was determined using a capillary rise experiment and πr^2. 114

Figure 5.S3. Wetting front profile in a constant velocity finger. A generalized logistic function was fit to the data and used to compute dS/dz. The fit has an R^2 = 0.98. 116

Figure 5.S4. Original image is altered to binary numbered image. Left figure is original image from the microscope program. The image is altered to binary numbered matrix as shown in right figure with Matlab. 117

Figure 5.S5. Boundary tracing. The Matlab function 'bwtraceboundary' is used to trace the interfacial boundary. Left figure is binary picture showing interfaces and right figure has green lines drawn by 'bwtraceboundary' command. 118

Figure 5.S6. Linear fit. Green lines drawn by 'bwtraceboundary' are altered to linear squared fir lines on right figure. 119

Figure 5.S7. Velocity dependent contact angle. The curve fit is ø = 30 + 50.08 v $^{0.13}$, where velocity is in {cm/s}. 120

Figure 5.S8. Calculated tdS/dt vs. Saturation. 121

Chapter 1. Introduction

A fundamental property of materials, the latent heat of phase change affects processes that range in scale from the global hydrological cycle [1] to the storage of spent nuclear fuel, the nucleation of crystals, and the manufacture of nano-scale structures [2, 3]. At the micro and nanoscale, material interfaces can have a significant effect on material behavior. In fact, it has been known that thermodynamic properties for small scale materials could be different from those in bulk state since 1871 when Lord Kelvin showed that the curvature of a fluid interface affects its vapor pressure [4].

In the past two decades, as technologies have advanced dramatically, the sizes of the structures in electric devices has decreased to nano-scale [2, 3]. Size dependent thermodynamic properties are important for accurate manufacture of nano scaled structures. Melting point depression and changes to the latent heat of melting for materials confined in small scaled structures have been observed experimentally since the 1990's [5, 6]. These studies showed that melting points, as well as latent heats of melting, can decrease dramatically for particles confined in pores less than 100 nm in diameter. In addition, the melting behavior of free standing metallic nano particles has also been shown to be affected by particle

size [7, 8]. However, attempts to explain these experimental observations have been unsuccessful.

Using a first order analysis based on the Kelvin and Clausius-Clapeyron equations, Defay and Prigogine [9] showed that material scale will also affect the vaporization of liquids confined in nano pores. However, the derivation assumes that the Clausius-Clapeyron equation holds for systems where surface energies play a role, and this is only approximately true. Importantly, very little experimental data is available to verify this result or with which to develop more accurate models.

Another area in which material interfaces play a critical role is capillary pressure, whose effect on fluid movement in micro-capillary systems has been studied extensively [10-12]. For flow in micro-size channels, the first theoretical work dates to at least 1921 and the work of Washburn [13] which described the movement of fluid as a function of time. For flow in porous media it is typically assumed that capillary pressures take on equilibrium values, regardless of how quickly the flows move. However, Weitz et al. [12] showed that non-equilibrium capillary pressures can arise when fluid interfaces are in motion. Hassanizadeh and Gray [11] and Deinert et al. [10] later suggested thermodynamic models to explain non-equilibrium capillary pressure in porous media. However, these models have never been tested against experimental data. Importantly, their implementation also requires an expression for the force required to move

interfacial contact lines in porous systems. Such models are also missing from the literature. Non-equilibrium capillary pressures are thought to play an important role in the onset of wetting front instability in porous systems, and accurate models to describe these pressures are needed.

Chapters 2-5 each deal with a different aspect of how interfacial surface tension affects thermodynamic behavior at the micro and nano scale. These chapters are written in paper format, and the first two have already been published in the Journal of Chemical Physics. Chapters 4 and 5 are being finalized for submission. Chapter 2 details a model derived to explain the change in the latent heat of melting of hydrocarbons and water confined in nanopores and its fit to experimental data from the open literature. This work has been published (Shin, J-H, J-Y Parlange, MR Deinert: Scale effects in the latent heat of melting in nanopores. *Journal of Chemical Physics,* 139, 044701, 2013). Chapter 3 details a model derived to predict changes in the latent heat of melting of free standing metal nanoparticles and its comparison to experimental data from the open literature. The model specifically takes into consideration different types of surface structures for the metallic nanoparticles. This work has been published (Shin, J-H, MR Deinert: Predicting scale effects in the latent heat of melting of metallic nanoparticles. *Journal of Chemical Physics*, 140, 164707, 2014). Chapter 4 details a model derived to predict the change in the latent heat of vaporization for fluids contained in nanopores and is directly extendable to nanoscale particles.

Data obtained for water confined in nanoporous glass, and using instruments at the Texas Materials Institute, were used to verify the model. Chapter 5 details the development of a model for non-equilibrium capillary pressure in terms of the force required to move interfacial contact lines. Data on contact line dynamics was obtained using high speed digital microscopy. The predictions of the model are compared to published data on non-equilibrium capillary pressures in the wetting front region of preferential flow paths. Chapter 6 gives a brief overview of future directions.

Chapter 2. Scale effects in the latent heat of melting in nanopores[†]

2.1. ABSTRACT

The curvature of a liquid vapor interface has long been known to change the equilibrium vapor pressure. It has also been shown that a capillary structure will affect the temperature at which both freezing and vaporization of a substance will occur. However, describing interfacial effects on the latent heat of a phase change has proven more difficult. Here we present a classical thermodynamic model for how the latent heat of melting changes as the size of the particles undergoing the transition decrease. The scale dependence for the surface tension is taken into consideration using a Tolman length correction. The resulting model is tested by fitting to published experimental data for the latent heat of melting for benzene, heptane, naphthalene and water contained in nano-porous glass. In all cases the model fits the data with an $R^2 \geq 0.94$.

2.2. INTRODUCTION

The energy required for a liquid to undergo a phase change affects processes that range in scale from the global hydrological cycle to the nucleation of crystals [e.g. 1, 14]. While considerable research has gone into explaining how

[†] The contents in this chapter were published in Journal of Chemical Physics: Shin, J-H, J-Y Parlange, MR Deinert., " Scale effects in the latent heat of melting in nanopores", Journal of Chemical Physics, 2013, 139, 044701.

a capillary interface will affect fluid pressure [e.g. 15, 16-21] the subject of how phase change is affected has received considerably less attention. Application of the Kelvin equation to droplets, and liquids that are contained within porous structures, has shown that the vapor pressure at which condensation occurs is dependent on the curvature of the capillary interface [e.g. 22, 23-25]. It has also been established that capillary structures can dramatically limit the ability of a liquid to boil, or cavitate, relative to what would be expected in the bulk substance, though the exact mechanisms for this are still under investigation [e.g. 14, 26]. That surface effects can depress the melting temperature of materials at small scale has itself been known for over one hundred years. More recently, phase change behavior in nanopores has been used to estimate surface forces and their scale dependence [27, 28].

The heat of phase change is assumed to be a constant in numerous thermodynamic relationships that are applied to nano-scale materials and systems (notably the Clausius-Clapeyron equation, Gibbs-Thompson equation and the Van't Hoff equation). However, experimental work has shown that the latent heat of liquid-solid phase changes can be affected by scale [29-35]. It is known that many materials exhibit a liquid surface layer at the nano-scale that does not solidify [30, 35], though the effect that this has on measurements is not by itself able to fully account for the observations [5, 35]. Several semi-empirical relationships have been suggested to explain the phenomena [32, 33]. Because a

capillary interface affects the free energy of a substance, it will also affect the interfacial stability criteria, and this needs to be considered in models for the latent heat of melting.

In the present contribution we present a classical thermodynamic analysis for how the latent heat of melting of a substance depends on its scale. We consider a spherical particle that melts at externally constant pressure, and show how the heat of phase change varies with the size of the particle. The scale dependence for the surface tension is taken into consideration using a Tolman length. A closed form result is given for how the heat of melting for substances varies with particle size. We verify our result using published data on the heat of melting for benzene, heptane, naphthalene and water contained within nano-scale pores. Estimates for the Tolman lengths for these substances are obtained by fitting the model to experimental data. While the results are derived for the melting of solid particles, they can easily be extended to describe the change in the heat of vaporization of liquid drops and fluids that are contained within a capillary structure where the fluid is under tension instead of compression (as is the case in drops and small particles). The classical model for why and how the latent heat of phase change in nanopores depends on scale and extends the thermodynamic description small scale phenomena developed Hill, Tolman and others [36, 37].

For Tolman the length, Gibbs showed that surface tension depends on the pressure, P, temperature T, and composition of the two coexisting bulk phases. He

also suggested that surface tension would change when the diameter D of the droplets falls below 100 nm based on statistical mechanical consideration. Based on the definition given by Gibbs, Tolman showed that surface tension varies with droplet size if the radius R_s of surface tension of the droplet does not coincide with the equimolar radius R_e. He estimated the Tolman length d, the separation between the equimolar surface and the surface tension, $d = R_e - R_s$ [38].

2.3. METHODS

The heat of melting of a spherical droplet of a pure solid substance that is in contact with its liquid phase at constant temperature and pressure is given by (Appendix):

$$q = h_l - h_s + v_s \frac{2\sigma}{r} \qquad (2.1).$$

Here, q is the latent heat of melting {J/g}, h_l is the specific enthalpy of the pure liquid {J/g}, h_s is the specific enthalpy of the solid phase with which it is in equilibrium {J/g}, v_s is the specific volume of the fluid {m^3/g}, σ is the interfacial surface tension {J/m^2}, and r is the radius of the particle {m}. For isothermal, isobaric phase change when interfacial effects can be ignored, Eq. (2.1) reduces to the well known result that $h_{ls} = Ts_{ls}$, where $h_{ls} = h_l - h_s$, T is temperature {K}, and

$s_{ls}=s_l-s_s$ is the difference in the specific entropies {J/g•K} on either side of the phase boundary [39]. However, when curvature is added to a liquid-solid interface it causes a pressure differential between the phases that will affect q. If the enthalpy of the liquid phase remains fixed (constant temperature and pressure), and that of the solid increases, the enthalpy of phase change would decrease. Similarly, if the enthalpy of the solid decreases while that of the liquid phase remains fixed, the enthalpy of phase change would increase.

The most direct approach to understanding the effect of interfacial curvature on the enthalpy of phase change is then to determine the net enthalpy change within the respective phases relative to that of bulk material. It is typical that a mono or bi-layer of adsorbed material remains unfrozen in micro and nano-scale pores for many, it not most, substances [30] and we make this assumption here. It is this unfrozen absorbed layer with which the frozen solid interacts. Importantly, this interaction is taken into consideration with the surface tension for the substance in contact with its own liquid. The surface energy of the unfrozen layer in contact with the pore wall is present in both the frozen and unfrozen states and, as a result, does not affect the latent heat of the phase change.

For analysis of a two phase system where a particle is in contact with its saturated liquid we follow Kondepudi and Prigogine, 1998 [40] and define the system's internal energy using:

$$dU = TdS - p_l dV_l - p_s dV_s + \sigma dA \qquad (2.2).$$

Here U is the internal energy of the system {J}, T is the temperature {K}, S is its entropy {J/K}, p_l is the pressure in the liquid phase {Pa}, V_l is the volume of the liquid phase {m^3}, p_s is the pressure in the solid phase {Pa}, V_s is the volume of the solid phase {m^3}, and A is the surface area of the solid {m^2}. Note in Eqs. (2.1) and (2.2) that we adopt the convention that extensive quantities and intensive quantities are denoted by upper and lower case symbols respectively. The effect of surface tension can be counted on either the solid or the liquid side and we use the convention of counting it in the former. We also make the simplification that the entropy of the interface is counted with the solid phase. Because the liquid and solid phases interact only through the interface, we can separate Eq. (2.2) into its phase components and it can be shown that the enthalpy of the solid is given by:

$$dH_s = V_s dp_s + TdS_s + \sigma dA \qquad (2.3).$$

Here H_s is the enthalpy of the solid {J}, and S_s is its entropy {J/K}. Equation (2.3) can then be integrated to find the change in fluid enthalpy, ΔH_s:

$$\Delta H_s = \int_{p_0}^{p_0+P_c} V_s dp_s + \int_{S_0}^{S} TdS_s + \int_{0}^{A} \sigma dA \qquad (2.4).$$

At small scale it is known that the surface tension of a substance can vary with radius of a particle. To first order that variation is given by:

$$\sigma = \sigma_0(1-d/r) \qquad (2.5),$$

where σ_0 is the bulk surface tension and d is two times the Tolman length [e.g. 36, 41].

For a constant temperature process where the substance can be assumed to be an incompressible spherical particle, Eq. (2.4) then yields:

$$\Delta h_s = v_s P_c + T\,\Delta s_s + \frac{3v_s\sigma_0}{r} - \frac{6v_s\sigma_0 d}{r^2} \qquad (2.6).$$

Here, Δh_s is the change in specific enthalpy of the solid particle {J/g}, Δs_s is the change in specific entropy of the solid {J/g•K} and P_c is the pressure change across the interface between the liquid and solid {Pa}. The change in entropy is itself given by $\Delta S_s = -(\partial\Delta G/\partial T)_{p,A}$, where ΔG can be obtained from the Gibbs potential {J} for the fluid:

$$dG_s = V_s dp_s - S_s dT + \sigma dA \qquad (2.7).$$

For a constant temperature process, dT is zero and integration of Eq. (2.7) then gives the same first and third terms as those on the right hand side of Eq. (2.4). Combining results we arrive at:

$$\Delta h_s = v_s P_c + \frac{3v_s\sigma}{r} - \frac{6v_s\sigma d}{r^2} - T(P_c\frac{dv_s}{dT} + \frac{3v_s}{r}\frac{d\sigma_0}{dT} - \frac{6v_s d}{r^2}\frac{d\sigma_0}{dT}) \qquad (2.8).$$

Finally, the total change in the enthalpy of melting is given by $\Delta q = \Delta h_l - \Delta h_s + v_s 2\sigma/r$. If we assume that the liquid phase is comprised of an ideal liquid, then for a constant temperature process, $\Delta h_l = 0$. Taking $P_c = 2\sigma/r$, then we get:

$$\Delta q = -\frac{3v_s\sigma}{r} + \frac{6v_s\sigma d}{r^2} + T(P_c\frac{dv_s}{dT} + \frac{3v_s}{r}\frac{d\sigma_0}{dT} - \frac{6v_s d}{r^2}\frac{d\sigma_0}{dT}) \qquad (2.9).$$

When liquids freeze in nanoscale pores, a layer of material often remains unfrozen at the pore surface [30]. In situations such as this, the r in Eq. (2.9) is not the radius of pore, but the radius of the frozen particle within the pore (i.e. $r = r_p - t$, where r_p is the pore radius and t the thickness of the unfrozen layer).

Data for the scale dependence of the latent heat of melting is given for seven organic substances are given in [5] and the values for napthalene are consistent with other available measurements [e.g. 33]. Data for water are from [42, 43]. Equation (2.9) requires data on solid-liquid surface tensions as well as solid densities, both as a function of temperature. These data are typically difficult

to find, especially when one is confined to substances for which the scale dependent latent heat of melting is also known. Various relationships have been proposed for estimating the dependence of surface tension on temperature with several authors suggesting a general form [e.g. 44, 45]:

$$\sigma_{sl} = \phi \left(\frac{V_s}{N_0} \right)^{1/3} \left(\frac{\Delta H_{Mf}}{V_s} \right) \qquad (2.10).$$

Here, N_o is Avogadro number (6.02×10^{23}/mol), V_s is molar solid volume {m^3/mol}, ϕ is a substance dependent constant, and ΔH_{Mf} is molar heat of melting {J/mol}. Applicable data for V_s, ΔH_{Mf} and ϕ for benzene, heptane and naphthalene were found in [46-51]. Equation (2.9) was fit to experimental data from [5] by varying d to maximize the correlation coefficient, R^2. Additional details and tabulated values can be found in the supplementary material [52].

2.4. Results and Discussion

Equation (2.9) shows that the scale dependence for a substance's latent heat of melting is driven by the effects of surface energy and entropy. Importantly, the result also provides convenient means by which to measure the Tolman length using data from nanoscale calorimetry. Equation (2.5) is a common approximation to full scaling relationship that Tolman proposed. However, it assumes that interfacial curvature can be defined by a particle radius and this ignores the type of surface roughness or irregularity that would likely exist for the

surface of nanoparticles. Despite this, the scaling relationship has been shown to work well for some nanocrystals [53]. Importantly, when a layer of material remains unfrozen at the pore surface, [30] the r in Eq. (2.9) is no longer the radius of the pore, but the radius of the pore minus the thickness of the surface layer.

The first term in Eq. (2.9) is dominant for heptane, benzene, naphthalene and water, with the terms containing d becoming increasingly important at small scale. Figure 2.1 shows the results of Eq. (2.9) against experimental data. The results show a very strong correlation ($R^2 \geq 0.96$) between experiment and theory for benzene, heptane and naphthalene when an optimal value for the Tolman length are used ($1.5x10^{-10}$, $7.5x10^{-11}$, $2.1x10^{-11}$ {m} respectively). Estimates for Tolman lengths range from as little as a few hundredths of a molecular diameter [54] to experimentally obtained values of a few molecular diameters [36] and the values found here are ~ 0.19, 0.28 and 0.35 molecular diameters respectively [55, 56]. The correlation between model and experimental results for water is also strong ($R^2 = 0.94$) with a Tolman length of $-1.9 x10^{-10}$.

In the present study we assume a spherical pore and particle geometry, which is unlikely to have been strictly true for the data presented in [5]. The assumption of spherical or cylindrical pores is, however, common in analytical formulations of capillary effects [22, 30, 57], and the degree to which the present model correlates to the available experimental data suggests that the assumptions are reasonable. It is possible that when Eq. (2.9) is fit to experimental data, that d

is also capturing the effects of irregular surface geometry within the pores. Roughness would tend to increase the surface area to volume ratio, increasing the effective surface energy. This could explain why the optimal value of d is negative for the water-ice interface. However, the sign of the Tolman length remains an open question with different studies suggesting positive or negative values depending on conditions and substance [54, 58, 59]. It is also possible that the negative Tolman length for water given here is an artifact of Eq. (2.9) being fit to data from two separate experimental systems with slightly different responses.

The derivation given here gives a classical thermodynamic analysis of why the latent heat of melting changes as the scale of substance is reduced. In particular, Eq. (2.9) gives a closed form result for how the latent heat of phase melting changes as the size of spherical particles is reduced. The number of substances for which the inputs to Eq. (2.9) are available, and for which scale dependent change in the heat of melting has been measured, is small. However, the model presented here fits the results for substances (both organic and inorganic) for which these data are available.

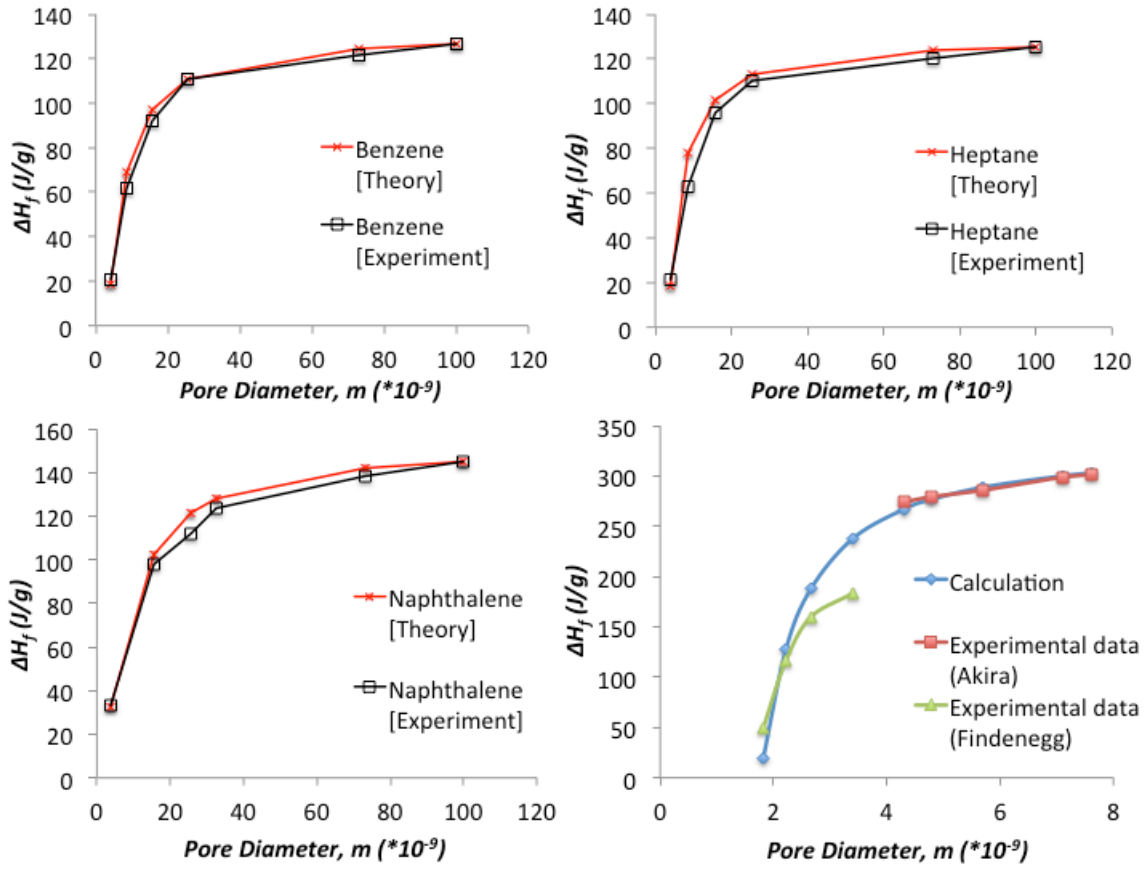

Figure 2.1 Experimental values and theoretical best fit graphs for heptane, benzene, naphthalene and water. Experimental data from [5] and the best fit of Eq. (2.9). The R^2 values for heptane, benzene, naphthalene and water are 0.96, 0.99, 0.98, and 0.94 respectively. The corresponding Tolman lengths are 7.5×10^{-11}, 1.5×10^{-10}, 2.1×10^{-10} and -1.9×10^{-10} respectively.

APPENDIX: HEAT OF MELTING FOR A DROPLET IN A CLOSED SYSTEM AT CONSTANT PRESSURE

Equation (2.1) is easily derived for a spherical particle that is contact with its liquid phase, at constant temperature and pressure in a closed system.

From the first law of thermodynamics, we have

$$Q = \Delta U + p_l \Delta V \tag{2.A1}$$

where U is the internal energy of the system (solid and liquid) and V is its total volume, Fig. 1. Assuming complete melting of a mass, m {g},

$$\Delta U = mu_l + mu_s \tag{2.A2}$$
$$\Delta V = \Delta V_l + \Delta V_s \tag{2.A3}$$
$$\Delta V_l = mv_l \tag{2.A4}$$
$$\Delta V_s = -mv_s \tag{2.A5}$$

Therefore,

$$Q = mu_l - mu_s + mp_l v_l - mp_l v_s \tag{2.A6}$$

So,

$$q = h_l - u_s - p_l v_s \tag{2.A7}$$

For a spherical mass,

$$p_l = p_s - 2\sigma/r \tag{2.A8}$$

Therefore,

$$q = h_l - u_s - p_s v_s + v_s 2\sigma/r \tag{2.A9}$$

Hence,

$$q = h_l - h_s + v_s 2\sigma/r \tag{2.A10}$$

SUPPLEMENTAL INFORMATION

Liquid-solid surface tensions and densities. Equation (2.9) requires data on solid-liquid surface tensions as well as solid densities, both as a function of temperature. However, these data are typically difficult to find. Various relationships have been proposed for estimating the dependence [60, 61] , with variants on following form having found wide application:

$$\sigma_{sl} = \phi\left(\frac{V_s}{N_o}\right)^{1/3}\left(\frac{\Delta H_{Mf}}{V_s}\right) \tag{2.S1}.$$

Here σ_{sl} is the solid-liquid surface tension (N/m), N_o is Avogadro number ($6.02*10^{23}$/mol), V_S is molar solid volume (m^3/mol), ϕ is a substance dependent constant, and ΔH_{Mf} is molar heat of melting (J/mol). The constants and molecular weight for hydrocarbons are. Equation (2.S1) provides a means for estimating the temperature dependence of σ_{sl} provided that data on both ΔH_{Mf} and V_s as a function of temperature are available.

The data used in conjunction with Eq. (2.S1) for benzene, heptane and naphthalene are summarized in Tables 2.S1-S4.

	ϕ	Molecular weight (g/mol)
Benzene	0.35	78.112
Heptane	0.33	100.20
Naphthalene	0.31	128.17

Table 2.S1. Ratios of molar surface tension to molar heat of melting and molecular weight (MW) [62].

T (K)	Heat of melting, ΔH_f (J/mol) (x10^4)	Solid specific volume, V_M (m^3/mol) (x10^{-5})	Solid-liquid surface tension, σ_{sl} (N/m) (x10^{-2})
230	1.536	7.705	3.517
240	1.435	7.707	3.285
250	1.328	7.709	3.039
260	1.215	7.711	2.780
270	1.096	7.714	2.506
278.16	0.986	7.715	2.272

Table 2.S2. Surface tension of benzene as a function of temperature. The heat of melting was given in [63], molar solid density (or specific volume) are from [64]. The surface tension is calculated by using Equation (2.S1). The curve fit of the surface tension for heptane is given by $\sigma_{sl} = -2.58\text{x}10^{-4}T + 9.49\text{x}10^{-2}$.

T (K)	Heat of melting, ΔH_f (J/mol) ($\times 10^4$)	Solid specific volume, V_M (m^3/mol) ($\times 10^{-4}$)	Solid-liquid surface tension, σ_{sl} (N/m) ($\times 10^{-2}$)
110	2.283	1.131	4.588
120	2.181	1.135	4.371
130	2.073	1.140	4.143
140	1.959	1.144	3.906
150	1.839	1.148	3.659
160	1.713	1.152	3.401
170	1.581	1.156	3.131
180	1.440	1.159	2.847
182.5	1.403	1.160	2.772

Table 2.S3. Surface tension of heptane as a function of temperature. The heat of melting was given in [65], molar solid density (or specific volume) are from [64]. The surface tension is calculated by using Equation (2.S1). The curve fit of the surface tension for heptane is given by $\sigma_{sl} = -2.11\times10^{-4}T + 6.21\times10^{-2}$.

T (K)	Heat of melting, ΔH_f (J/mol) (x10^4)	Solid specific volume, V_M (m^3/mol) (x10^{-4})	Solid-liquid surface tension, σ_{sl} (N/m) (x10^{-2})
300	2.895	1.093	4.65
310	2.725	1.096	4.37
320	2.547	1.099	4.08
330	2.362	1.101	3.78
340	2.170	1.104	3.46
350	1.968	1.107	3.14
353.43	1.897	1.108	3.02

Table 2.S4. Surface tension of naphthalene as a function of temperature. Heat of melting was given in [66], solid density (or specific volume) are from [67]. The curve fit of the surface tension for naphthalene is given by $\sigma_{sl} = -3.06\text{x}10^{-4}T + 1.39\text{x}10^{-2}$.

T (K)	Solid-liquid surface tension, σ_{sl} (N/m) (x10^{-2})
273	2.90
270	2.82
265	2.69
260	2.56
255	2.43
250	2.30
245	2.17

Table 2.S5. Solid-liquid surface tension of Ice as a function of temperature [68].

Optimal values of d. Equation (2.9) was fit to experimental data from [69] by varying d (which represents two times the Tolman length) to maximize R^2. The molecular diameters for benzene, heptane, naphthalene, and water are 5.27 Å [70], 4 Å [71], 6 Å [72], and 2.75 Å [73] . It is typical for a monolayer of adsorbed material to remain unfrozen at the pore wall and radius used in Eq. (2.10) was then the pore radius minus the molecular diameter. The latent heats of phase change for hydrocarbons in [69] were also adjusted, but water is already adjusted values. Tables 2.S5-S7 give the experimental values for the scale dependent latent heat of melting along with the best fit of Eq. (2.10) to those data. Optimal values of d are given in Figs. (2.S1-S4).

Experimental data adjustment. The Experimental data for hydrocarbons is from [69] which has an assumption that no liquid layers exist between solid and pore

structure. However, it is typical that a mono or bi-layer of unfrozen layers material exists at the pore surface. The data for hydrocarbons[69] were modified to take an unfrozen mono-layer into consideration. However, for water/ice this layer is already considered in the data [6, 74]

$$\Delta H_{\mathrm{mod}ified} = \Delta H_{origin\_data} * \left(\frac{r-t}{r} \right)^3 \qquad (2.S2)$$

where, $\Delta H_{\text{modified}}$ is the melting heat for reduced size of solid, $\Delta H_{\text{original}}$ is the melting heat from [69], ‘r’ is the radius of the pore, and ‘t’ is the thickness of unfrozen liquid layer between pores and solid hydrocarbons.

Diameter (m x10^{-9})	Δq , theory (cal/g)	Δq , experiment (cal/g)
100	0	0
72.9	-0.50	-1.21
25.5	-3.88	-3.80
15.6	-7.13	-8.27
8.5	-13.8	-15.6
3.95	-25.8	-25.4

Table 2.S6. Change in the heat of melting for benzene: The theoretical values calculated by Eq. (2.10) and the adjusted experimental results [69] change as the diameter of droplet varies. Both values at 100*10^{-9} (m) are shifted to 0 under the assumption that 100nm pore has the same latent heat of melting as bulk state.

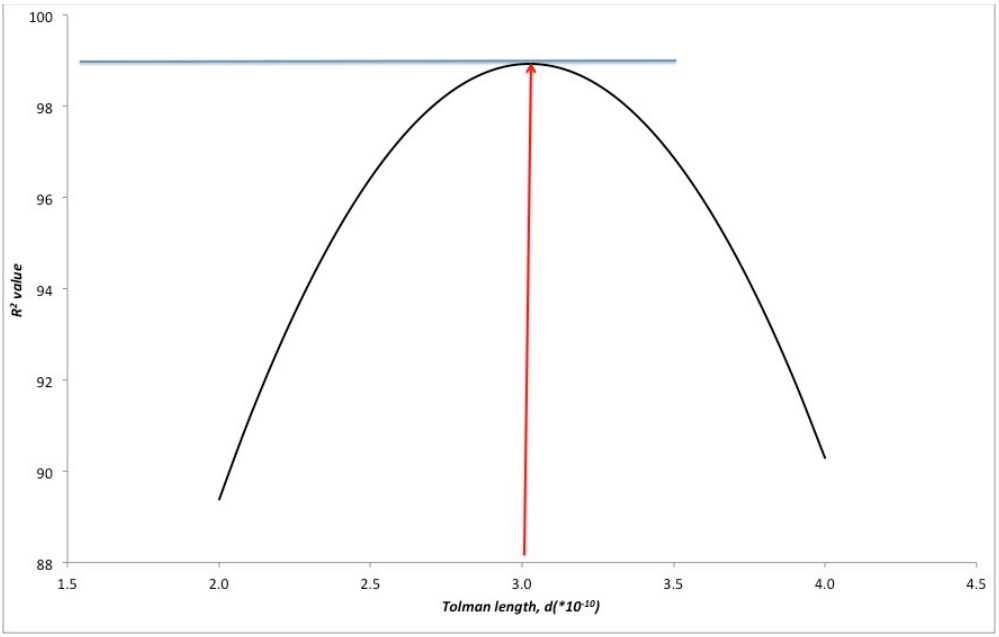

Figure 2.S1. R^2 value for benzene according to Tolman length: A value of d= 3.0*10^{-10} yields the highest R^2 = 0.99.

Diameter (m x10^{-9})	Δq , theory (cal/g)	Δq , experiment (cal/g)
100	0	0
72.9	-0.38	-1.18
25.5	-3.03	-3.66
15.6	-5.63	-6.70
8.5	-11.3	-15.0
3.95	-25.6	-24.9

Table 2.S7. Change in the heat melting for heptane: The theoretical change in heat of melting calculated by Equation (2.10) and the adjusted experimental results [69] change as the diameter of droplet varies. Both values at $100*10^{-9}$ (m) are shifted to 0 under the assumption that 100nm pore has the same latent heat of melting as bulk state.

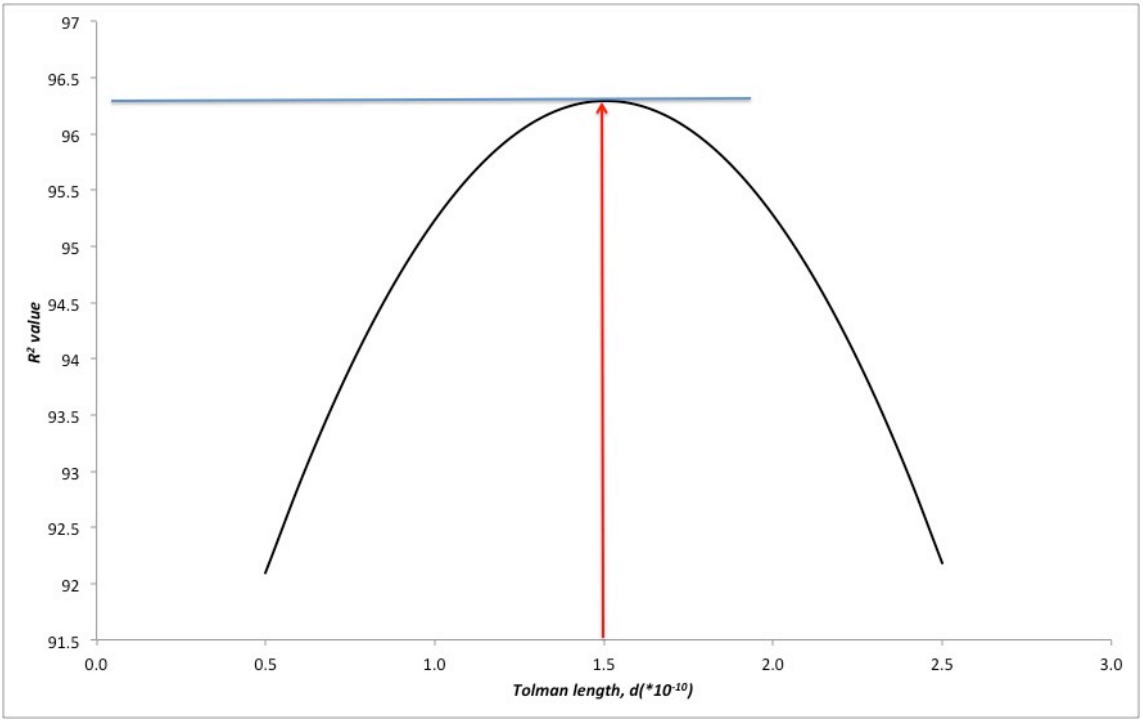

Figure 2.S2. R^2 value for heptane according to Tolman length: A value of d= $1.5*10^{-10}$ (m) yields the highest R^2 =0.96.

Diameter (m *10^{-9})	Δq, theory (cal/g)	Δq, experiment (cal/g)
100	0	0
72.9	-0.73	-1.59
32.4	-4.03	-5.07
25.5	-5.61	-7.94
15.6	-10.19	-11.2
3.95	-26.9	-26.8

Table 2.S8. Change in the heat of melting for naphthalene: Theoretical values calculated by Equation (2.10) and the adjusted experimental results [69] change as the diameter of droplet varies. Both values at $100*10^{-9}$ (m) are shifted to 0 under the assumption that 100nm pore has the same latent heat of melting as bulk state.

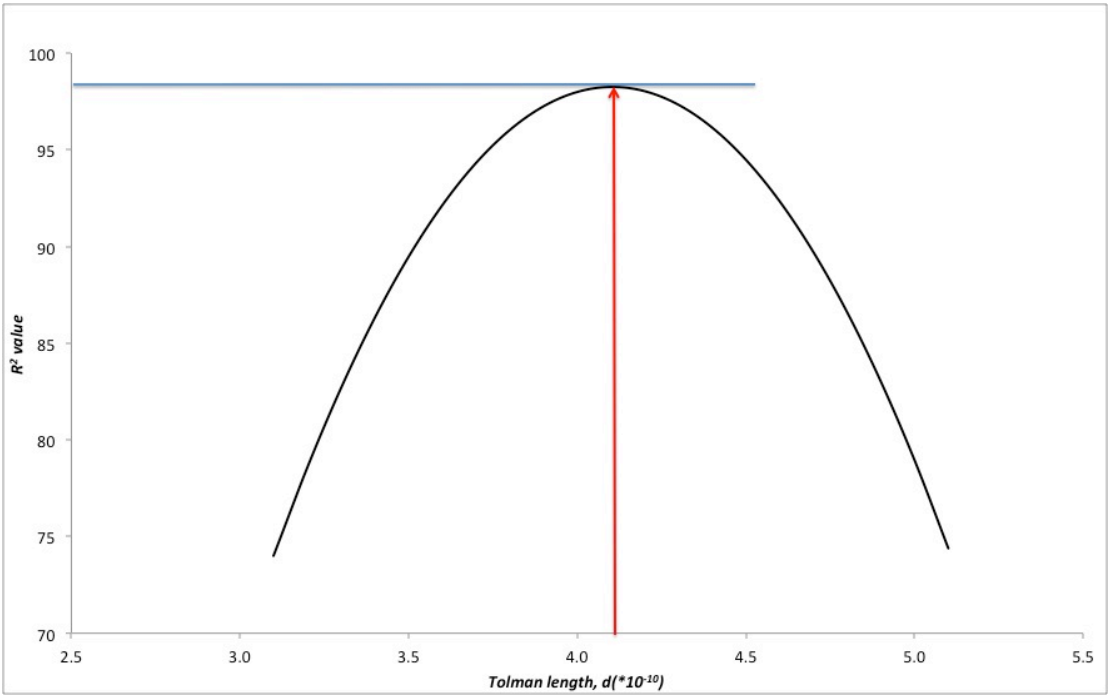

Figure 2.S3. R^2 value for naphthalene according to Tolman length: A value of $d=4.1x10^{-11}$, yields the highest $R^2=0.98$.

Diameter (m x 10^{-9})	Δq ,theory (J/g)	Δq ,experiment (J/g)
7.60	-0.30	-0.32
7.10	-0.33	-0.34
5.70	-0.44	-0.47
4.80	-0.56	-0.54
4.30	-0.66	-0.59
3.40	-0.95	-1.50
2.66	-1.45	-1.73
2.22	-2.05	-2.16
1.82	-3.13	-2.83

Table 2.S9. Change in the heat of melting for ice (H_2O): Theoretical values calculated by Equation (2.10) and the experimental results for small pore diameter [6] and for large pore diameter [74] change as the diameter of droplet varies. Both values at $100*10^{-9}$ (m) are shifted to 0 under the assumption that 100nm pore has the same latent heat of melting as bulk state.

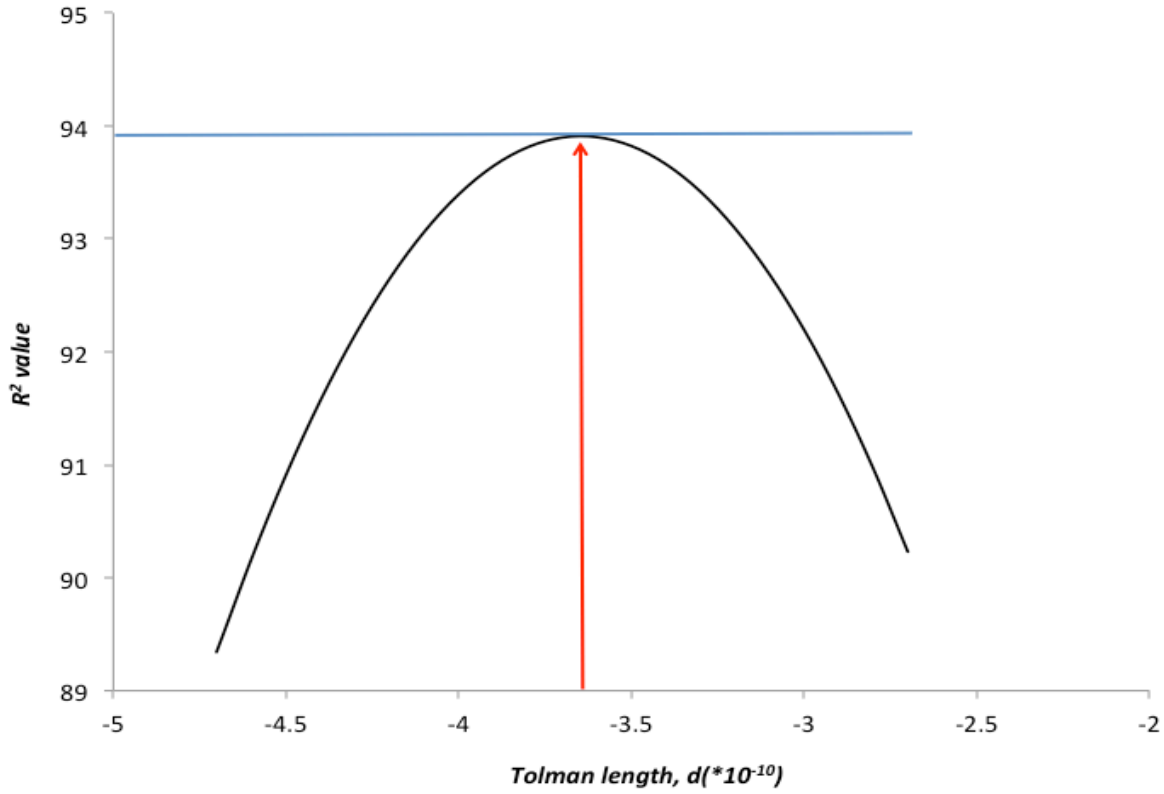

Figure 2.S4. R^2 value for water/ice according to Tolman length: A value of d=-3.7 x10^{-10}, yields the highest R^2 =0.94.

Tolman lengths for hydrocarbons were calculated with the equation (1) given in the published literature [75]. The equation is given as follow:

$$\delta(D) = \frac{D}{4}\left[\exp\left(\frac{2S_b}{3R}\frac{1}{2D/h-1}\right)/\left(1-\frac{1}{2D/h-1}\right)-1\right] \qquad (2.S3)$$

In order to calculate them, parameters given in Table 2.S9 were used and C-H bond lengths are 1.084 Å [76], 1.121 Å [76], and 1.070 Å [76] for benzene, heptane, and naphthalene, respectively.

	h {nm}	E_o {J/mol} x10^4	T_b {K}	$S_b = E_o/T_b$ {J/(mol.K)}
Benzene	0.108	3.07	353.24	86.91
Heptane	0.112	3.18	371.58	85.58
Naphthalene	0.107	4.33	491.43	88.11

Table 2.S10. Several necessary parameters used in Eq. (2.S3). h is C-H bond length [76], and S_b is entropy with E_o and T_b, bulk solid-vapor transition enthalpy and temperature.

Following figures show the calculated Tolman lengths as a function of diameter and averaged values. The calculated averaged Tolman lengths using the equation (1) are 1.09 x 10^{-10}, 1.11 x 10^{-10}, and 1.09 x 10^{-10} for heptane, benzene, and naphthalene respectively. On the other hand, Tolman lengths for fitting were 7.5 x 10^{-11}, 1.5 x 10^{-10}, and 2.1x10^{-10} for heptane, benzene, and naphthalene, respectively.

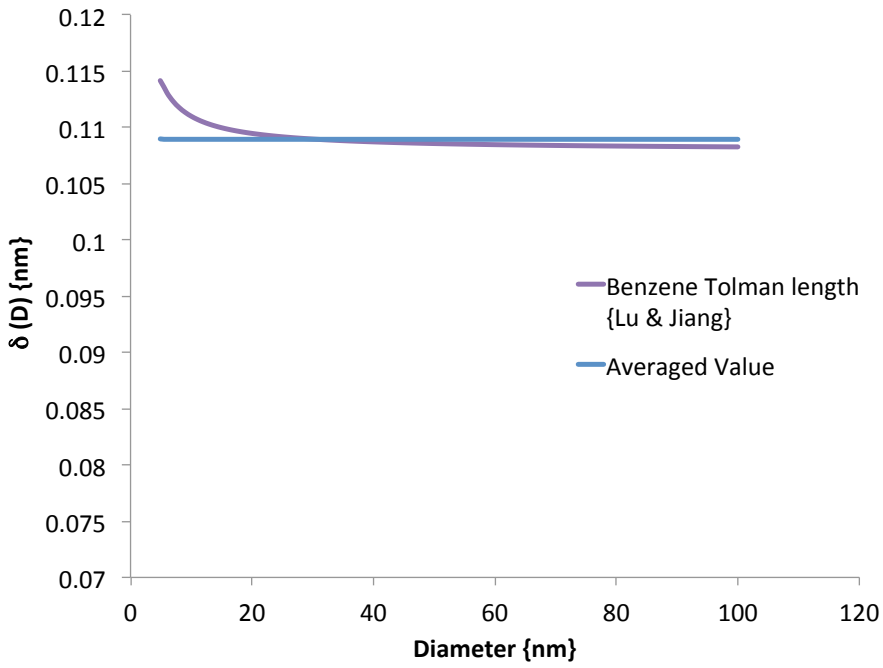

Figure 2.S5. Tolman length of Benzene as a function of pore diameter. The averaged Tolman length is 1.09×10^{-10}.

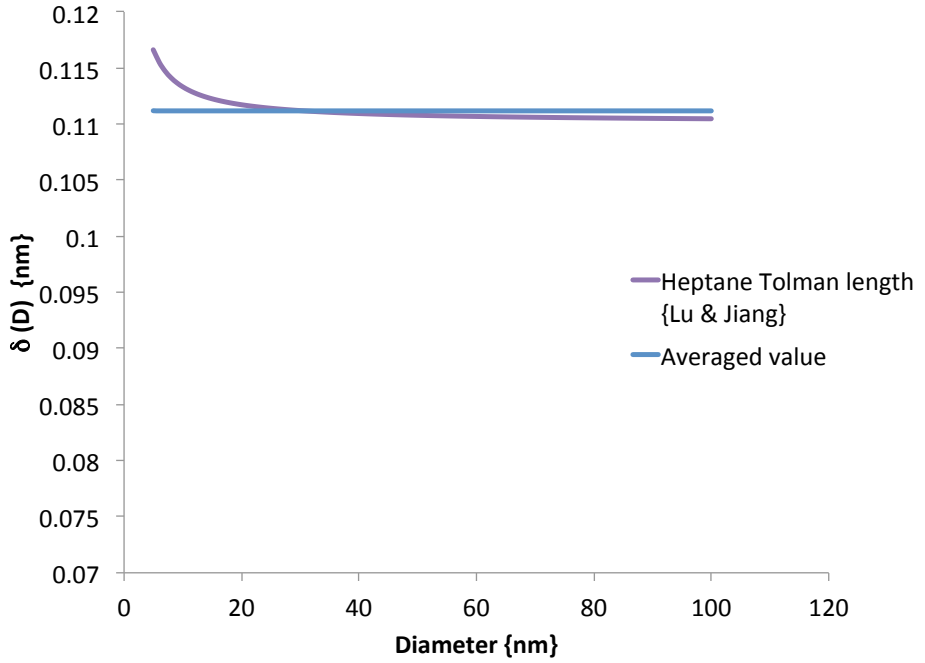

Figure 2.S6. Tolman length of Heptane as a function of pore diameter. The averaged Tolman length is 1.11×10^{-10}.

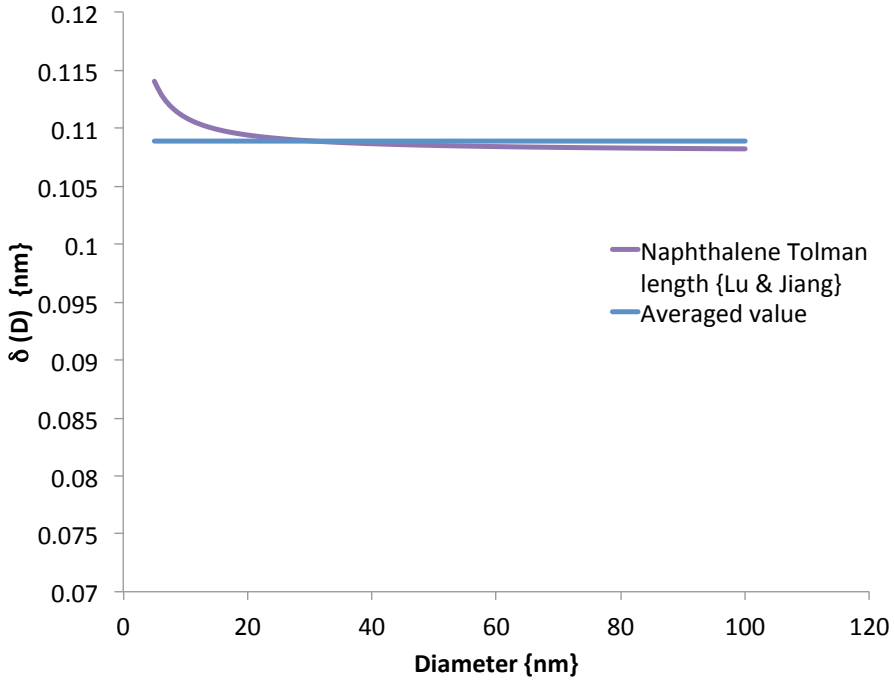

Figure 2.S7. Tolman length of Naphthalene as a function of pore diameter. The averaged Tolman length is 1.09×10^{-10}.

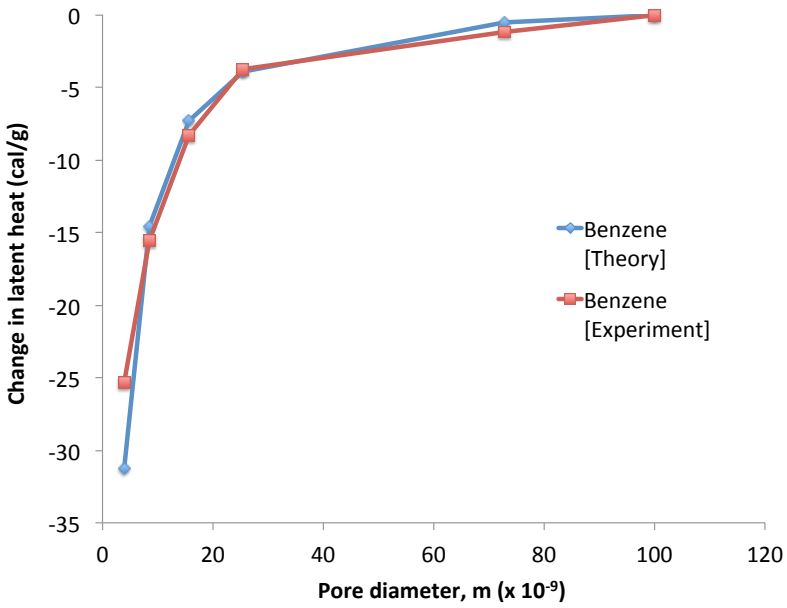

Figure 2.S8. This figure shows the change in latent heat for Benzene with the calculated Tolman length, 1.09×10^{-10}, and $R^2 = 0.92$.

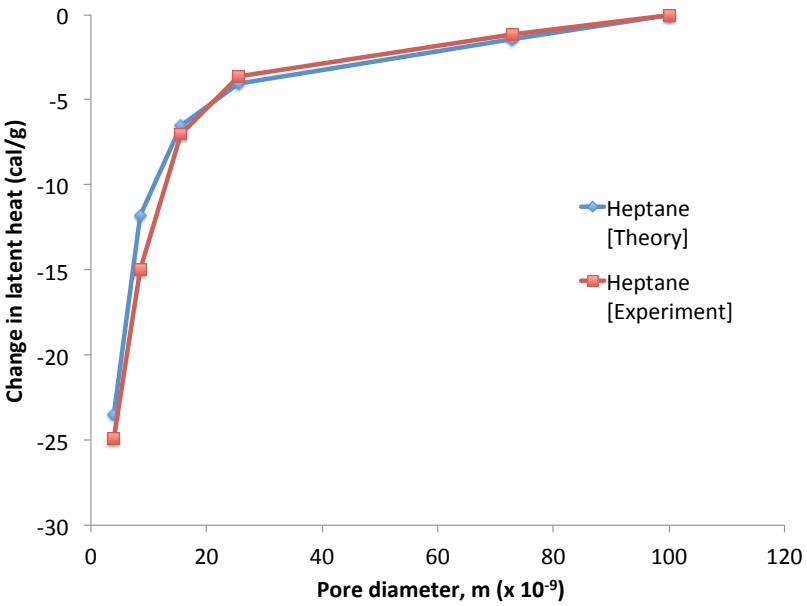

Figure 2.S9. This figure shows the change in latent heat for Heptane with the calculated Tolman length, 1.11×10^{-10}, and $R^2 = 0.97$.

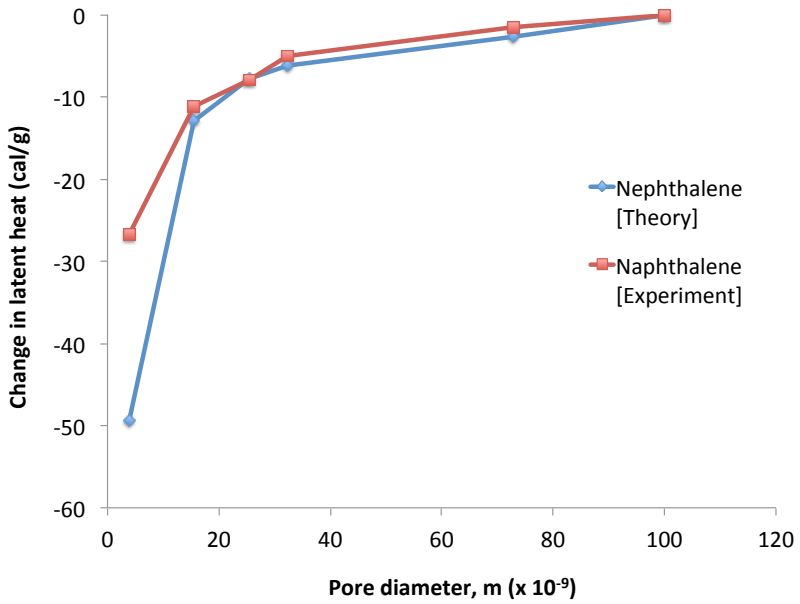

Figure 2.S10. This figure shows the change in latent heat for Naphthalene with the calculated Tolman length, 1.09×10^{-10}, $R^2 = 0.70$.

Chapter 3. A model for the latent heat of melting in free standing metal nanoparticles‡

3.1. ABSTRACT

Nanoparticles of many metals are known to exhibit scale dependent latent heats of melting. Analytical models for this phenomenon have so far failed to completely capture the observed phenomena. Here we present a thermodynamic analysis for the melting of metal nanoparticles in terms of their internal energy and a scale dependent surface tension proposed by Tolman. The resulting model predicts the scale dependence of the latent heat of melting and is confirmed using published data for tin and aluminum.

3.2. INTRODUCTION

Latent heats of phase change affect processes that range in scale from the global hydrological [1] to the manufacture of nano-scale structures [2, 3]. As early as 1871 it was recognized that the thermodynamic properties of materials at small scale could be different than in bulk state [4]. The dramatic increase in nano-science that has occurred in the past two decades has made modeling these changes increasingly important. Small scale systems often exhibit high surface area to volume ratios which gives the surface energy an increasing large effect on

‡ The contents in this chapter were published in Journal of Chemical Physics: Shin, Jeong-Heon, Mark R. Deinert., " A model for the latent heat of melting in free standing metal nanoparticles., Journal of Chemical Physics, 2014,140, 164707.

material properties as the scale is reduced [34, 37, 77]. This is true for both solid and liquid phases, as well as transitions between them.

Considerable research has been done on the effect that fluid interfaces have on vapor and capillary pressure [15, 22, 23, 55, 78, 79]. Melting point depression for small scale materials has been demonstrated. Analytical explanations for these phenomena have been made in terms of the Gibbs-Thompson equation and semi-empirical relationships, but fail to fully explain the change in the latent heat of melting in small scale systems. [32, 33, 35].

Free standing nanoparticles can exhibit a range of melting behavior [35, 80-82]. Several studies have shown that metallic nanoparticles of tin, and indium melt through a liquid shell. Experiments suggest that this layer either exists as a part of these metals at the nanoscale, or that it forms well below the bulk melting temperature and requires very little energy [35, 83]. Experimental data also suggests that aluminum nanoparticles melt through a liquid layer [80, 82]. However, with aluminum, an oxide layer also forms around the particle [82, 84], and the surface tension of this layer increases the pressure in the aluminum core, Fig. 3.1. In addition, the liquid aluminum and oxide layers have different coefficients of thermal expansion, and it has been shown that this can affect the energy required to melt the nanoparticles [82]. In both cases, the surface tension of the liquid layer increases the pressure in the underlying solid particle, and in the case of aluminum, the oxide layer does as well, Fig. 3.1.

Scale effects in the latent of melting have also been observed with materials confined in nanopores [5, 42, 43]. Recent work [77] has shown that these observations can be explained using a first law analysis and a scale dependent correction to the surface tension using a Tolman length [36]. For melting in nanopores surface area to volume ratio was found to be the dominant factor affecting the latent heat. Changes to the surface tension were found to be second order effects until the particles become very small. In the present contribution we extend this thermodynamic analysis to free standing metal nanoparticles that melt through liquid surface or oxide layers. A critical difference between the two systems is the increase in internal pressure that the metallic particle experiences as a result of liquid and oxide surface layers. The Tolman length itself is estimated using the results of a statistical mechanical analysis of interfaces [75, 85]. The resulting model predicts the scale dependence for the latent heat of melting in spherical metallic nanoparticles, and is confirmed using published experimental data for tin and aluminum.

3.3. METHODS

The latent heat of melting for bulk materials is equal to the difference between the liquid and solid phase enthalpies. However, previous work has shown that at small scale, an additional term is required that captures the pressure difference caused by the interface between the phases [77, 86]. For nanoparticles with a liquid surface layer it can be shown that the latent heat of

melting for a nanoparticle that melts through a liquid surface layer is given by [87]:

$$q = h_l - h_s + \frac{2v_s\sigma_{sl}}{r_s} - \frac{2(v_l - v_s)\sigma_{lv}}{r_l} \quad (3.1).$$

Here, q is the latent heat of melting {J/kg}, h_l and h_s are the specific enthalpy of the liquid and solid phases {J/kg}, v_s and v_l are the solid and liquid specific volumes {kg/m^3}, σ_{sl} and σ_{lv} are the solid-liquid and liquid-vapor surface tensions {J/m^2}, with r_s and r_l being the radius of the solid particle and the radius of its liquid surface layer, Fig. 3.1 {m}. For a particle that forms a surface oxide shell, the latent heat of melting can be given by:

$$q = h_l - h_s + \frac{2\sigma_{sl}v_s}{r_s} - \frac{2\sigma_{ol}(v_l - v_s)}{r_l} - \frac{2\sigma_{ov}(v_l - v_s)}{r_o} \quad (3.2).$$

Here σ_{ol} is the surface tension of the oxide-liquid interface, σ_{ov} is the surface tension of the oxide-vapor interface, and r_o is the radius of the oxide layer.

As the scale of a substance is reduced, both h_l and h_s are also affected. The change in the total internal energy of the system can be written as [40]:

$$dU = TdS - p_l dV_l - p_s dV_s + \sigma_{sl}dA + \sigma_{lv}dA_l \quad (3.3).$$

Here T is the temperature {K}, S is the entropy of the fluid-solid system {J/K}, p is pressure {Pa}, V is volume {m^3}, A is interfacial surface area {m^2} with the subscripts l and s denoting liquid and solid, and σ_{lv} is the liquid-vapor surface tension {J/m^2}. Because the liquid and solid phases interact only through the interface, we can separate Eq. (3.3) into its phase components, and it can be shown that the enthalpy of the solid and liquid phases are given by:

$$dH_s = V_s dp_s + TdS_s + \sigma_{sl} dA_s$$
$$dH_l = V_l dp_l + TdS_l + \sigma_{lv} dA_l \qquad (3.4)$$

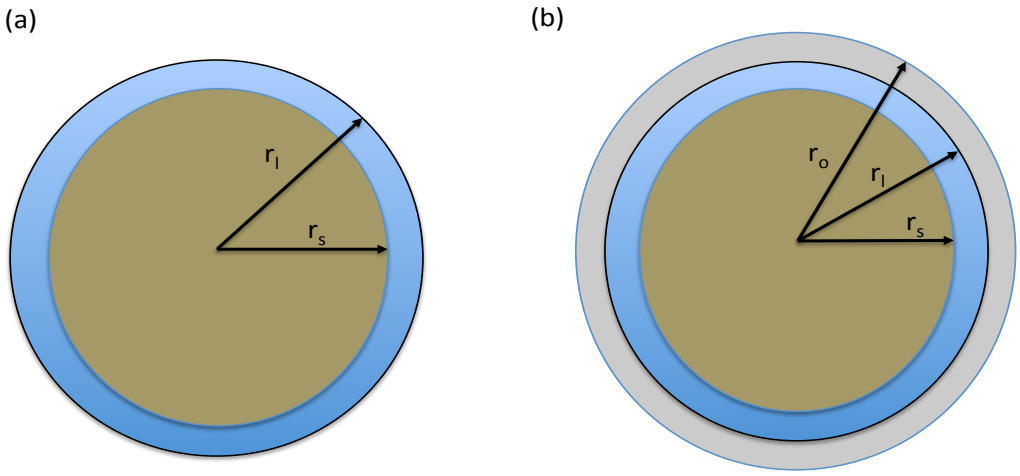

Figure 3.1. This schematic shows solid particle and its liquid layer. Figure (a) is for Tin particle. Tin particle is covered with its liquid layer, 1.6 nm [18] and Figure (b) is for aluminum particle. Aluminum particle is covered with aluminum oxide layer (Al_2O_3) and liquid aluminum exists between aluminum core and aluminum oxide.

For many metals, the change in density with melting is small and the corresponding change in liquid pressure, p_l, and surface area, A_l, would be negligible as a particle melts. As a result, Eq. (3.4) would give $dH_l = T\mathrm{d}S_l$. If the phase change takes place at constant temperature, then $\mathrm{d}S_l \sim 0$, and the change in enthalpy of the fluid can be ignored. By contrast, the change in area and pressure associated with the formation, and melting, of a nanoparticle are not negligible. The change in the specific enthalpy of the solid phase can be obtained from Eq. (3.4) as follows:

$$\Delta H_s = \int_{p_o}^{p_o+\Delta p} V_s \, dp_s + \int_{S_o}^{S} T \, dS_s + \int_{0}^{A} \sigma_{sl} \, dA \qquad (3.5),$$

where Δp is the pressure change at the interface between solid and bulk liquid {Pa}. It is known that surface tension varies with scale and can be approximated using a relationship proposed by Tolman [36]:

$$\sigma_{sl} = \sigma_{0,sl}(1-2\delta/r_s) \qquad (3.6),$$

where, $\sigma_{0,sl}$ is the bulk liquid-solid surface tension and δ {m} is the Tolman length, and r_s is the radius of the solid particle. Assuming an incompressible solid, we

can combine Eqs. (3.5, 6), integrate, and divide by the volume of a spherical particle to get:

$$\Delta h_s = v_s \Delta p + T \Delta s_s + \frac{3 v_s \sigma_{0,sl}}{r_s} - \frac{12 v_s \sigma_{0,sl} \delta}{r_s^2} \qquad (3.7).$$

Here Δh_s is the change of specific enthalpy of the solid phase {J/kg}, v_s is the solid specific volume {m^3/kg}, and Δs_s is the change of specific entropy of the solid phase {J/kg•K}. The entropy change at constant pressure is given by $\Delta S_s = -(\partial \Delta G_s / \partial T)_{p,A}$, where ΔG_s can be obtained from:

$$dG_s = V_s dp_s - S_s dT + \sigma_{sl} dA_s \qquad (3.8)$$

For a constant temperature process, dT is zero and integration of Eq. (3.8) then gives the same first and third terms as those on the right hand side of Eq. (3.5). Combining results we get:

$$\Delta h_s = v_s \Delta p + \frac{3 v_s \sigma_{0,sl}}{r_s} - \frac{12 v_s \sigma_{0,sl} \delta}{r_s^2} - T\left(\Delta p \frac{dv_s}{dT} + \frac{3 v_s}{r_s} \frac{d\sigma_{0,sl}}{dT} - \frac{12 v_s \delta}{r_s^2} \frac{d\sigma_{0,sl}}{dT} \right) \qquad (3.9)$$

For particles with a liquid surface layer, $\Delta p = 2\sigma_{sl}/r_s + 2\sigma_{lv}/r_l$. If an oxide layer surrounds the liquid, as with aluminum, then $\Delta p = 2\sigma_{sl}/r_s + 2\sigma_{lv}/r_l + 2\sigma_{ov}/r_o$. Both the liquid-vapor and oxide-vapor surface tensions are assumed to scale in a

manner similar to Eq. (3.6).

The Tolman length for both liquid-vapor, and solid-vapor interfaces can be estimated using [75]:

$$\delta(D) = \frac{D}{4}\left[\exp\left(\frac{2S_b}{3R}\frac{1}{2D/IR-1}\right)/\left(1-\frac{1}{2D/IR-1}\right)-1\right] \quad (3.10).$$

Here δ {m} is the Tolman length, D is the diameter of the particle {m}, S_b is the solid-vapor transition entropy {J/mol•K}, R is the ideal gas constant, and IR is the atomic diameter {m}. Respective values for aluminum and tin can be found in the supplemental information. For spherical particles the contact angle between the phases is zero and Dupre's relationship becomes σ_{sv} - σ_{lv} = σ_{sl}, and Eq. (3.10) can also be used to approximate the Tolman length for the solid-liquid interface.

Since the change in the specific enthalpy of the liquid can in general be assumed to be small, the change in the latent heat of melting for a particle with a liquid surface layer is given by:

$$\Delta q = -\Delta h_s + v_s(2\sigma_{sl}/r_s) - 2\sigma_{lv}(v_l - v_s)/r_l \quad (3.11).$$

For a particle with an additional oxide layer over the liquid:

$$\Delta q = -\Delta h_s + v_s 2\sigma_{sl}/r_l - 2\sigma_{ol}(v_l - v_s)/r_l - 2\sigma_{ov}(v_l - v_s)/r_o \quad (3.12).$$

In both cases Δh_s is given by Eq. (3.9).

Data on the scale dependent latent heat of melting, as well as temperature dependent surface tensions and specific volumes, are available for 'freestanding' tin and aluminum nanoparticles [35, 82, 84]. The particles in these studies are freestanding in the sense that they are deposited on a surface with a minimal point of contact.

Temperature dependent data for the liquid-vapor surface tensions for tin and aluminum were taken from [88, 89]. Solid-liquid surface tensions have been shown to be strongly related to the liquid-vapor surface tension and the method of Tyson and Miller (1977) [90] gives $\sigma_{sl} = 0.11\sigma_{lv}$ for tin and $\sigma_{sl} = 0.18\sigma_{lv}$ for aluminum. The surface tension of aluminum oxide-vapor interface depends on the aluminum oxide phase, and this is true for the surface tension of the metal liquid-oxide interface as well. The phase stability of aluminum oxide is a function of the layer thickness, specific surface area, and temperature [91, 92]. For the particle sizes, oxide layer thicknesses, and temperature ranges in [82], the energetically stable oxide phase would be α-Al_2O_3 [87, 91, 92]. The oxide-vapor surface tensions for α-Al_2O_3 was taken from [93]. The surface tension of the metal liquid-oxide interface was determined using Dupre's relation and data on surface wetting of liquid metal aluminum on α-Al_2O_3 [94]. Data on the respective

surface tensions can be found in the supplemental information [87].

Equation (3.10) shows the Tolman length to be a function of particle size, though the dependence is weak except for very small particles. Over the range of particle sizes for the data in [82], δ ~ constant [87]. The Tolman lengths used for tin, aluminum, and aluminum oxide were computed using Eq. (3.10), and were 3.73×10^{-10}, 3.11×10^{-10}, and 5.03×10^{-11} {m} respectively, and represent average values [87] over the size ranges for the data in [35, 82, 84].

3.4. RESULTS AND DISCUSSION

Figures 2 shows a comparison of Eqs. (3.9,11) to published data for the latent heat of melting of free standing tin, where Eq. (3.10) is used to estimate the Tolman length. Figure 3 shows a comparison of Eqs. (3.9,12) to data from Sun and Simon (2007) [82] for the latent heat of melt of aluminum nanoparticles where Eq. (3.10) is used to estimate the Tolman length. As with the melting of particles confined in nanopores [77], the surface area to volume ratio has the dominant effect on the latent heat of melting. The scale dependence of the surface tension is a second order effect, becoming important only when the particles become very small. This is easy to understand on physical grounds as the Tolman length takes into consider the effect of molecular packing in the interfacial region between phases. As size decreases, a larger fraction of its molecules occupy this interfacial region. The Tolman length is defined to be the distance over which the transition

between phases occurs, and this is typically less than a few molecular diameters. The predictions of Eq. (3.10) are consistent with this scale for both Sn and Al.

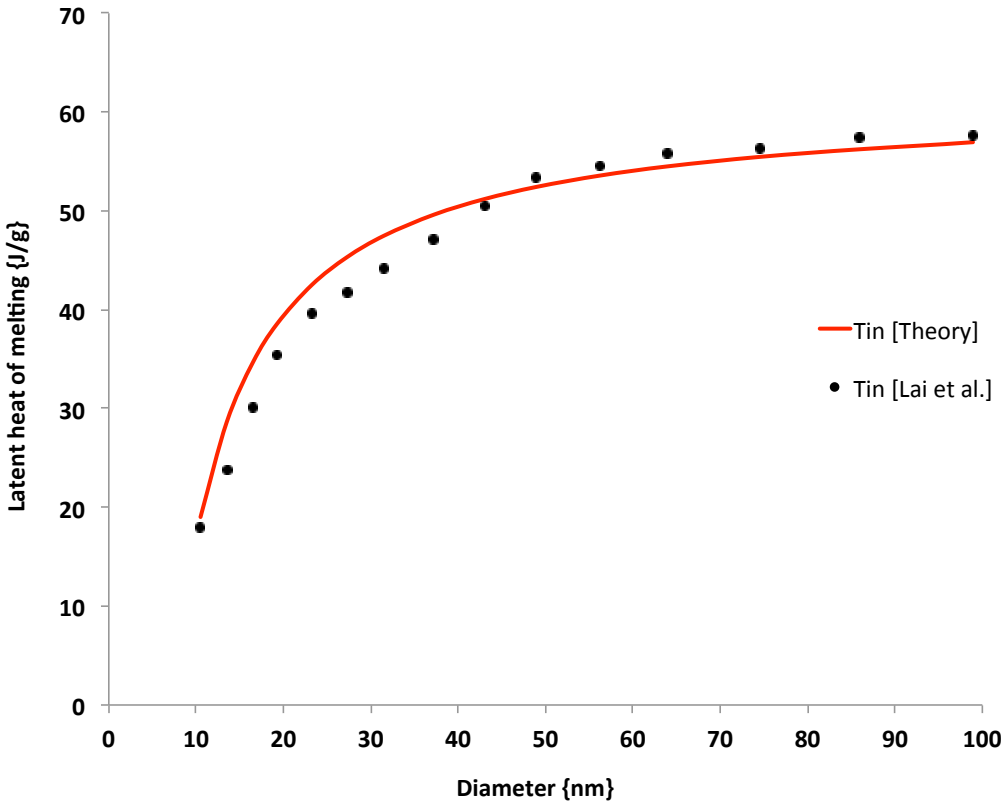

Figure 3.2. Experimental data for tin is from S.L. Lai et al [18] and calculated result fit well. The averaged Tolman length is 3.73 x 10^{-10} computed using Eq. (3.10).

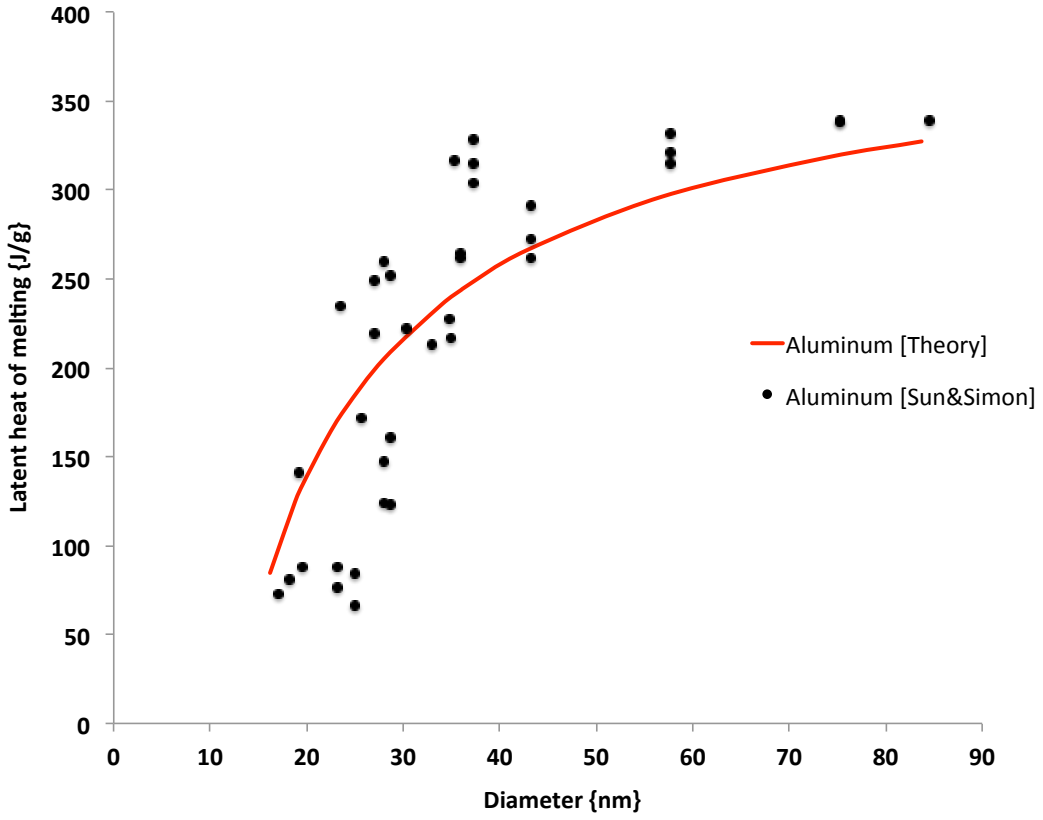

Figure 3.3. Experimental data for aluminum is from Sun and Simon (2007) [19] calculated result fit well. The average Tolman length of aluminum is 3.11×10^{-11} and the averaged Tolman length of aluminum oxide is 5.03×10^{-11}, computed with Eq. (3.10).

The data shown in Fig. 3.2 are from a single experimental system [35] and Eqs. (3.9,10,11) predict the experimental results with an $R^2 = 0.93$. The data in Fig. 3.3 shows considerably more scatter. However Sun and Simon (2007) present the actual data [82], not the averages with associated error bars, so this is to be expected. Equations (3.9,12) predict the trend in the data well when the

Tolman length is estimated using Eqs. (3.10). The data used in Fig. 3.3 were adjusted by Sun and Simon (2007) to account for differences in the thermal expansion of the aluminum oxide and the core it surrounded [82]. However, Sun and Simon (2007) assume that the Al_2O_3 is in an amorphous phase, which has a higher coefficient of thermal expansion than does α-Al_2O_3 ($24x10^{-6}$ -vs- 16.2×10^{-6} $\{K^{-1}\}$, respectively) [95]. If the α- Al_2O_3 is instead assumed, then the latent heat values shown in Fig. 3.3 would actually be slightly lower.

Equation (3.9) assumes that the Tolman length is constant, which is not true when particles become very small. However, for the size range of the experimental data for tin and aluminum [35, 82, 84], Eq. (3.10) gives a relatively constant value and the use of an average Tolman length for the size range is justified [87]. The density change on melting for tin is ~2.8% and for aluminum it is ~6.7% [35, 82, 96]. The change in surface area and volume that comes with the melting of nanoparticles is then quite small. In addition, the liquid-solid surface and liquid-vapor surface tensions are of the same magnitude. Taken together, the assumption made in Eq. (3.10) that $\Delta h_l << \Delta h_s$ is valid.

The derivation presented here gives a model with which to predict how the latent heat of melting for free standing metal nanoparticles changes as the scale of substance is reduced. The results are based on a first law analysis with a functional estimate for the Tolman length and are applicable to particles with liquid and oxide surface layers. The number of metals for which the inputs to Eqs.

(3.9,11,12) are available, and for which scale dependent change in the heat of melting has been measured, is relatively small. However, predictions made using Eqs (3.9,10,11,12) show a strong correlation to the available data for tin and aluminum.

SUPPLEMENTAL INFORMATION

Specific heats of melting for nanoparticles. The specific heat of melting for a spherical particle that is contact with its liquid phase at constant temperature and pressure in a closed system can be derived as follow. Let Q be the heat required for the phase change, then:

$$Q = \Delta U + P_o \Delta V \qquad (3.S1),$$

where U is the internal energy of the system (solid and liquid), V is the volume of the particle, and P_o is the constant pressure of the atmosphere that surrounds the particle. Assuming complete melting of a mass m {g},

$$\Delta U = mu_l - mu_s \qquad (3.S2)$$

$$\Delta V = \Delta V_l + \Delta V_l \qquad (3.S3)$$

$$\Delta V_l = mv_l \qquad (3.S4)$$

$$\Delta V_s = -mv_s \qquad (3.S5).$$

Here m is the mass of material undergoing the phase change, u_l and u_s are the specific internal energy of the respective liquid and solid phases {J/kg}, with v_l and v_s the respective specific volumes {m^3/kg}.

The pressure in the solid core of particles with liquid surface layers is given by:

$$P_s = 2\sigma_{sl}/r_s + 2\sigma_{lv}/r_l + P_o \qquad (3.S6).$$

Here σ_{sl} and σ_{lv} are the solid-liquid and liquid-vapor surface tensions {J/m^2}, with r_s and r_l the respective radii {m} as defined in Fig. 3.1. For a particle with a solid oxide surface surrounding the liquid layer we get:

$$P_s = 2\sigma_{sl}/r_s + 2\sigma_{lv}/r_l + 2\sigma_{ov}/r_o + P_o \qquad (3.S7),$$

where σ_{ov} is the oxide-vapor surface tension {J/m^2}, and r_o is the outer radius of the oxide layer.

Combining Eqs. (3.S1-S5) we get:

$$Q = mu_l - mu_s + mP_ov_l - mP_ov_s \qquad (3.S8).$$

Combining Eq. (3.S8) with Eq. (3.S6), and dividing by *m*, then gives:

$$q = h_l - h_s + v_s 2\sigma_{sl}/r_s - 2\sigma_{lv}(v_l - v_s)/r_l \quad \text{(3.S9)}$$

Combining Eq. (3.S8) with Eq. (3.S7), and dividing by *m*, then gives:

$$q = h_l - h_s + v_s 2\sigma_{sl}/r_l - 2\sigma_{ol}(v_l - v_s)/r_l - 2\sigma_{ov}(v_l - v_s)/r_o \quad \text{(3.S10)}$$

Densities of aluminum. The densities of liquid and solid for aluminum are from [97-99] . The liquid density of aluminum is given in {kg/m^3} by [97]:

$$\rho_l(T) = 2377.23 - 0.311(T\{K\} - 933.47) \quad \text{(3.S11)}$$

And solid densities of aluminum are given by [98, 99]:

$$\rho_s(T) = 2776.9 - 238.9 \times 10^{-3}\, T\{K\} \quad \text{(3.S12)}$$

Densities of tin. The densities of liquid and solid for tin are from [100-103]

The liquid density of tin is given in {kg/m^3} by [100]:

$$\rho_l\,(T) = 7374.7 - 675.5 \times 10^{-3}\ T\{K\} \qquad (3.S13)$$

And solid densities of tin, 7.265 {kg/m^3} at 25 C, 7.298 {kg/m^3} at 15 C, and 7.180 {kg/m^3} at 232 C are from [101-103] and the curve fit is given in {kg/m3} as below:

$$\rho_s\,(T) = 7420 - 484 \times 10^{-3}\ T\{K\} \qquad (3.S14)$$

Liquid Aluminum			Solid Aluminum		
Temp. {^{o}C}	Density {kg/m^3}	Spec. vol. (x10^{-4}) {m^3/kg}	Temp. {^{o}C}	Density {kg/m^3}	Spec. vol. (x10^{-4}) {m^3/kg}
933.47	2377.23	4.207	890	2564.28	3.899
940	2375.20	4.210	900	2561.89	3.903
950	2372.09	4.216	910	2559.50	3.907
960	2368.98	4.221	920	2557.11	3.911
970	2365.87	4.226	933.47	2553.89	3.916

Liquid Tin			Solid Tin		
Temp. {^{o}C}	Density {kg/m^3}	Spec. vol. (x10^{-4}) {m^3/kg}	Temp. {^{o}C}	Density {kg/m^3}	Spec. vol. (x10^{-4}) {m^3/kg}
231.93	7218.03	1.385	190	7328.04	1.365
240	7212.58	1.386	200	7323.20	1.366
250	7205.83	1.388	210	7318.36	1.366
260	7199.07	1.389	220	7313.52	1.367
270	7192.32	1.390	231.93	7307.75	1.368

Table 3.S1. Solid, liquid density and specific volume for Aluminum and Tin [97-103].

Surface tensions of aluminum and aluminum oxide interfaces. The surface tension between solid Al_2O_3 and liquid aluminum metal can be estimate using Dupre's relation and Young's equation. Dupre's relation is [104].

$$W = \sigma_{sv} + \sigma_{lv} - \sigma_{ol} \quad (3.S15) .$$

Here σ_{sv} is the solid-vapor surface tension of the solid Al_2O_3, σ_{lv} is the liquid-vapor surface tension of liquid aluminum metal, and σ_{ol} is the surface tension of the interface between the solid Al_2O_3 and the liquid aluminum metal. Young's equation relates the surface tensions to the contact angle [104]:

$$cos\theta = (\sigma_{sv} - \sigma_{ol})/ \sigma_{lv} \quad (3.S16).$$

By combining Eqs. (3.S11, S12) we get:

$$W = \sigma_{lv} [1+ \cos(\theta)] \quad (3.S17).$$

The contact angle between liquid metals and oxide surfaces typically varies between -0.01 and -0.05 (degree/K) [104]. Here we use the midpoint value of $d\theta/dT$= -0.03 {degree/K} to compute *W*. Combining Eqs. (3.S11,S13) we get:

$$\sigma_{ol} = \sigma_{sv} + \sigma_{lv} - W \quad \text{(3.S18).}$$

The liquid-vapor surface tension for aluminum is given in {mJ/m^2} by [105]:

$$\sigma_{lv} = 1024 - 0.274\,[T(K) - 933] \quad \text{(3.S19).}$$

For the Al_2O_3 solid-vapor surface tension is given in {mJ/m^2} by [93]:

$$\sigma_{sv} = 2559 - 0.784\,T(K) \quad \text{(3.S20).}$$

Table 3.S2 shows the values for σ_{sv}, σ_{lv}, and W used to compute σ_{ol}.

Temp. (K)	Contact angle (degree)	W {mJ/m^2}	σ_{lv} {mJ/m^2}	σ_{sv} {mJ/m^2}	σ_{ol} {mJ/m^2}
930	90.29	1019.63	1024.82	1829.88	1840
940	89.99	1022.26	1022.08	1822.04	1820
950	89.69	1024.86	1019.34	1814.20	1810
960	89.39	1027.43	1016.60	1806.36	1800
970	89.09	1029.96	1013.86	1798.52	1780
980	88.79	1032.47	1011.12	1790.68	1770
990	88.49	1034.95	1008.38	1782.84	1760
1000	88.19	1037.41	1005.64	1775.00	1740

Table 3.S2. Surface energies with temperature variation. Here σ_{lv} is the liquid-vapor surface tension for aluminum metal and is computed using Eq. (3.S15). The solid-vapor surface tension for Al_2O_3, σ_{sv}, is computed using Eq. (3.S16). The surface tension of the solid-liquid metal interface, σ_{ol}, is calculated using Eq. (3.S14). Equation (3.S13) is used to compute *W*.

The liquid-solid surface tension for the interface between liquid and solid aluminum metal has been shown to be strongly related to σ_{lv}. Tyson and Miller (1977) suggest $\sigma_{sl} = 0.18\sigma_{lv}$ for aluminum metal and we use that value here [90].

Surface tensions of tin. The liquid–vapor surface tension for tin is given in {mJ/m^2} by [89];

$$\sigma_{lv} = 581 - 0.13\,[T(K) - 505.15] \qquad (3.S21).$$

The solid-liquid surface tension for tin is taken to be $\sigma_{sl} = 0.11\sigma_{lv}$ [90].

Tolman length as a function of diameter. The Tolman length for the liquid-solid, liquid-vapor, and solid-vapor surface tensions for aluminum, tin, and aluminum oxide can be determined using [75]:

$$\delta(D) = \frac{D}{4}\left[\exp\left(\frac{2S_b}{3R}\frac{1}{2D/IR-1}\right)/\left(1-\frac{1}{2D/IR-1}\right)-1\right] \qquad \text{(3.S22)}.$$

Here D is the diameter of the of the particle {m}, S_b is the of the solid-vapor transition entropy {J/mol•K}, R is the ideal gas constant, and IR is the atomic diameter {m}. In the range of the particle size we are looking at for tin and aluminum [7, 8], Eq. (3.S18) gives relatively constant values, Fig. (3.S1). The parameters used in Eq. (3.S18) for tin and aluminum are given in Table 3.S3.

Material	***IR* (nm)**	**H_{LV} (kJ/mol)**	T_b (K)	S_b (=H_{LV}/T_b) (J/mol K)
Aluminum (Al)	0.25	302.185	2792	108.23
Tin (Sn)	0.29	321.615	2875	111.87
Aluminum Oxide (Al_2O_3)	0.18	49.38	3250	15.194

Table 3.S3. Properties for aluminum, tin, and aluminum oxide for Eq. (3.S17). Here *IR* is the atomic diameter [106, 107], H_{LV} is the latent heat of vaporization [108, 109], T_b is boiling point, and S_b is the entropy.

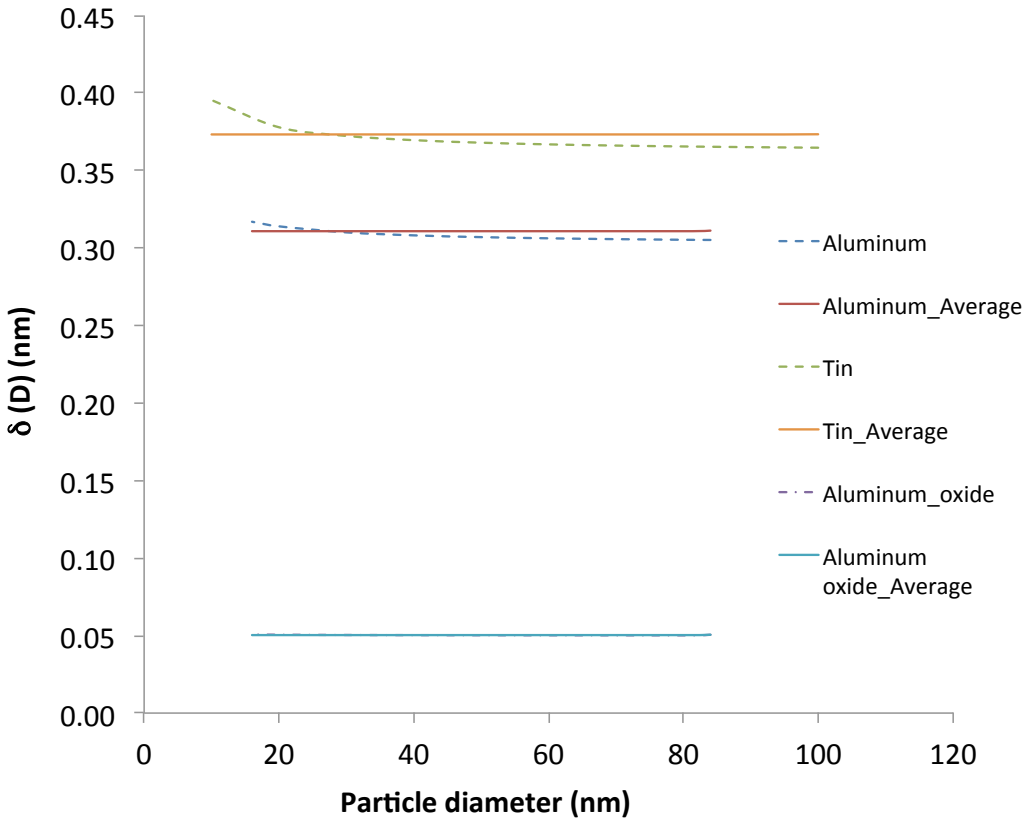

Figure 3.S1. Tolman length as a function of particle diameter. The figure shows how the parameter δ varies with particle diameter for aluminum metal, α-Al_2O_3, and tin as a function of particle diameter. Dashed lines show the predictions of Eq. (3.S18), solid lines show the average value over the diameter range. The diameter ranges correspond to the ranges in the data for tin and aluminum particles in [9,10]. Here Tolman lengths, δ are 3.11 $x10^{-10}$, 5.03 $x10^{-11}$, and 3.73 $x10^{-10}$ for aluminum, α-Al_2O_3, and tin, respectively.

Aluminum oxide phase. Al_2O_3 can exist in several phases with the γ and α phases being the most commonly encountered [110, 111] The specific phase in which Al_2O_3 exists at nanoscale depends on the thickness of the layer, its

temperature, and specific surface area [110-113]. Work with micron scale powders shows that Al_2O_3 exists in an amorphous phase between 300~ 500 C, then transforms to γ phase of Al_2O_3 at ~500 ^oC [113]. As the temperature increases, the phase changes again and finally ends up in the α phase [113]. However, it is known that Al_2O_3 phase is also affected by the specific surface area [111]. McHale et al. [111] shows that the γ phase of Al_2O_3 is more stable thermodynamically when the specific surface area is greater than 125 m^2/g, but with the α phase being more stable below this. For the data in [8], the thickness of the Al_2O_3 layers is also above the critical value at which a crystalline phase forms [110]. The respective specific surface areas of the Al_2O_3 layer on the aluminum particles would be in the range of 23.3 to 48.9 m^2/g, assuming that the particles are spherical. Based on these data we assume the Al_2O_3 surface layer on the aluminum particles in the Sun and Simon study [8] were in the α phase, not the amorphous state that these authors assumed.

Diameter (m x 10^{-9})	Δq, experiment {J/g}	Δq, theory {J/g}
99.0	57.6	56.9
86.0	57.5	56.2
74.5	56.3	55.5
64.0	55.8	54.5
56.3	54.6	53.6
49.0	53.3	52.4
43.0	50.4	51.2
37.3	47.1	49.6
31.5	44.2	47.5
27.3	41.7	45.3
23.3	39.6	42.5
19.3	35.4	38.6
16.5	30.0	34.7
13.5	23.8	28.6
10.5	17.9	19.0

Table 3.S4. Latent heat of melting of tin particle: Theoretical values calculated by Eqs. (3.9, 11) and the experimental results [7].

Diameter {m x 10^{-9}}	Δq, experiment {J/g}	Δq, theory {J/g}
17.0	72.8	94.2
18.3	80.4	117.9
19.3	141.3	130.5
19.5	88.0	133.3
21.0	88.0	149.8
23.3	76.1	170.8
23.5	234.8	172.9
25.0	84.8, 66.3	184.8
25.8	171.7	190.3
27.0	248.9, 219.6	198.8
28.0	123.9, 147.8, 259.8	205.1
28.8	123.3, 160.9, 252.2	209.6
30.3	221.7	217.9
33.0	213.0	231.3
34.8	227.2	238.9
35.0	216.3	239.9
35.3	316.3	240.9
36.0	262.0, 264.1	243.9
37.3	304.4, 314.4, 327.9	248.5
43.3	262.0, 272.8, 291.3	267.4
57.8	315.2, 331.5, 320.7	297.8
75.3	338.0, 339.1	319.7
84.5	339.1	327.7

Table 3.S5. Latent heat of melting of aluminum particle: Theoretical values calculated by Eqs. (3.9,12) and the experimental results [8].

Chapter 4. Water's latent heat of vaporization changes with scale

4.1. Abstract.

Nanometer scale water is ubiquitous in the Earth's environment, and its vaporization and condensation play an important role in the Earth's atmosphere as well as affecting near surface energy budgets. Despite this, the thermodynamic properties of water at this scale remain incompletely understood. It has been known for over a hundred years that water's vapor pressure is affected by the curvature of its interface. More recent work has shown that its latent heat of melting can also change significantly at the nanoscale. Here we show that water's latent heat of vaporization is also affected. Measurements were made using a differential scanning calorimeter and thermo-gravimetric analysis for water confined in porous glass. The results show that the latent heat increases rapidly when vaporization occurs from pores that are < 10 nm in diameter. The results are explained with a thermodynamic model that is applicable to other substances, and where the scale dependence of the interfacial surface tension is taken into consideration using a Tolman length.

4.2. Introduction.

It was shown by Lord Kelvin that the equilibrium vapor pressure of a liquid changes with the scale of its interface [4]. Since then it has been demonstrated that the temperature at which phase changes occur, latent heats of melting, and

surface tensions can also depend on scale [5, 9, 31, 32, 35-37, 80, 86, 114]. Understanding how size affects thermodynamic properties is particularly important in the manipulation of nanomaterials as well as in understanding environmental processes where water at small scale plays a role. In particular, evaporation and condensation at reduced scale play an important role in the formation of clouds [115], the evaporation of sea sprays [116], and water from soils [1, 117]. All of these processes in turn affect near surface energy budgets and temperatures.

It has been shown that water confined in nanopores undergoes phase transitions at different temperatures than in its bulk state, and that this affects the heat capacity of the medium in which it is confined. Changes to the heat capacity of the confined water itself have also been observed [29]. Research has also demonstrated that the temperature at which water droplets evaporate is different at reduced scale than it is in its bulk state, and this can have an effect on near surface temperatures and heat fluxes [118, 119]. The effect of size reduction on latent heats of melting has been studied for select hydrocarbons [5], metal particles [35, 80, 82], as well as water [42, 43, 120]. However, and despite its importance, very little work has been done to establish how scale affects water's latent heat of vaporization or that of any other substance.

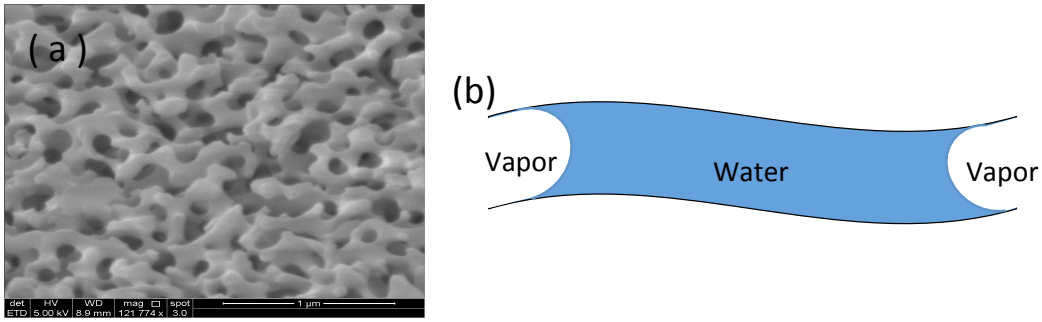

Figure 4.1. Nanoporous matrix. (a) Scanning Electron Micrograph of 130 nm nanoporous glass. The pores are capillary channels of a given diameter. (b) Schematic of water confined in a capillary. Evaporation takes place from the ends.

Nanoporous glass is an ideal medium for determining how water's latent heat of vaporization changes with scale. The glass is made of interconnected capillary channels with nanometer scale diameters, Fig. 1a. Water is fully wetting on the pore walls with a contact angle ~0. Vaporization can be throught of as occurring from both sides of the capillaries at once, until the glass is dry, Fig. 1b.

For isothermal, isobaric vaporization of bulk fluid, the latent heat of vaporization, q {J/g}, is given by the well known result $q = h_g - h_l$. Here h_g and h_l are the specific enthaplies {J/g•K} on the vapor and liquid sides of the phase boundary [39]. However, nanoscale systems have high surface area to volume ratios and this gives the interfacial energies an increasingly large effect on material properties [34, 37, 77]. This is true for pure phases, but also for the transitions

between them. Defray and Prigogine (1966) [86] showed that the heat vaporization from spherical surfaces would take the form:

$$q = h_g - h_l - v_s 2\sigma_{lg}/r \qquad (4.1).$$

Here v_s is the specific volume of the fluid {m^3/g}, σ_{lg} is the liquid vapor surface tension {J/m^2}, and r is the radius of the particle {m}. Equation (4.1) assumes that both h_g and h_l are unaffected by the scale of a substance. However, it was recently shown that the enthalpies of pure phases change is affected by surface effects, which increase with the surface area to volume ratio [77, 121].

The change in h_g and h_l with scale can be understood by looking at the total enthalpy of the liquid and vapor phases:

$$\begin{aligned} dH_l &= V_l dp_l + TdS_l + \sigma_{lg} dA_l \\ dH_g &= V_g dp_g + TdS_g \end{aligned} \qquad (4.2).$$

Here H_l and H_g are the enthalpies of the liquid and vapor components of the system {J}, V_l and V_g are the volumes {m^3}, T is the temperature {K}, S_l and S_g are the liquid and vapor phase entropies {J/K} , and A_l is the area of the liquid vapor interface {m^2} where the contribution of the interfacial energy is counted on the liquid side.

At small scale it is known that the surface tension of a substance can vary with the radius of its interface. To first order that variation can be expressed as:

$$\sigma_{lg} = \sigma_0(1-2\delta/r) \qquad (4.3),$$

where σ_o is the bulk surface tension and δ is the Tolman length [e.g. 36, 41]. The sign of δ can be positive or negative depending on the curvature of the interface.

For vaporization of a wetting fluid from a capillary, surface tension and interfacial curvature cause p_l to decrease relative to the bulk state. The same is also true for the equilibrium vapor pressure in the gas phase. Surface tension causes a decrease in pressure across the liquid-gas interface, and the curvature of the interface. These changes also affect the entropy of the respective phases. Equations (4.1, 4.2) can then be integrated to give the change in enthalpy due to surface effects:

$$\begin{aligned} \Delta H_l &= \int_{P_o - P_c}^{P_o} V_l \, dp_l + \int_{S_l}^{S_o} T \, dS_l + \int_{A}^{0} \sigma_{lg} \, dA_l \\ \Delta H_g &= \int_{P_g}^{P_o} V_g \, dp_g + \int_{S_g}^{S_o} T \, dS_g \end{aligned} \qquad (4.4).$$

Here P_o and S_o are the pressure and entropy in the absence of a capillary interface, P_c is the capillary pressure, S_g and S_l are the entropy of the gas and

liquid with a capillary interface, with A_l being the area of the interface. If the capillaries are of fixed width, then Eqs. (4.3, 4.4) can be combined and if can be shown (see supplemental information) that:

$$\Delta h_l = \frac{2v_l\sigma_{lg}}{r} - \frac{3v_l\sigma_{lg}}{r} + \frac{12v_l\sigma_{lg}\delta}{r^2} + T\left(-\frac{2\sigma_{lg}}{r}\frac{\partial v_l}{\partial T} + \frac{3v_l}{r}\frac{\partial \sigma_{lg}}{\partial T} - \frac{12v_l\delta}{r^2}\frac{\partial \sigma_{lg}}{\partial T}\right)$$
$$\Delta h_g = \frac{2v_l\sigma_{lg}}{r} - T\left(\frac{2\sigma_{lg}}{r}\frac{\partial v_l}{\partial T} + \frac{2v_l}{r}\frac{\partial \sigma_{lg}}{\partial T}\right) \qquad (4.5),$$

The change in the latent heat of vaporization is then given by:

$$\Delta q = \Delta h_g - \Delta h_l - v_s 2\sigma_{lg}/r \qquad (4.6).$$

To good approximation the Tolman length for the liquid-vapor interface can be estimated using [75]:

$$\delta(D) = \frac{D}{4}\left[\exp\left(\frac{2S_b}{3R}\frac{1}{2D/IR-1}\right)/\left(1-\frac{1}{2D/IR-1}\right)-1\right] \qquad (4.7).$$

Here δ {m} is the Tolman length, D is the diameter of the particle {m}, S_b is the solid-vapor transition entropy {J/mol•K}, R is the ideal gas constant, and IR is the atomic diameter {m}. Respective values for aluminum and tin can be found in the

supplemental information. The Tolman length is negative for concave surfaces and positive for convex ones.

4.3. METHOD

Thermogravimetric analysis was used to measure the latent heat of vaporization of water confined in nanoporous glass. Five different sizes of controlled pore glass were used with the specifications given in Table S1 in the supplemental information. Each sample was saturated with water after which both the bulk and confined water were evaporated together in the thermogravimetric chamber. During evaporation, the heat flow, mass, and temperature were measured simultaneously. These data were used to compute the latent heat of vaporization for the water confined in porous glass.

Nanoporous glass with 5 different pore diameters was used for the measurements. The glass was cleaned and dried as described in the supplemental information before being saturated with water. Two separate runs were made during each thermogravimetric analysis experiment. First, an appropriate evaporating sample run with a rate 10 C/min from 40 C to 80 C for 4 min, then 80 C was maintained for 35 minutes to dry up. Next, the dried sample was run with a rate 10C/min from 40 C to 70 C for 3 minute, then 70 C was maintained for 15 minutes. At the first run, bulk water was evaporated first in the crucible, and then both bulk and confined water was evaporated together. In order

to calculate the actual heat used to evaporate water, the second run was subtracted from the first run. The reason why the temperature was increased linearly up to the temperature we are interested in was to stabilize the sample. In addition, during the runs, to maintain constant around the sample in the chamber, nitrogen gas was released with the rate 50 ml/min, and temperature and mass of the sample were measured simultaneously.

A Mettler Toledo TGA/DSC2 was used for the calorimic measurements. Here the thermal input to the sample, its temperature and mass are all measured simultaneously. The TGA has a temperature resolution of 0.25 K and mass weighting accuracy is 0.005% of the measured mass. Both bulk and confined water are present at the start of each calorimic measurement. Energy balance on the same requires that:

$$\dot{Q} = \dot{m}_{confined}\Delta h_{lv,conf}(T) + \dot{m}_{bulk}\Delta h_{lv,bulk}(T) + \dot{Q}_{heating} \qquad (4.8)$$

Here $\dot{Q}$ is thermal input to the sample {J/sec}, $m_{confined}$ and m_{bulk} are the mass of the water confined in nanoporous glass and bulk water {kg}, h_{lv_bulk} and h_{lv_conf} are the latent heat of vaporization for bulk and confined water respectively {J/kg}, and $\dot{Q}_{heating}$ is the energy per unit time that goes into heating of the glass, water and sample holder {J/sec}.

The mass of the confined water need to calculated as followed:

$$m_{confined} = \rho_{water} \text{ x } (m_{CPG} \text{ x } v_{CPG}) - m_{surface} \quad (4.9)$$

where $m_{confined}$ is mass of confined water in given porous glass {g}, ρ is density of water {g/cm^3}, m_{CPG} is mass of the dried controlled pore glass used each experiment {g}, v_{CPG} is the specific pore volume given in Table.1 {cm^3/g}, and $m_{surface}$ is the mass of water absorbed to the surface of the glass pores. It is typically assumed that a monolayer of water remains on the pore walls after vaporization [122], and this was confirmed gravimetrically (see supplemental information).

Equation (4.8) can be integrated over time to get the latent heat of vaporization of the water confined from the nanoporous glass:

$$h_{lv,confined} = \frac{\left(Q - Q_{heating}\right) - \left(m_{total} - m_{confined}\right) \cdot h_{lv,bulk}}{m_{confined}} \quad (4.10)$$

The calorimic measurement of $h_{lv,\ confined}$ was repeated ten times for each diameter of nanoporous glass. The heat flux as a function of time from one of these measurements is shown in Fig. 4.2.

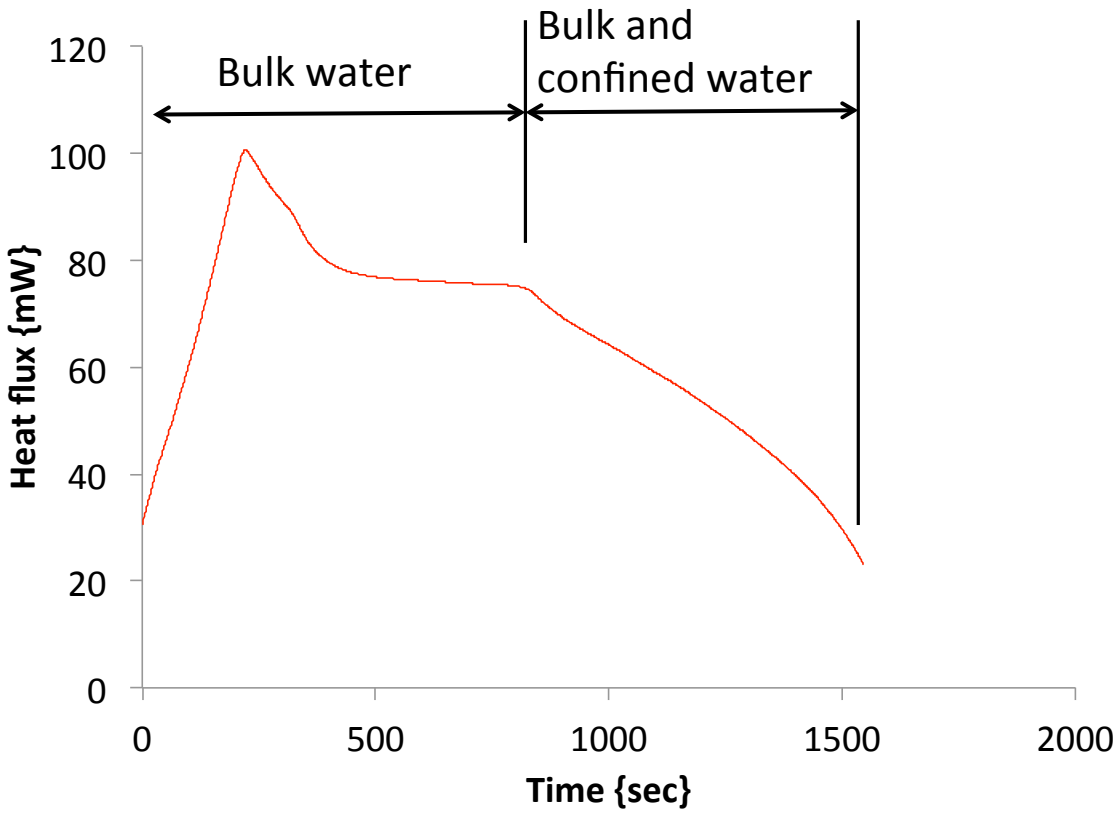

Figure 4.2. Heat fluxes given to the sample. This graph shows the heat flux supplied to the sample, 33nm CPG. For the calculation of $h_{lv,confined}$, in Eq. 4.10, the heat after about 900 seconds was used where bulk and confined water vaporize together.

4.4. Results and Discussion

Figure 4.3 shows the measured latent heats of vaporization for water as a function pore radius, along with the predictions of Eqs. (4.5-7). The values are

the average from the ten individual measurements made at each diameter. The error bars are internal standard deviations from these measurements. The predicted and measured values have an R^2 of 0.92. The experimental result shows that the latent heats of vaporization for water in nano-porous glass increases as the radius of the pores decrease. When the pore diameter is 130 nm, there was no distinct difference compared to the latent heat of vaporization at bulk state. However, when the diameter of pore is 7.5nm the latent heat of vaporization is ~5% greater than that of the bulk state and theory predicts that it will increase rapidly form there.

Equations (4.5, 4.6) assume that δ is constant. Equation (4.7) shows only a 4% increase between 130 and 7.5 nm (see supplemental information), which is consistent with this assumption. The model given by Eqs. (4.5-7) slightly over predicts the change in the latent heat of vaporization at the smallest scale. Here we have assumed that the sign of the Tolman length is negative, which is a common assumption for concave surfaces. This has the effect of increasing the surface tension as scale is reduced, which drives up the predicted value of Δq. However, the sign of the Tolman length remains an open question, and if a positive value is instead used, the Eqs. (5-7) predict the measured data with an R^2 of 0.96. In addition, Eq. (4.2) is only approximate and this is particularly true at very small scale, which can also distort the predicted values of Δq. That said, Eqs. (4.5-7) do remarkably well in predicted the behavior of water as small scale. The small

effect seen by changing the sign of δ underscores that scale dependent changes to the surface tension are second order effects on the latent heat of vaporization.

While Eqs. (4.5-7) were derived to understand the vaporization of water from nanoporous materials, it is applicable to other liquids as well. The limits of integration in Eqs. (4.4) can be changed to predict how the latent heat of vaporization of droplets will change with their scale.

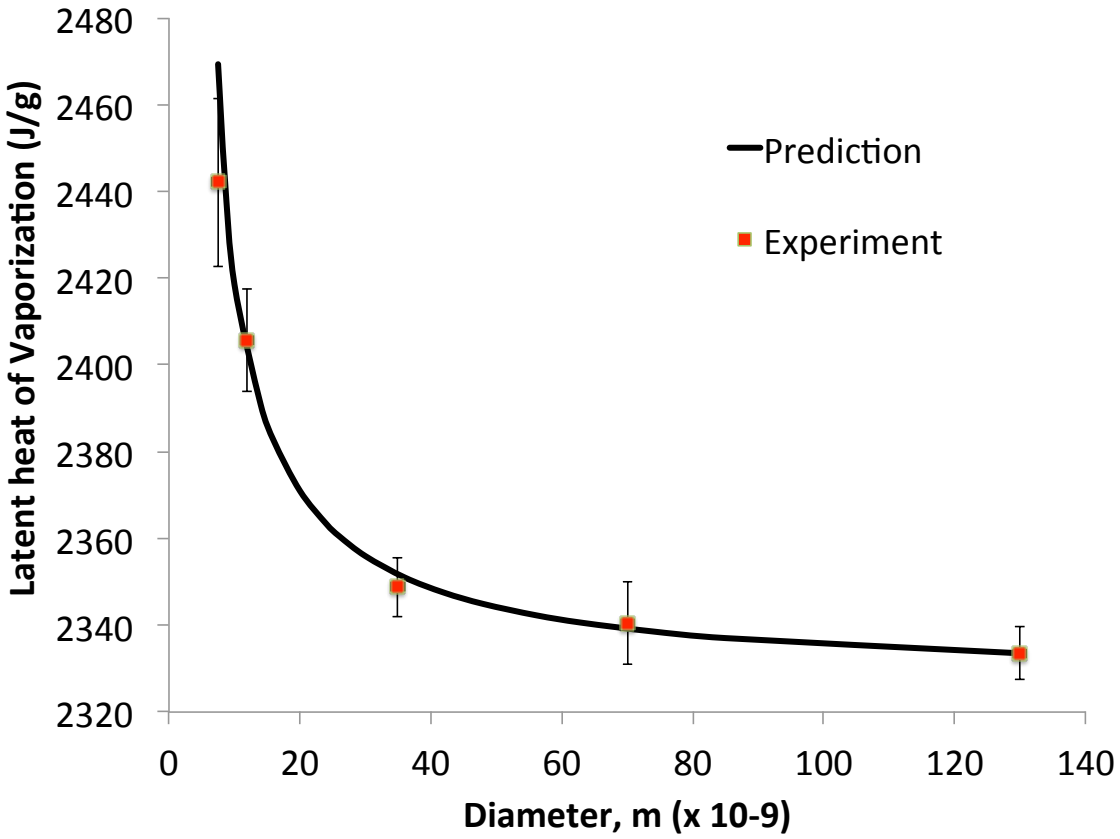

Figure 4.3. Experimental result and theoretical model. Tolman length is -4.7×10^{-11} [123] and liquid thickness is 2.75×10^{-10}.

SUPPLEMENTAL INFORMATION

Specific latent heats of evaporation for water confined in nano pores. The specific heat of evaporation for water confined in nanopores at constant temperature and pressure can be derived as follow. Let Q be the heat required for the phase change

$$Q = \Delta U + P_g \Delta V \quad (4.S1)$$

where U is the internal energy of the system, V is the volume of the pores, and P_g is the constant pressure of the atmosphere that surrounds the pores. Assuming completing evaporation of a mass m {g},

$$\Delta U = mu_g - mu_l \quad (4.S2)$$

$$\Delta V = mv_g - mv_l \quad (4.S3)$$

Thus, heat

$$Q = mu_g - mu_l + P_g (mv_g - mv_l)$$

$$q = h_g - u_l - p_g v_l \quad (4.S4)$$

Capillary pressure is $P_g - P_l = 2\sigma_{lg} / r$ (4.S5)

$$q = h_g - u_l - \left(P_l + \frac{2\sigma}{r}\right)v_l = h_g - h_l - \frac{2\sigma v_l}{r} \quad (4.S6)$$

$dU = TdS - P_l dV_l - P_g dV_g + \sigma dA$ (4.S7)

Here, σdA term works between two phases.

Vapor part: $dH_g = TdS_g + V_g dP_g \rightarrow \Delta H_g = \int_{S_g}^{S_o} T\, dS_g + \int_{P_g}^{P_o} V_g dP$ (4.S8)

Liquid part: $dH_l = TdS_l + V_l dP_l + \sigma dA \rightarrow \Delta H_l = \int_{S_l}^{S_o} T\, dS_l + \int_{P_o - P_c}^{P_o} V_l dP + \int_A^0 \sigma\, dA$

(4.S9)

A. Vapor state

$$\Delta h_g = T\Delta s_g + RT\ln\frac{P_o}{P_g} = T\Delta s_g + \frac{2\sigma v_l}{r} \quad (4.S10)$$

Here,

$$\Delta s_g = -\frac{\partial \Delta G_g}{\partial T} = -\frac{\partial}{\partial T}\left(\int_{P_g}^{P_o}\frac{RT}{P}dP\right) = -\frac{\partial}{\partial T}\left(RT\ln\frac{P_o}{P_g}\right)$$

$$= -\frac{\partial}{\partial T}\left(\frac{2\sigma v_l}{r}\right) = -\frac{2\sigma}{r}\frac{\partial v_l}{\partial T} - \frac{2v_l}{r}\frac{\partial \sigma}{\partial T} \quad (4.S11)$$

Therefore,

$$\Delta h_g = T\Delta s_g + RT\ln\frac{P_o}{P_g} = \frac{2\sigma v_l}{r} - T\left(\frac{2\sigma}{r}\frac{\partial v_l}{\partial T} + \frac{2v_l}{r}\frac{\partial \sigma}{\partial T}\right) \quad (4.S12)$$

This is same with the equation in the Prigogine.

B. Liquid State.

Eq. S9 is below:

$$\Delta H_l = \int_{S_l}^{S_o} T\,dS + \int_{P_o-P_c}^{P_o} V_l\,dP + \int_A^0 \sigma\left(1-\frac{2\delta}{r}\right)dA \tag{4.S13}$$

By integrating it, the specific enthalpy change for liquid is below:

$$\Delta h_l = v_l P_c + T\Delta s_l - \frac{3v_l\sigma}{r} + \frac{12v_l\sigma\delta}{r^2} \tag{4.S14}$$

Here,

$$\Delta s_l = -\frac{\partial \Delta G_l}{\partial T} = -\frac{\partial}{\partial T}\left(\int_{P_o-P_c}^{P_o} v_l\,dP + \int_A^0 \sigma\,dA\right) = -P_c\frac{\partial v_l}{\partial T} + \frac{3v_l}{r}\frac{\partial\sigma}{\partial T} - \frac{12v_l\delta}{r^2}\frac{\partial\sigma}{\partial T} \tag{4.S15}$$

Therefore, if Eq. S5 is plugged into Eq. S4, we have

$$\begin{aligned}\Delta h_l &= v_l P_c + T\Delta s - \frac{3v_l\sigma}{r} + \frac{12v_l\sigma\delta}{r^2} \\ &= v_l P_c - \frac{3v_l\sigma}{r} + \frac{12v_l\sigma\delta}{r^2} + T\left(-P_c\frac{\partial v_l}{\partial T} + \frac{3v_l}{r}\frac{\partial\sigma}{\partial T} - \frac{12v_l\delta}{r^2}\frac{\partial\sigma}{\partial T}\right)\end{aligned} \tag{4.S16}$$

The equation (4.S12) and (4.S16) are plugged into (4.S6).

Tolman length as a function of diameter. The Tolman length for the liquid-solid, liquid-vapor and solid-vapor surface tensions for water can be determined using [75]

$$\delta(D) = \frac{D}{4}\left[\exp\left(\frac{2S_b}{3R}\frac{1}{2D/IR-1}\right)/\left(1-\frac{1}{2D/IR-1}\right)-1\right] \qquad (4.S17)$$

Here D is the diameter of the pores {m}, S_b is the of the solid-vapor transition entropy {J/mol•K}, R is the ideal gas constant, and IR is the atomic diameter {m}.

Material	***IR* (nm)**	***H*$_{LV}$ (kJ/mol)**	T_b (K)	S_b (=H_{LV}/T_b) (J/mol K)
Water (H_2O)	0.096	13.6	373.13	36.5

Table 4.S1. Properties for water for Eq. (4.S17). IR is the atomic diameter, H_{LV} is the latent heat of vaporization of bulk water, T_b is boiling temperature, and S_b is the entropy.

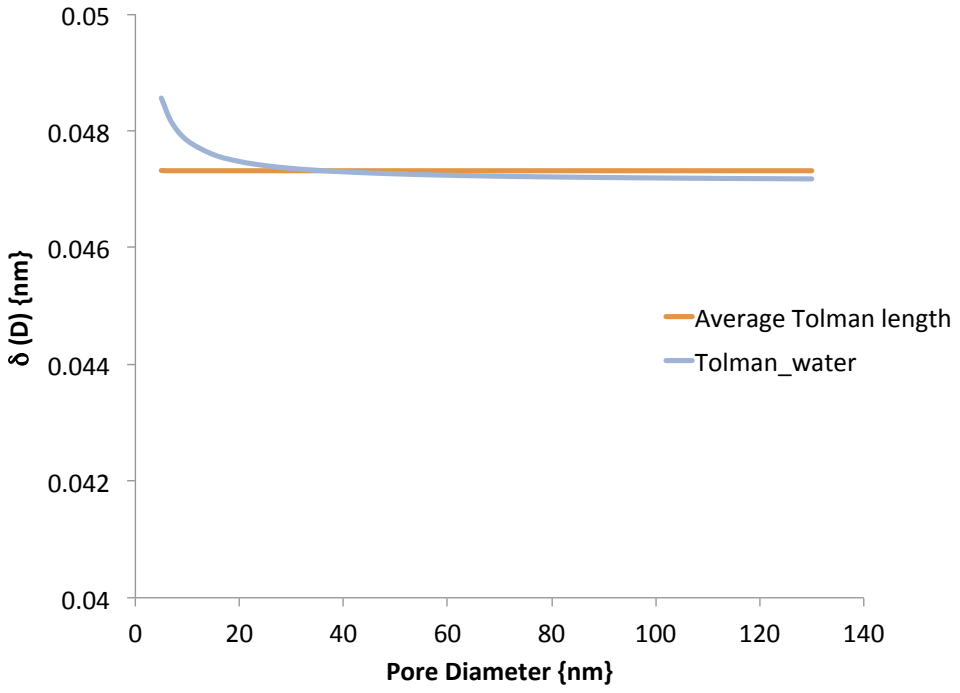

Figure 4.S1. Tolman length as a function of pore diameter. This figure shows the variation of the Tolman length of water with the pore diameter change. Equation (4.S17) is used to calculate Tolman length with properties in Table 4.S1.

Experiment.

Materials. The controlled pore glasses (CPG) used for this experiment were available commercially from *Sigma Aldrich* and *EMD Millipore*, and they were 5

different sizes of CPGs (7.5nm, 12nm, 33nm, 70nm, and 130nm). The specifications of CPGs are listed in the Table 4.S2.

Mean Pore Diameter (nm)	Distribution (%)	Specific surface area (m^2/g)	Pore volume (cc/g)
7.5	20.0	340	0.4
12.0	10.0	210	0.5
33.0	7.6	68	1.15
70.0	10.0	36	0.8
130.0	8.4	24	1.19

Table 4.S2. The specifications for CPG.

Sample preparation. Hydrogen peroxide (H_2O_2) was used to clean the Controlled Pore Glass (CPG). The CPG was then put in hydrogen peroxide (H_2O_2) and heat at 100 C for 10 hours, after which was washed with de-ionized water copiously. After washing it, the CPG was put in nitric acid (HNO_3) for 24 hours in a vacuum chamber, then washed with de-ionized water and dried on heating plate at 150 C for 10 hours. Figure 4.S2 shows the way how the CPG was saturated with distilled water.

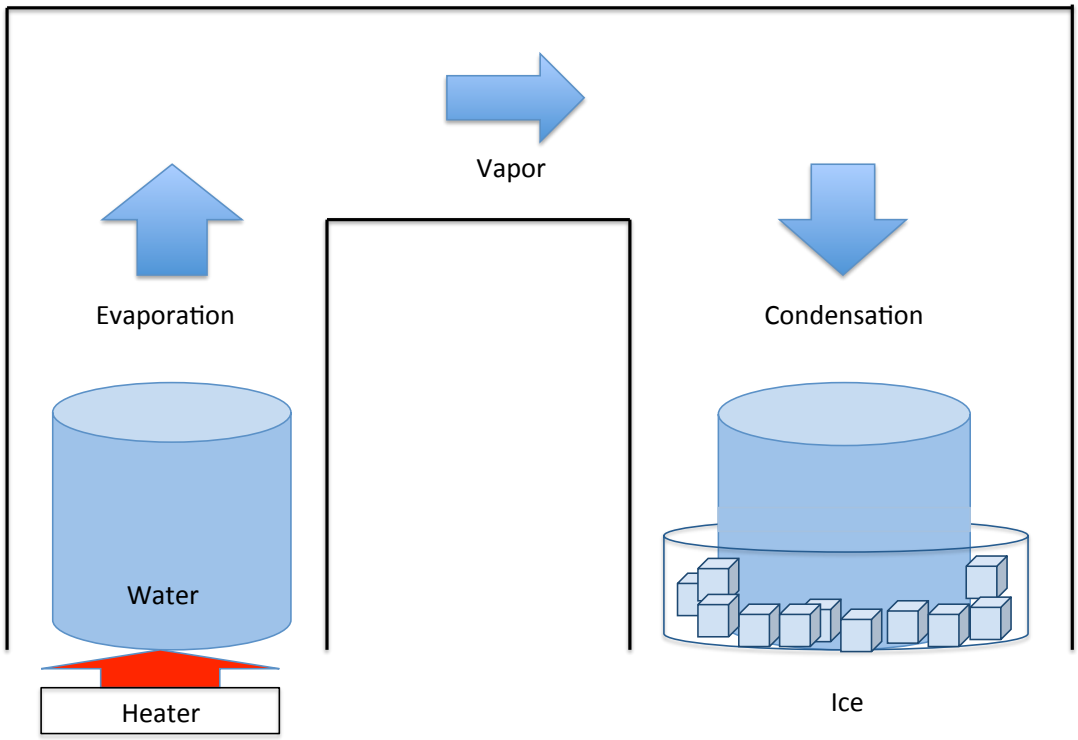

Figure 4.S2. Simple chamber to induce water condensation in pores of CPG. In the chamber, distilled water was vaporized by heating to make high humidity in the chamber at one side and dried CPG was put in small beaker cooling to induce the condensation in the pores and around them for 5 hours.

In this procedure, condensation process could be visualized with ESEM (Environmental Scanning Electron microscopy) located at TMI, the University of Texas at Austin. In the ESEM chamber, at 4 C, humidity around the sample was increased and water vapor was adsorbed in and on the controlled pore glass. The condensation process could be pictured as shown in Fig. 4.S3. The schematic of the sample including the pore glass confining water and bulk water is shown in Fig. 4.S4.

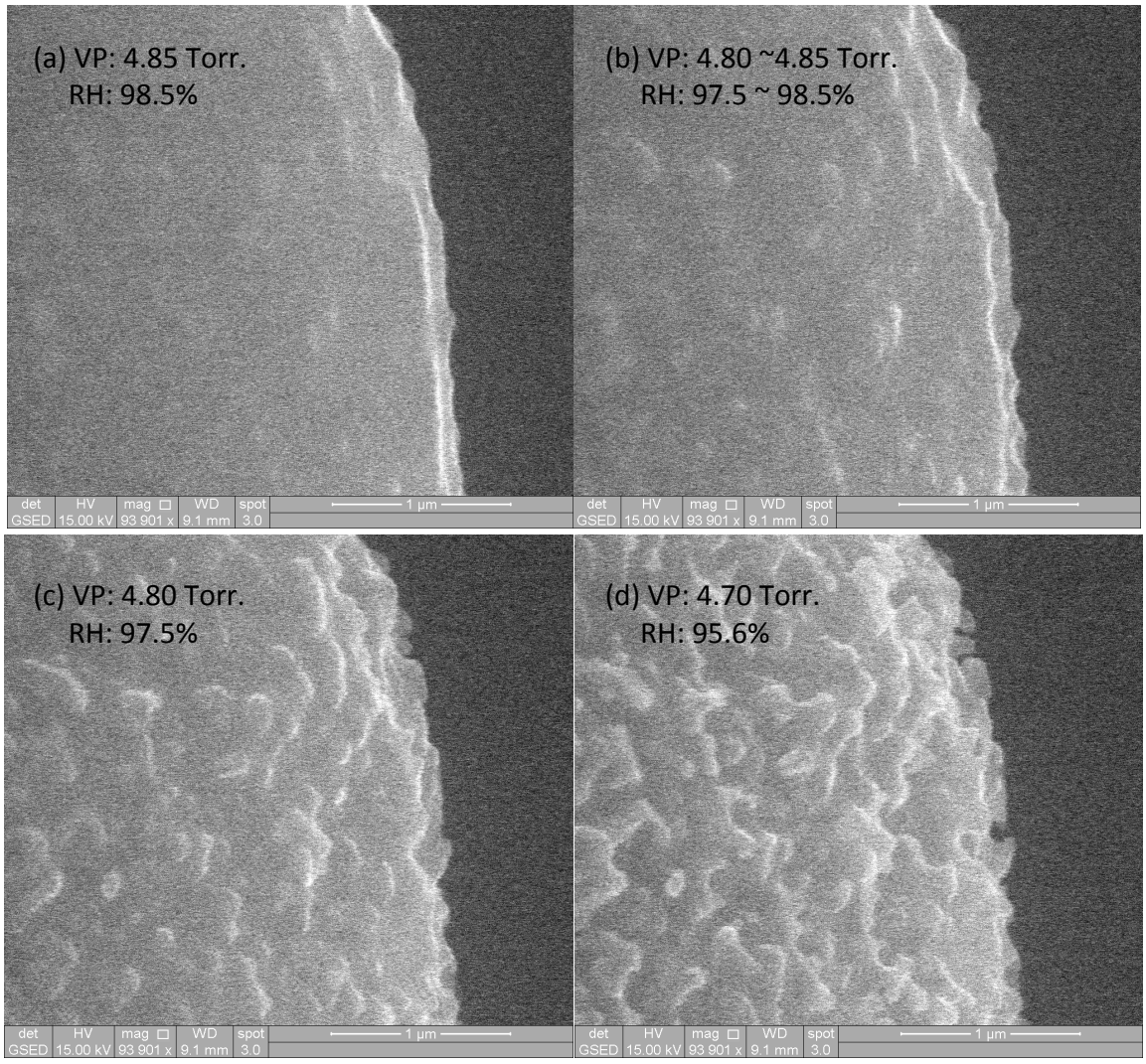

Figure 4.S3. This figure shows x93901 magnified images for evaporation from 130 nm CPG. By changing pressure from 4.85 Torr. To 4.70 Torr. at 4C, the relative humidity changes from 98.5 % to 95.6 %. From this image, it is possible to see in-situ evaporation from the CPG particle. (VP: Vapor Pressure, RH: Relative Humidity)

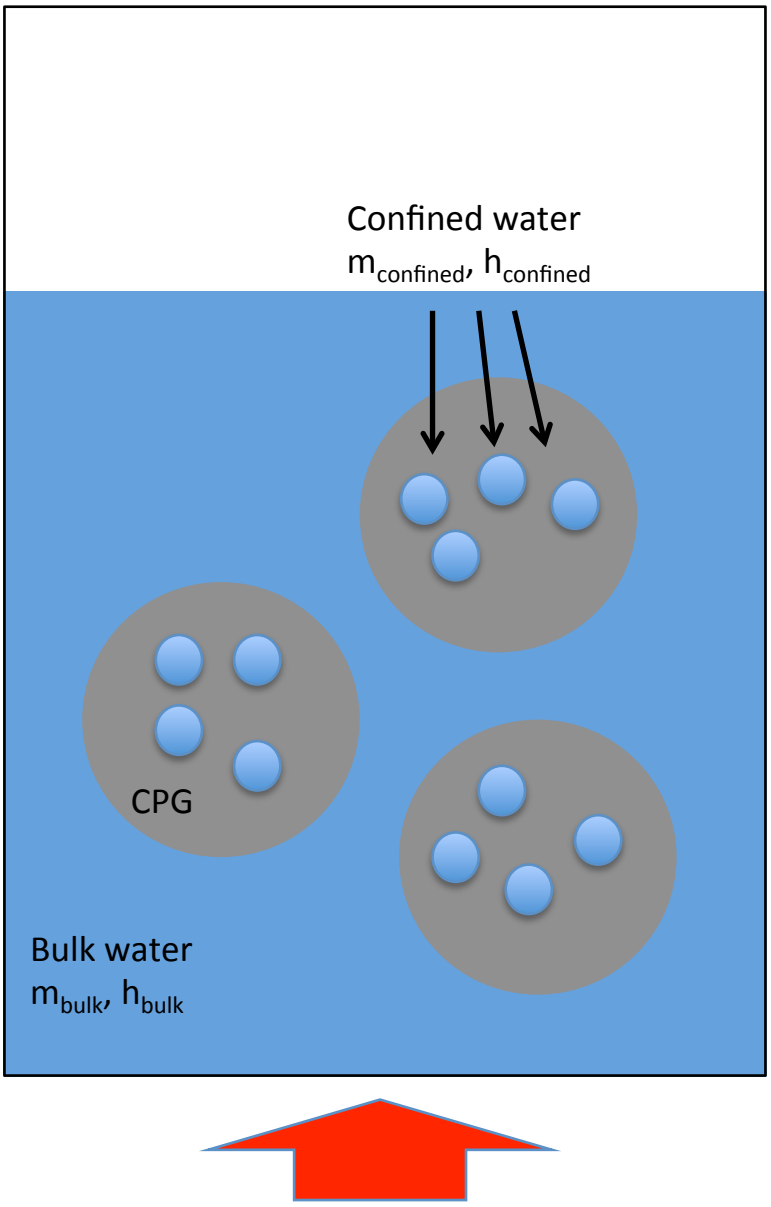

Figure 4.S4. Schematic of the sample with prepared CPG. The 70 μl alumina crucible was filled with the CPG with water (confined and bulk water).

Then, the CPG was put in degassed and distilled water and located in vacuum chamber at room temperature for 24 hours to be saturated and to prevent from any contamination. Since bulk water is covering CPG and pores, the water in pores is not evaporated.

Data Calculation

With experimental data, the latent heat of vaporization of confined water in Controlled Pore Glass (CPG) was calculated. TGA provides mass change {g} vs. time {sec}, Heat flux {mW} vs. time {sec} and Temperature {K} vs. time {sec}, and they are shown in Fig. 4.S5, Fig. 4.2, and Fig. 4.S6, respectively. In the crucible, bulk water and the water confined in pores starts to evaporate together from about 900 seconds. Since the specific heat of CPG (~ 0.84 J/g.K) is smaller than that of water (~4.186 J/g.K), the sample temperature increases and the TGA system decreases the heat flux to maintain the setting temperature.

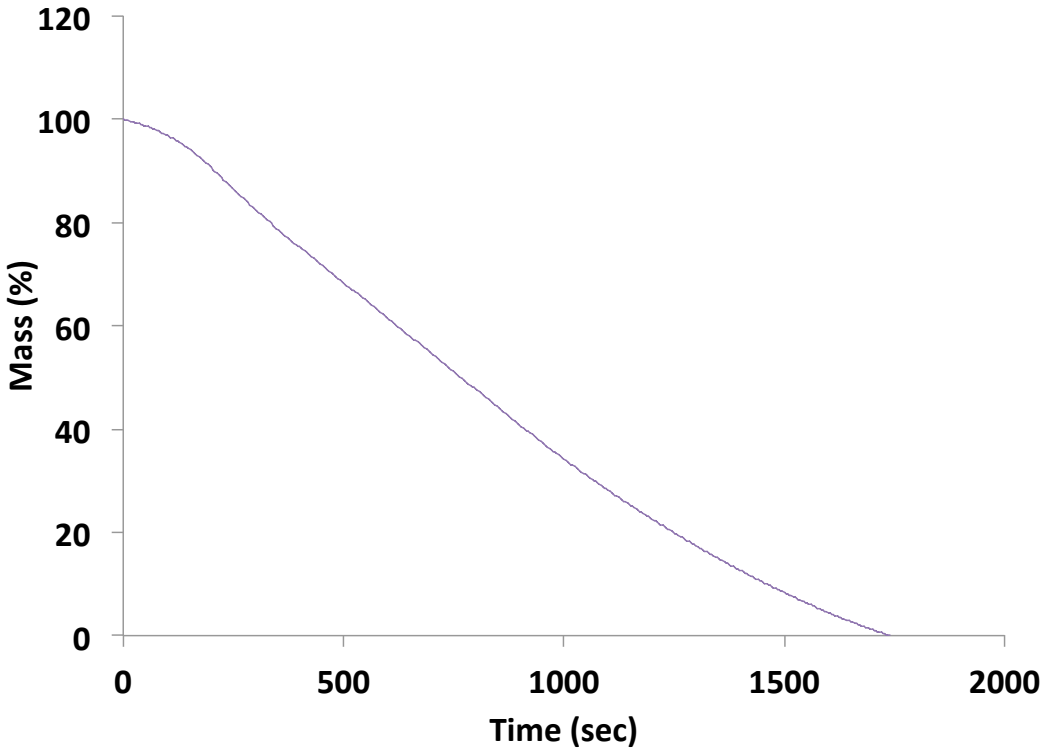

Figure 4.S5. Mass change of water in the crucible in percentage (%). The slope is not straight because of the change of the exposed area of water being vaporized. This data is for 33 nm CPG.

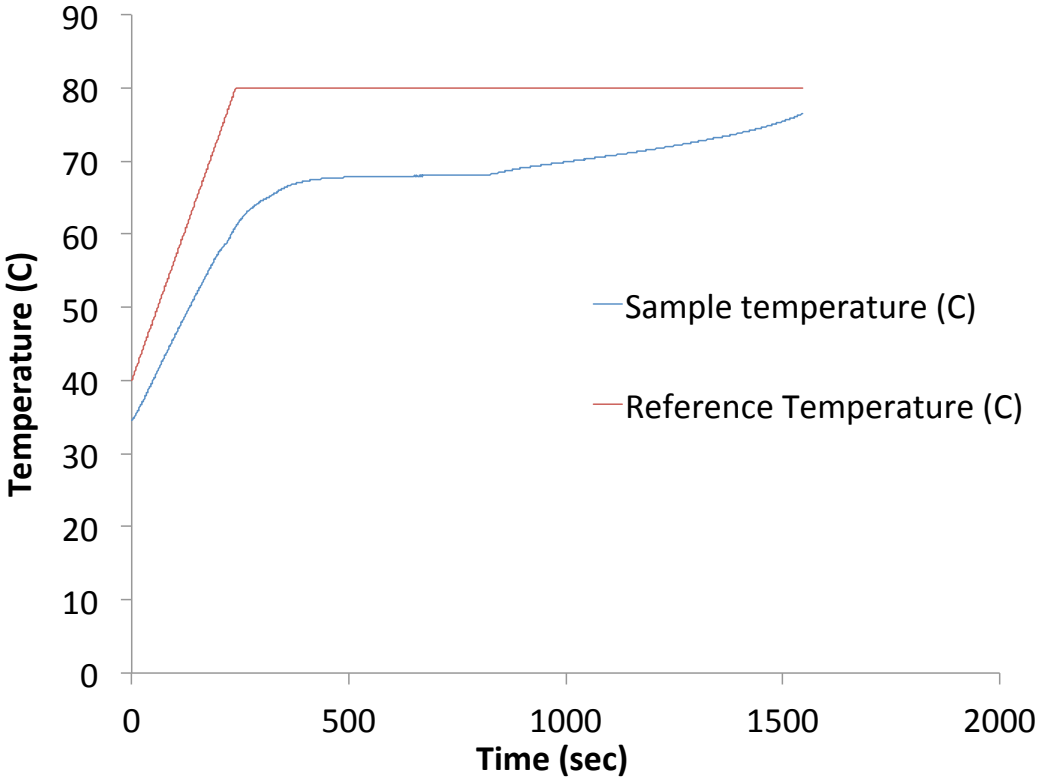

Figure 4.S6. Reference temperature (°C) in red and sample temperature (°C) in blue in the chamber of the TGA system. Red line, setting temperature increases linearly and maintains set temperature. Blue line, sample temperature follows the trend of the setting temperature, but there is a gap between two temperatures because of the conductivity, and vaporization process of the sample. This data is for 33 nm CPG.

The given heat, Q is related to the mass of water in the TGA as:

$$Q = \Delta m_{confined} \Delta h_{lv,conf}(T) + \Delta m_{bulk} \Delta h_{lv,bulk}(T) + Q_{heating} \quad (4.S18)$$

Here, $\Delta m_{confined}$ is the mass change of the water confined in CPG, Δm_{bulk} is the mass change of bulk water, $\Delta h_{lv,conf}$ is the latent heat of vaporization of the water confined in pores, h_{lv_bulk} is the latent heat of vaporization of bulk water, and $Q_{heating}$ is the heat usage because of temperature change.

$Q_{heating}$ from equation (1) is calculated as below:

$$Q_{heating} = m_{CPG} \cdot C_{glass}(T) \cdot (T - T_{const}) + m_{water} \cdot C_{water}(T) \cdot (T - T_{const}) + m_{container} \cdot C_{container}(T) \cdot (T - T_{const})$$

(4.S19)

where m_{CPG}, m_{water}, and $m_{container}$ are the mass of CPG, the mass of water and the mass of crucible, respectively. C_{glass}, C_{water} and $C_{container}$ are the specific heats of CPG, water, and crucible, respectively and given at Table 4.S2 and 4.S3.

The specific heats for water and glass are given below:

Temperature (K)	Cp of water (J/g K)
333.15	4.18
353.15	4.19
373.15	4.22

Table 4.S3. Specific heat of water [124].

Temperature (K)	Cp of glass (J/g K)
273	0.70
373	0.85

Table 4.S4. Specific heat of glass [103].

To estimate the mass of the water confined in pores of CPG, we use the specific volume, (v_{CPG}) which is given by the manufacture. After the running of TGA and sample is dried, the mass of the dried CPG is measured. The pore volume of CPG is calculated as:

$$V_{pore} = m_{CPG} \times v_{CPG} \qquad (4.S20).$$

Here, V_{pore} is the pore volume and m_{CPG} is the mass of CPG in the sample.
And the mass of water confined in pores will be:

$$m_{confined} = \rho_{water} \times V_{pore} - m_{surface} \qquad (4.S21).$$

It is known and tested that liquid layer exists on the surface of the CPG. The thickness of liquid layer is about one molecular diameter, 2.75×10^{-10} {m}. The mass of liquid layer is $m_{absorbed}$.

Liquid layer check

It is known that thin liquid layer exists on the surface of pore structure [122]. The liquid layer is not vaporizable at around 70 C, and it affects the latent heat of vaporization of water confined in pore structure. Thus, checking whether liquid layer exists on the surface of pore structure is worth calculating the latent heat of vaporization. The test was performed with 0.5 g of 33 nm CPG. The amount of CPG used for TGA test was not enough to check the liquid layer because of the limitations of resolution of measurement tools.

About 0.5 g of dried CPG was used to check whether there is a liquid layer on pore structure. After saturated CPG was prepared, the CPG was dried at 70 C on hotplate until CPG dries and the mass of dried CPG was measured, m_{CPG_before}. The CPG dried at 70 C was dried again in the oven. The setting temperature of the oven was 250 C and it was dried for 15 hrs. The mass of CPG dried in the oven is m_{CPG_after}.

$$m_{surface} = m_{CPG\_before} - m_{CPG\_after} \quad (4.S22)$$

Here, m_{CPG_before} is the mass of CPG before putting in the oven at 250 C for 15 hrs, and m_{CPG_after} is the mass of CPG after being dried in the oven.

From the test, $m_{difference}$ was ***0.01020 g*** right after getting it from the oven. As time goes, the difference of the mass was decreasing to ***0.00290g*** in about 5 minutes. The reason must be condensation inside and outside of pores.

The equation for expecting mass of liquid layer of water on the surface is below:

$$m_{difference} = \rho_{water} \cdot m_{CPG} \cdot a_{surface-CPG} \cdot t_{liquid\_layer} \quad \text{(4.S23).}$$

where m_{CPG} is the mass of dried CPG, a_{suface_CPG} is the specific area of CPG (m^2/g), 68 m^2/g, and t_{liquid_layer} is expecting adsorbed liquid layer, one molecular diameter of water (~ 2.75×10^{-10} m) [125]. If it is assumed that the thickness of liquid layer on the surface of pores is one molecular diameter. $m_{difference}$ = 980 {kg/m^3} x 0.5 {g} x 68 {kg/m^3} x 2.75×10^{-10} {m} ~ 9.16 {mg}

Uncertainty Analysis for $h_{lv,confined}$

Since $h_{lv,confined}$ involves multiple parameters, applying error propagation equation is given below[126]:

$$\left(\sigma_{h_{lv,confined}}\right)^2 = \left(\frac{\partial h_{lv,confined}}{\partial Q}\right)^2 \left(\sigma_Q\right)^2 + \left(\frac{\partial h_{lv,confined}}{\partial Q_{heating}}\right)^2 \left(\sigma_{Q_{heating}}\right)^2 + \left(\frac{\partial h_{lv,confined}}{\partial m_{total}}\right)^2 \left(\sigma_{m_{total}}\right)^2 + \left(\frac{\partial h_{lv,confined}}{\partial m_{confined}}\right)^2 \left(\sigma_{m_{confined}}\right)^2 + \left(\frac{\partial h_{lv,confined}}{\partial h_{lv}}\right)^2 \left(\sigma_{h_{lv}}\right)^2 + \left(\frac{\partial h_{lv,confined}}{\partial h_{lv,bulk}}\right)^2 \left(\sigma_{h_{lv,bulk}}\right)^2 \quad (4.S24)$$

where parameters are explained in Eq (S23), and the confined mass in pores has to be taken for the uncertainty of pores and confined mass of water. Thus, error propagation for the confined mass is given below:

$$\sigma_{m_{confined}} = \left(\frac{\partial m_{confined}}{\partial m_{CPG}}\right)^2 \left(\sigma_{m_{CPG}}\right)^2 + \left(\frac{\partial m_{confined}}{\partial v_{CPG}}\right)^2 \left(\sigma_{v_{CPG}}\right)^2 + \left(\frac{\partial m_{confined}}{\partial \rho_{water}}\right)^2 \left(\sigma_{\rho_{water}}\right)^2 \quad (4.S25)$$

Uncertainty of these experiments will be

$$\left\langle \sigma^2_{h_{lv,confined}} \right\rangle = \frac{1}{N} \sum \left[\begin{array}{l} \left(\frac{\partial h_{lv,confined}}{\partial Q}\right)^2 \left(\sigma_Q\right)^2 + \left(\frac{\partial h_{lv,confined}}{\partial Q_{heating}}\right)^2 \left(\sigma_{Q_{heating}}\right)^2 + \left(\frac{\partial h_{lv,confined}}{\partial m_{total}}\right)^2 \left(\sigma_{m_{total}}\right)^2 \\ + \left(\frac{\partial h_{lv,confined}}{\partial m_{confined}}\right)^2 \left(\sigma_{m_{confined}}\right)^2 + \left(\frac{\partial h_{lv,confined}}{\partial h_{lv}}\right)^2 \left(\sigma_{h_{lv}}\right)^2 + \left(\frac{\partial h_{lv,confined}}{\partial h_{lv,bulk}}\right)^2 \left(\sigma_{h_{lv,bulk}}\right)^2 \end{array} \right]$$

(4.S26)

Results

Diameter (nm)	$\Delta h_{confined}$ (J/g)	σ_{h_lv} (J/g)
130	2333.53	6.004
70	2340.47	9.438
35	2348.77	6.775
12	2405.69	11.789
7.5	2442.09	19.388

Table 4.S5. Latent heats of vaporization and error. This table shows experimental results for the latent heats of vaporization and calculated errors for five different sizes of radii.

Chapter 5. Non-equilibrium capillary pressures and flow field stability in porous media

5.1. ABSTRACT

It has been known for decades that preferential flow paths can form during the infiltration of water into dry homogeneous media [127]. However, efforts to predict this phenomena using standard theories of multiphase flow, especially water-SiO_2 system in porous media have failed. In particular, attempts have been made to use Richards equation to fully model the development of these flow fields and the non-monotonic moisture profiles they exhibit. Unfortunately, when standard equilibrium relationships for the capillary pressure and transport coefficients are assumed, Richards equation has been shown to be incapable of doing this. However, past experimental works [128, 129] have shown that non-equilibrium capillary pressures will allow Richards' equation to produce the non-monotonic moisture profiles observed. In addition, the capillary pressure overshoot for unstable wetting fronts of viscous fluids was explained with Laplace equation using Hoffman relationship [127]. Here we show how this type of capillary pressure is expected in the wetting front region of a preferential flow field. The results are generated using a thermodynamic model for capillary pressure that

considers the movement of fluid interfaces, and velocity dependent contact angles for water-SiO_2 system.

5.2. INTRODUCTION

A notable feature of preferential flow fields in unsaturated media are the non-monotonic moisture profiles that they often develop [129-131]. Because Richards equation is typically used to describe fluid transport through isothermal, incompressible media, there have been attempts to use it to fully model these types of flow [129, 132-135]. In one-dimension Richards equation can be written as:

$$\frac{\partial \theta}{\partial t} = \frac{\partial}{\partial z} K(\theta) \frac{\partial \Psi}{\partial z} \qquad (5.1).$$

Here $\Psi = h(\theta) + z$ {m} is potential. For water infiltration into air saturated media $h(\theta) = (p_w - p_a)/\rho g$ is the pressure head {m}, with p_w and p_a being the wetting and air pressures {Pa}, ρ the water density and g the gravitational constant. Note that $h(\theta) = -P_c$, where P_c is the capillary pressure. The moisture content of the media is denoted by θ {$cm^3 \bullet cm^{-3}$}, t is time {sec}, z is height above a datum {m} and is taken to be positive up. The hydraulic conductivity of the medium is denoted by $K(\theta)$ {$m^2 \bullet sec^{-1}$}.

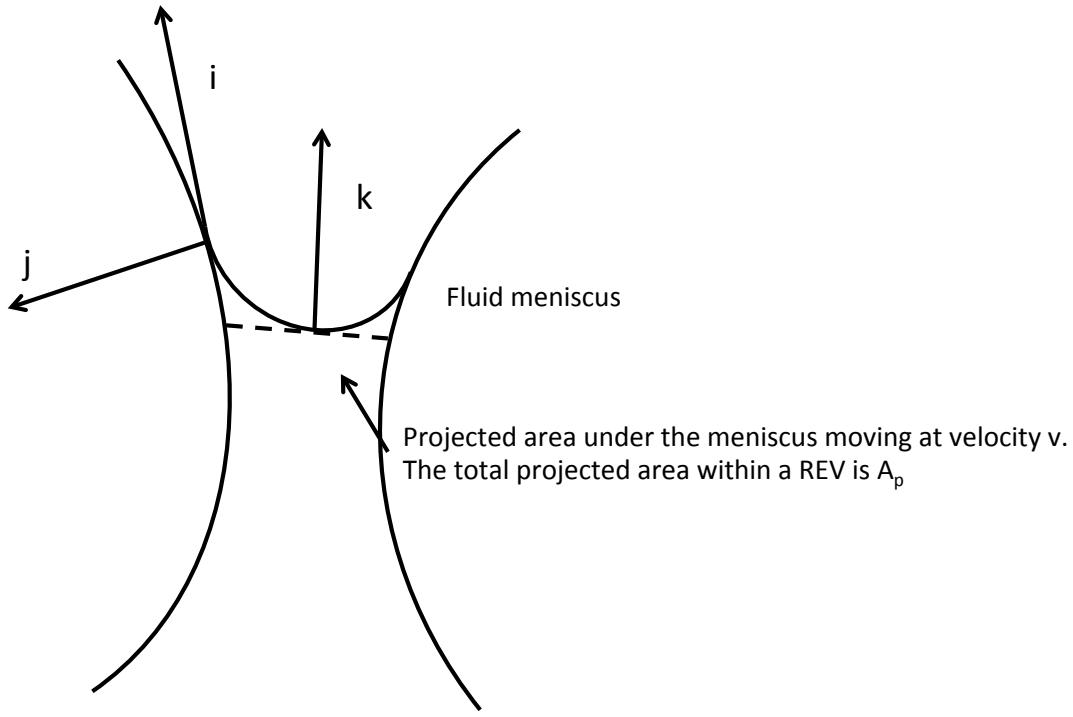

Figure 5.1. Interfacial movement. The projected area, A_p, is shown. Here the contact line force is in the *i* direction and the movement of the interface is in the *k* direction.

It is easy to show that if $K(\theta)\partial\Psi/\partial z$ is monotonic, then $\partial\theta/\partial t$ will be as well. Equation (5.1) can also be written as $\partial\theta/\partial t = \nabla \bullet q$, where $q = -K(\theta)\ \partial\Psi/\partial z$. Expanding the relationship for q:

$$q = -K(\theta)\left(\frac{\partial h}{\partial z}+1\right) = -K(\theta)\left(\frac{\partial h}{\partial \theta}\frac{\partial \theta}{\partial z}+1\right) \qquad (5.2).$$

If p_a is constant, then under equilibrium conditions both $K(\theta)$ and $\partial h/\partial\theta$ are

monotonically increasing functions of moisture content. As a result, if a wetting front profile starts out with $\partial\theta/\partial z<0$, Richard's equation can only produce monotonic increasing value for $\partial\theta/\partial t$. However, if the sign of $\partial h/\partial\theta$ changes during infiltration, then $\partial\theta/\partial t$ can as well [136]. Importantly, numerical integration of Eq. (5.1) in the wetting front region of a preferential flow field produced exactly this type of $\partial h/\partial\theta$ relationship [136-138].

It has been known for decades that interfacial contact angles are velocity dependent [139]. Simulations have shown that the force required to move a contact line through a smooth capillary tube is proportional to v and other studies have obtained predictions of a v^x dependence with x ranging from 0.4 to 9/7 depending on the approach and fluid properties [140, 141]. Previous work has also shown that the motion of fluid interfaces can affect capillary pressure in porous systems [142]. Here we show that velocity dependent contact angles can produce the non-equilibrium $\partial h/\partial\theta$ relationship observed [136-138] in preferential flow fields with a non-monotonic moisture profile.

5.3. CAPILLARY PRESSURE IN A POROUS MEDIUM WITH MOVING CONTACT LINES

It was previously shown that the internal energy of a wetting fluid that enters a region of porous media and displaces a non-wetting fluid can be expressed as [19, 143]:

$$U' = T\,S' - (p_a - p_w)\,V'_w + \sum \sigma_{w,i}\,A'_{w,i} - \langle \alpha\, \boldsymbol{F}\bullet\boldsymbol{v}\quad A_p v\rangle \qquad (5.3).$$

Here U' is the time rate change of the fluid element's internal energy, T is the fluid temperature {K}, S' is the time rate change of the fluid element's entropys, $\sigma_{w,i}$ {J•m^{-2}} and $A'_{w,i}$ {m^2} are the surface tension and time rate change of interfacial area of the wetting fluids in contact with the i'th non-wetting phase, α is the contact line length per unit of cross sectional pore area {m^{-1}}, $\boldsymbol{F}$ is the force exerted by/on the contact line per unit of its length per unit of its velocity {kg•m^{-1}•sec^{-1}}, $\boldsymbol{v}$ is the interfacial velocity {m/sec}, A_p is the cross sectional area of a pore {m^2}, with v its magnitude, Fig. 5.1. The last term on the right hand side of Eq. (5.3) represents an average over a representative elementary volume: $\langle \alpha\, \boldsymbol{F}\bullet\boldsymbol{v}\ A_p v\rangle = \int(\alpha\, \boldsymbol{F}\bullet\boldsymbol{v}\ A_p v)\, dV_{REV} / \int dV_{REV}$, where the integrand in the numerator varies with the size of the pores and the velocity of the interface within them.

For an isothermal process where the entropy and internal energy of the fluid element can be considered to be constant, Eq. (5.3) reduces to:

$$(p_a - p_w)V'_w = \sum \sigma_{w,i}\,A'_{w,i} - \langle \alpha\, \boldsymbol{F}\bullet\boldsymbol{v}\ A_p v\rangle \qquad (5.4).$$

Performing the average for $\langle \alpha\, \boldsymbol{F}\bullet\boldsymbol{v}\ A_p v\rangle$ requires a detailed knowledge of the pore structure and velocity profile within the flow field. However, if we assume that α, $\boldsymbol{F}$, A_p, and v do not vary with position over the volume of the integral, then the work

done per unit time in moving the fluid-solid contact line may be written as α <$\boldsymbol{F}\bullet\boldsymbol{v}$> $A_p v$. By conservation of mass $V'_w = A_p v$ and Eq. (5.4) can be rewritten as:

$$P_c\, V'_w = \sum \sigma_{w,i}\, A'_{w,i} - \alpha\, \langle \boldsymbol{F}\bullet\boldsymbol{v} \rangle V'_w \qquad (5.5).$$

Dividing through by V'_w we get:

$$P_c = \sum \sigma_{w,i}\, (\partial A_{w,i}/\partial V_w)_{u,s,T} - \alpha\, \langle \boldsymbol{F}\bullet\boldsymbol{v} \rangle \qquad (5.6).$$

It has previously been shown that Eq. (5.6) can be written as [19]:

$$P_c = \sum \sigma_{w,i}\, (\partial A_{w,i}/\partial V_w)_{u,s,T} - \tau\, \partial\theta/\partial t \qquad (5.7).$$

When the first term on the right hand side of Eq. (5.7) is set equal to the equilibrium capillary pressure, one gets the result proposed by Hassanizadeh and Gray in 1990 [21]. However, both of the terms on the right hand side of Eq. (5.6) are affected by the motion of a fluid interface. For a single fluid moving through a capillary it can be shown that:

$$\sigma_w \frac{\partial A_w}{\partial V_w} = \frac{2\sigma_w \cos\phi(v)}{r(\theta)} \qquad (5.8)$$

Combining Eqs. (5.7,5.8) we get:

$$P_c = \frac{2\sigma_w \cos\phi(v)}{r(\theta)} - \tau\frac{\partial\theta}{\partial t} \qquad (5.9).$$

Here both terms on the right hand side are functions of moisture content, and interfacial velocity. The parameter τ encompasses the force required to move contact lines through unsaturated medium, and its functional form remains an open question. However, an expression for τ based on dimensional analysis has been proposed [144, 145] that can be used to estiamte the magnitude of this parameter:

$$\tau = \frac{\varepsilon\mu\beta}{k\lambda}\left(P_b\right)^2 \qquad (5.10).$$

Here ε is porosity, μ is the fluid viscosity, and β is 0.1 [145]. The coefficients, λ and P_b are determined by a fit of the Brook-Corey relationship to equilibrium capillary pressure data for a medium [146], and k is the medium's intrinsic permeability [147]. Coefficients and calculated values are in supplemental information.

5.4. DEPENDENCE OF CAPILLARY PRESSURE ON CONTACT LINE VELOCITY

The equilibrium capillary pressure for a 20/30 SiO_2 sand was determined using an 8 day capillary rise experiment. The non-equilibrium capillary pressure was determined using numerical integration of Darcy's law along the centerline of a preferential flow field that was infiltrating into the same medium at constant velocity. Wetting front velocity and flow field moisture content were measured non-invasively using real-time neutron radiography, as was the hydraulic conductivity of the medium [137, 138, 148, 149].

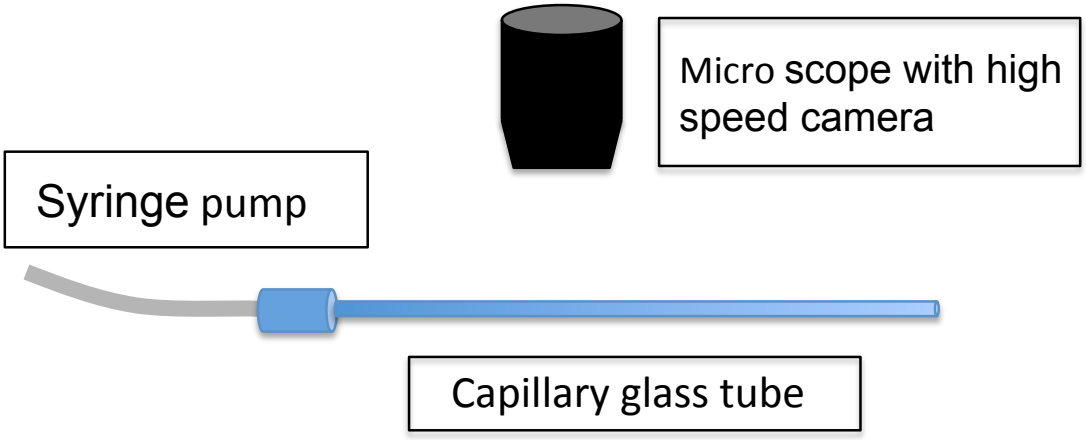

Figure 5.2. Experimental set up to measure the interface angle of water flow in micro glass tube.

The dependence of contect angle on interfacial velocity for water moving across SiO_2 grains was obtained from experiments done in glass capillary tubes. A syringe pump was used to drive an interface through a glass capillary channel at a constant velocity. The interface, and contact angle, were tracked using digital images taken at 1/30th of a second intervals using digital microscopy. The images were then processed to give the contact angle. Additional details can be found in the supplemental information. The experiments show that the fluid-solid contact angle in an air-water system is proportional to *v {cm/s}*, Fig. 5.2:

$$\phi = 30 + 50.08 v^{0.13} \qquad (5.11).$$

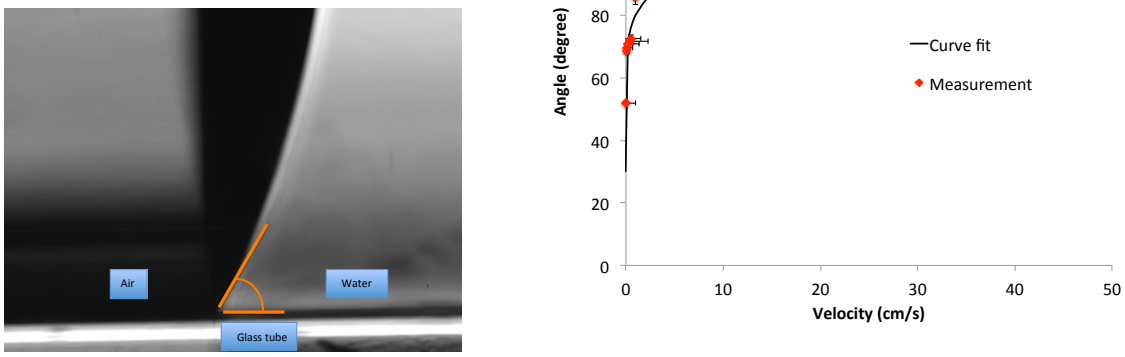

Figure 5.3. Interface angle vs. velocity of water front from the capillary glass experiment. The curve fit is ø = 30 + 50.08 v $^{0.13}$, where v is in {cm/s}.

The change in contact angle was also found to be the same whether the channel has a uniform diameter or one that changes width. Previous studies have found the equilibrium contact angle of water on glass beads are small, with values from 0.00 to 0.40 rad being used [150-152].

Interface angles were measured by varying the velocity of the water flow through glass capillary tubes and compared with Hoffman's model [139]. However, Hoffman model shows the limitation to describe the interface angle of water flow as shown in the Figure. One of the reasons might be that the Hoffman's model deals with only viscous fluids (e.g. G.E. Silicon SF-96, Brookfield Silicone, Dow Corning Silicone, Ashland Chemical Admex, and Santicizer). The limitation was also explained with other recent articles [153] and suggested advanced model for water interface angle and the result is also shown in the figure

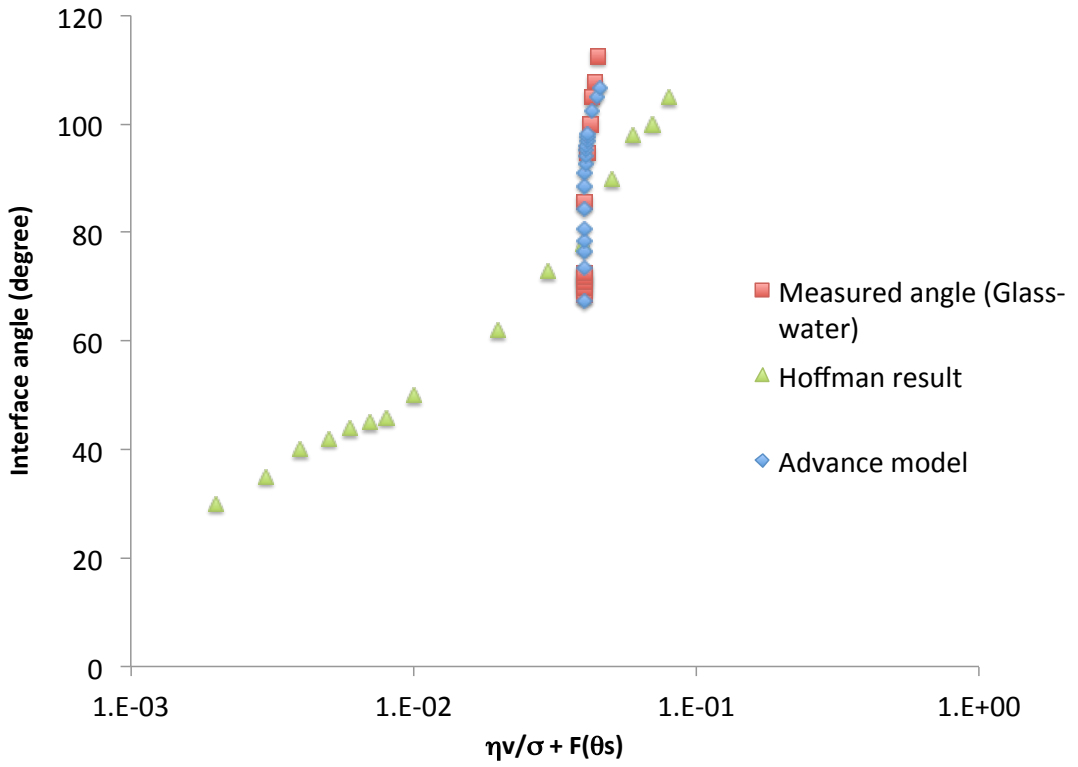

Figure 5.4. This figure shows the data from Hoffman [139], advance model [153] and measured angle. For the comparison, viscosity h is 0.001 {Pa.s}, surface tension of water s is 0. 072 {N/m}. And 0.04 was used for $F(q_s)$ of measured angle and advanced model [153].

***Contact line velocity*.** When pores fill with water, they often do so rapidly in what is often sometimes called a 'Haines jump' and it has been noted that this can be the dominant mechanism for pore filling in preferential flow [130]. At high capillary numbers it has also been noted pore filling becomes smoother again [154]. Regardless, in the wetting front region of a preferential flow field, pore filling would

cause interfacial velocities that would result in a decrease in capillary pressure relative to its equilibrium value.

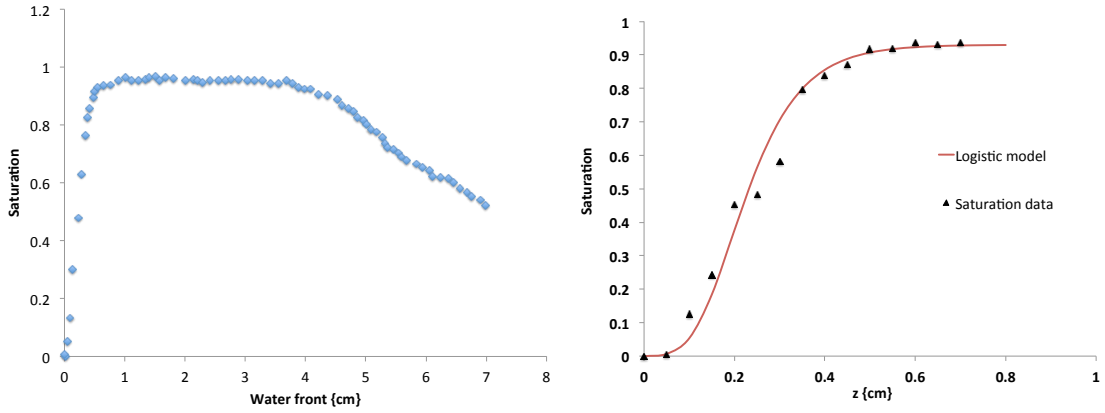

Figure 5.5. Wetting front profile in a constant velocity finger. The saturation profile for a finger that was moving through 20/30 sieve SiO_2 sand at 0.19 cm/sec.

Figure 5.3 shows the saturation profile for a preferential flow field traveling through dry 20/30 SiO_2 sand at constant velocity. The average velocity at which interfaces move through pores can be determined using:

$$\frac{dS}{dt} = v_w \frac{dS}{dz} = \frac{A_P v}{\theta_s} \qquad (5.12),$$

where v_w is the wetting front velocity {m/sec}, S the saturation $\{\theta/\theta_s\}$, and θ_s is the saturated moisture content. Rearranging Eq. (5.11) gives the interfacial velocity in terms of the cross sectional pore area, saturated moisture content, wetting front velocity and the slow of the saturation profile.

Cross sectional pore area. The cross sectional area, A_p, can be determined from the pore size distribution of the media, which can itself be determined using a capillary rise experiment, which gives the equilibrium capillary pressure moisture content relationship $P_c(S)$. Here the pore radius is given by [150, 151]:

$$r(S) = \frac{2\sigma\cos(\phi)}{P_c(S)} \qquad (5.13).$$

Here $r(S)$ is the radius of the smallest pores filled at a particular capillary pressure. If one assumes that the pores are spherical then the number of these pores can also be found using data from a capillary rise experiment:

$$N(S) = \int \frac{\theta_s f(r)}{V_p} dr \qquad (5.14),$$

where $f(r)=d\theta/dr$ $\{m^{-1}\}$ [155]. The cross sectional area distribution is then given by:

$$A_p(S) = N(S) * \pi r^2(S) \quad (5.15).$$

Additional details on A_p, v, and $\phi(v)$ can be found in the supplemental information.

5.5. RESULTS AND DISCUSSION

Figure 5.4 shows a comparison of data on equilibrium capillary pressure versus saturation for a 20/30 SiO_2, along with data for the capillary pressure in the wetting front region of the preferential flow field moving through the same medium. Not only does the non-equilibrium capillary pressure drop more quick than does its equilibrium value, but it is also non-monotonic, as is the saturation profile shown in Fig. 5.3.

Both of the terms on the right hand side contribute to the non-equilibrium capillary pressure. However, a fit of the Brooks and Corey relationship to the capillary rise data gave a P_b of 10^{-4} m and a λ of 2.45. The Intrinsic permeability of the medium was 1.95×10^{-9} m^2. This means that the magnitude of $\tau\ \partial\theta/\partial t$ is extremely small and that $P_c = 2\sigma_w \cos(\phi)/r(S)$. In fact this has been proposed previously [156], but here is given a precise basis. This functional form for the non-equilibrium capillary pressure is velocity dependent, and can handle both wetting and drying behavior.

When Eq. (5.12) is combined with the distribution for $A_p(S)$, and data on the wetting front velocity and saturation gradient, we get the average interfacial velocity, *v,* as a function of saturation, Fig. 5.5. The saturation dependent velocity affects the contact angle and the capillary pressure as given by Eqs. (5.7,5.9). Figure 5.6 shows the measured non-equilibrium capillary pressure along with the prediction of Eq. (5.9) when the second term on the right is ignored.

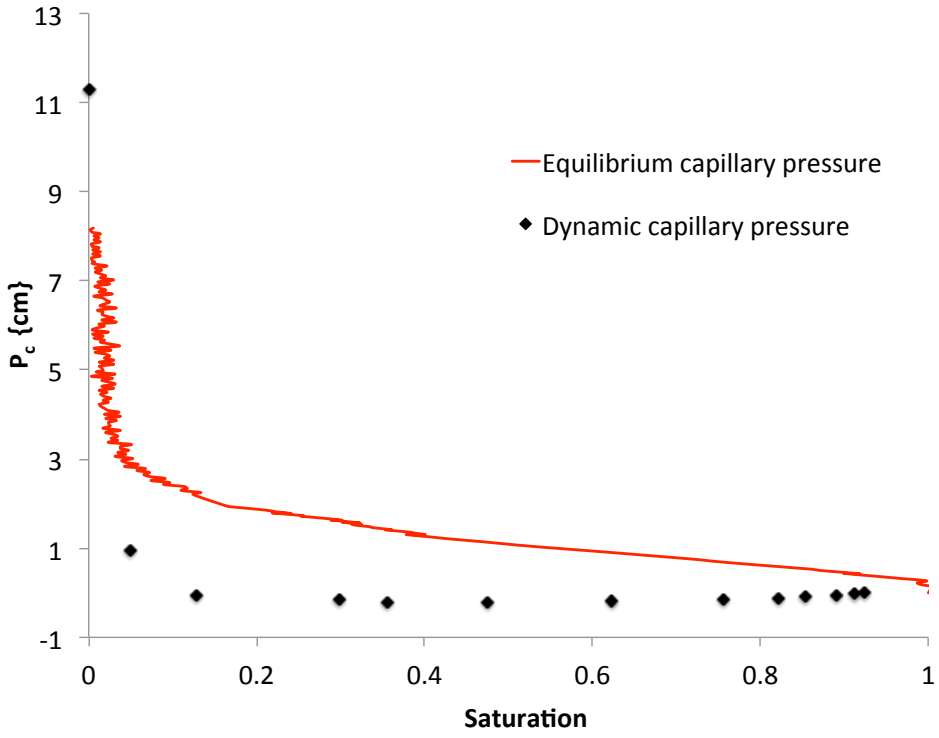

Figure 5.6. Dynamic and equilibrium capillary pressures. The dynamic capillary pressure was determined using numerical integration of Darcy's law along the centerline of a preferential flow field that was infiltrating into dry SiO_2 sand at constant velocity. Wetting front velocity and flow field moisture content were measured non-invasively using real-time neutron radiography, as was the hydraulic conductivity of the medium. The dynamic capillary pressure drops abruptly across the leading edge of the wetting front, reaches a minimum at between S ~ 0.5, and then begins to rise again. The equilibrium capillary pressure drops monotonically.

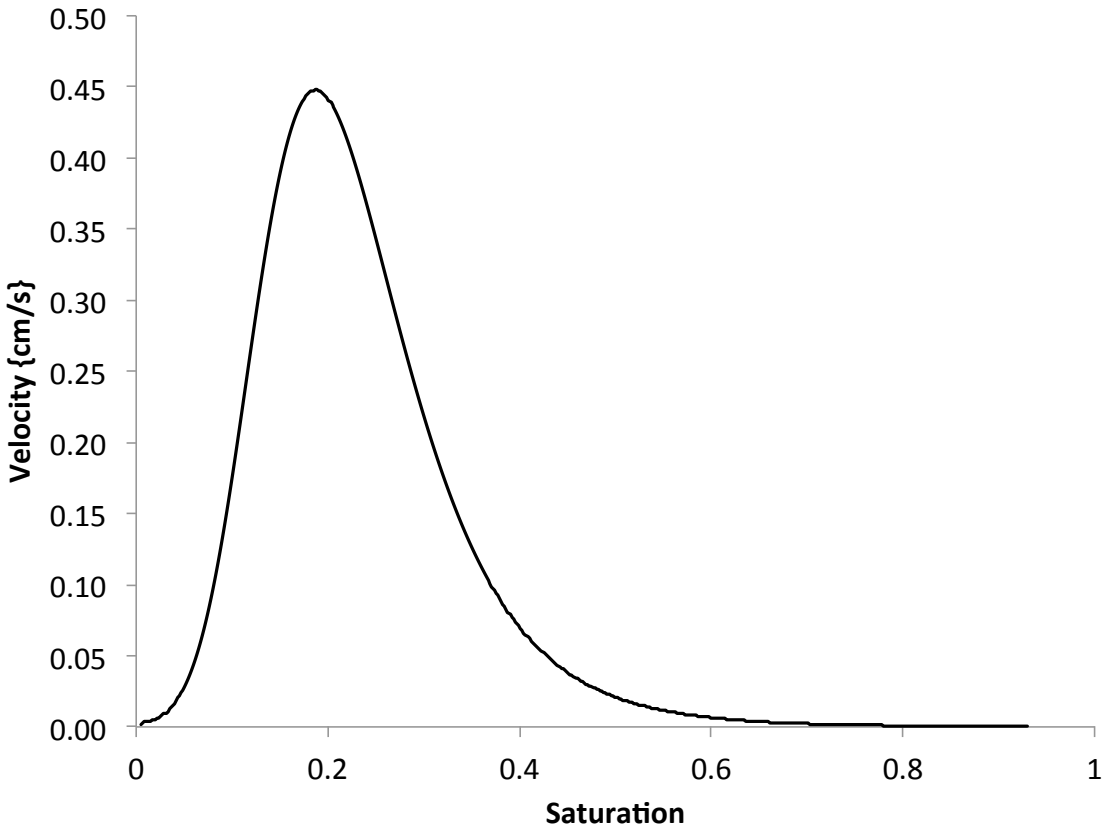

Figure 5.7. Interfacial velocity as a function of saturation.

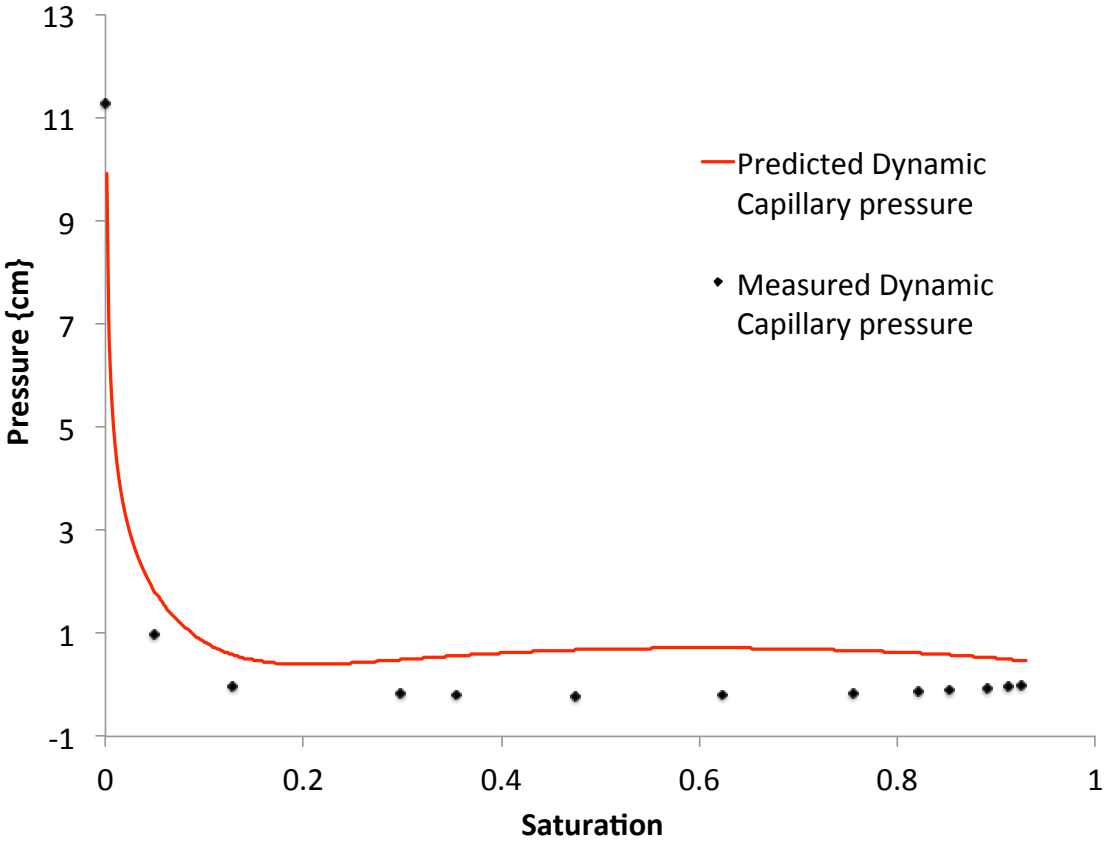

Figure 5.8. Dynamic Capillary pressure. Predicted dynamic capillary pressure and measured capillary pressure shows agreement. Predicted capillary is the sum of equilibrium capillary and dynamic term.

The correlation between theory and experiment in Fig. 5.6 shows that velocity dependent contact angles can be a dominant factor in the formation of non-equilibrium capillary pressures in porous media. Other studies have investigated situations where τ can have much larger values that it does for the course grained media from which the data were drawn here. Importantly, the ability of these

capillaries pressures to form non-monotonic saturation dependence is also what is required by Eq. (5.2) for the onset of drainage behind the wetting front, which can also clearly be seen in Fig. 5.3.

SUPPLEMENTAL INFORMATION

Equilibrium and non-equilibrium capillary pressure data were determined for the same medium and reported in [19, 137, 138]. The equilibrium data is shown in Fig. 5.1 along with the best fit of the van Gecutchen model [157]:

$$S = \left[\frac{1}{1 + \left(\alpha P_{c,eq} \right)^n} \right]^m \qquad (5.S1).$$

Here, S is saturation $\{\theta/\theta_s\}$ where θ_s is the saturated moisture content, $P_{c,eq}$ is the equilibrium capillary pressure {m}, and α, m, and n are fitting parameters.

The equilibrium capillary pressure is given by:

$$P_{c,eq}(S) = \frac{2\sigma \cos(\phi)}{r(S)} \qquad (5.S2).$$

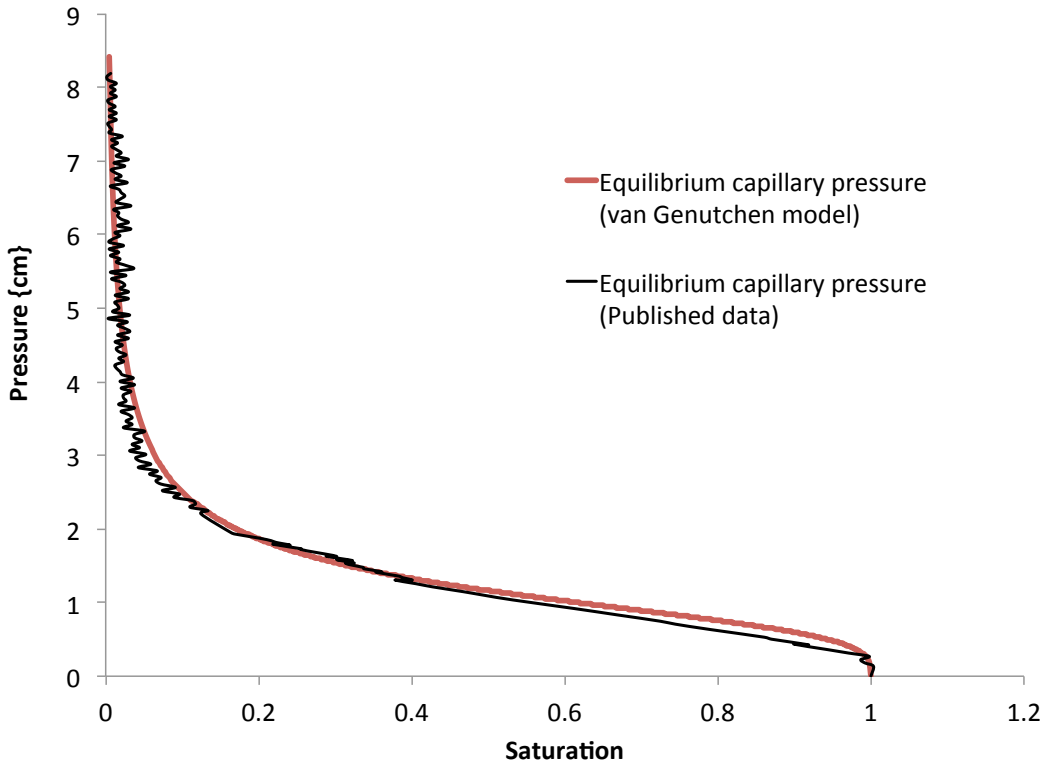

Figure 5.S1. Equilibrium capillary pressure and the best fit of the van Genutchen model graphs. Equilibrium capillary pressure data from [19].

Cross sectional pore area. The cross sectional area, A_p, can be expressed as:

$$A_p(S) = N(S)\,\pi r^2(S) \qquad (5.S3)$$

where $N(S)$ is the number of pores per unit volume at saturation S, and where r(S) can be determined by rearranging Eq. (5.S2). The pore density can also be determined from the capillary rise data:

$$N(S) = \int \frac{\theta_s f(r)}{V_P} dr \qquad (5.S4),$$

where $f(r) = d\theta/dr$, and V_p is the volume of the smallest filled pores at S. The cross sectional Figure 5.S2 shows the cross section pore area distribution as a function of saturation.

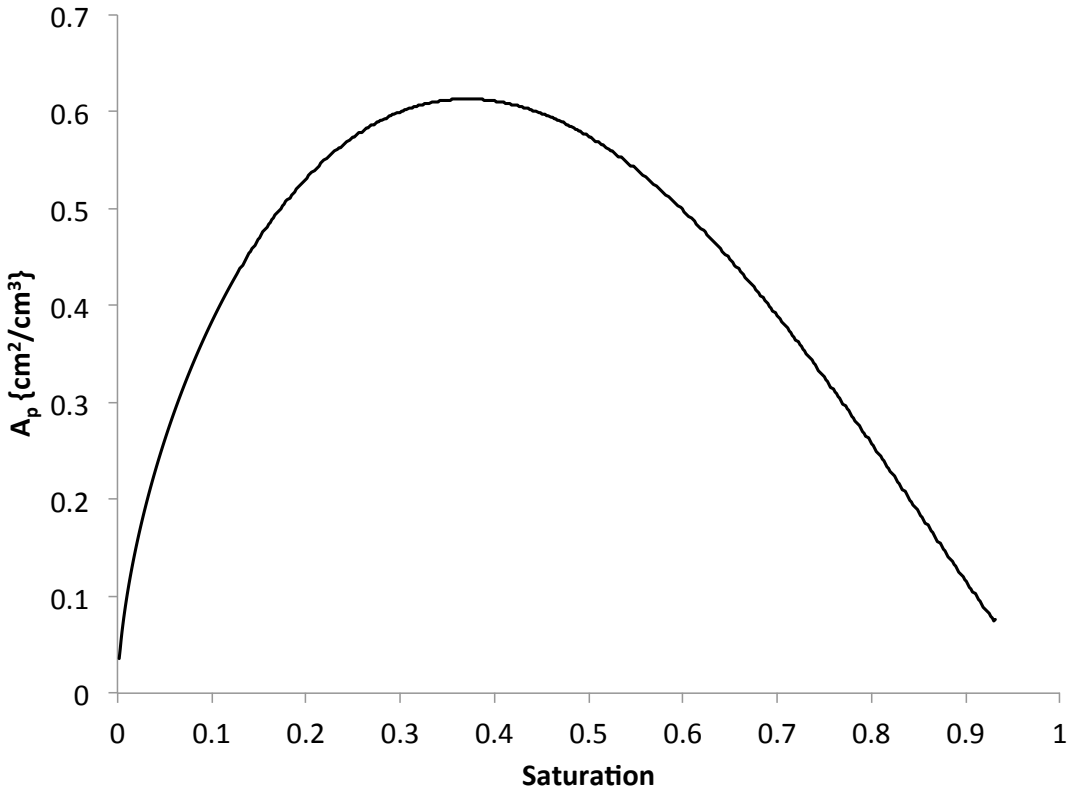

Figure 5.S2. Cross sectional pore area distribution. The cross section area distribution was determined using a capillary rise experiment and πr^2.

Contact line velocity. We assume that fluid-solid contact lines move at the same velocity as fluid interfaces, and that pores fill sequentially from smallest to largest. Then the time rate change in moisture content within the flow field can be written as:

$$\frac{dS}{dt} = v_w \frac{dS}{dz} = \frac{A_P v}{\theta_s} \qquad \text{(5.S5)},$$

where v_w is the wetting front velocity {m/sec}, and v is the average interfacial velocity in the pores that are filling at saturation *S*.

Rearranging Eq. (5.S5) gives the interfacial velocity in terms of the cross sectional pore area, saturated moisture content, wetting front velocity and the slow of the saturation profile. Figure 5.5 shows the saturation profile in the wetting front region of a translating preferential flow field [137, 138].

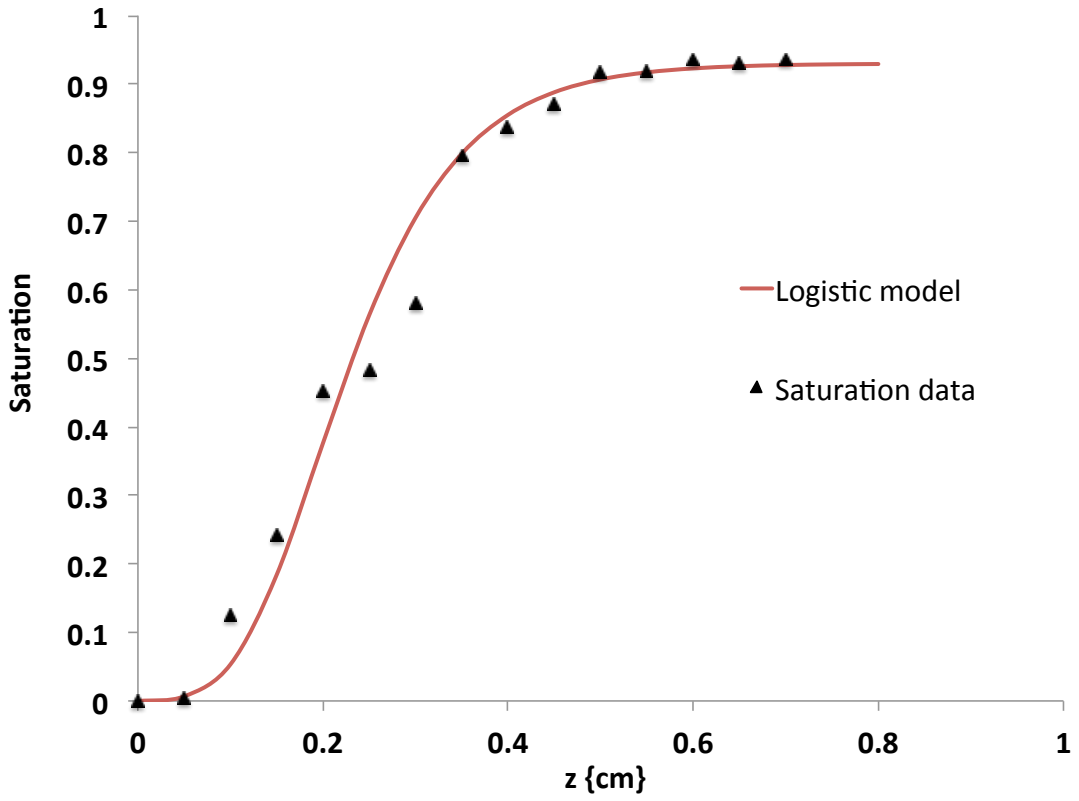

Figure 5.S3. Wetting front profile in a constant velocity finger. A generalized logistic function was fit to the data and used to compute dS/dz. The fit has an R^2 = 0.98.

A generalized logistic equation was fit to the data to provide a noise free result for computing dS/dz in Eq. (5.S5):

$$S(z) = A + \frac{K - A}{\left(1 + Qe^{-B(z-M)}\right)^{1/\nu}} \tag{5.S6}$$

Here, S is saturation, z is distance, constants A = 0, K = 0.93, Q = 0.51, B =12, M = 0, and ν = 0.05.

Velocity dependent contact angle. The dependence of contact angle on interfacial velocity for water moving across SiO_2 grains was obtained from experiments done in SiO_2 capillary tubes. A syringe pump was used to drive an interface through a glass capillary channel at a constant velocity. The interface, and contact angle, were tracked using digital images taken at 1/30th of a second intervals using digital microscopy. The images were then processed to give the contact angle, Fig. 5.S4.

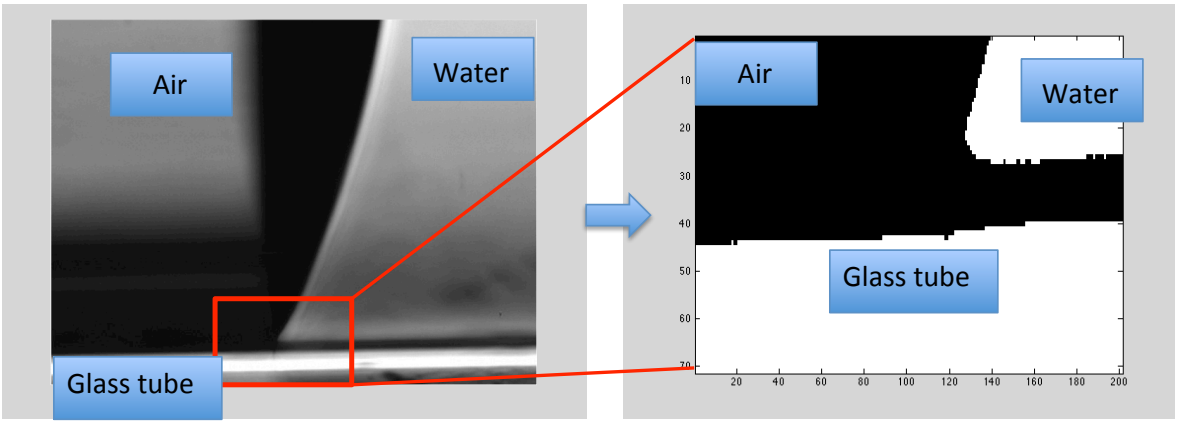

Figure 5.S4. Original image is altered to binary numbered image. Left figure is original image from the microscope program. The image is altered to binary numbered matrix as shown in right figure with Matlab.

Original images were changed to black & white color images and interfacial boundary was traced using the Matlab function, 'bwtraceboundary', Fig. 5.S5.

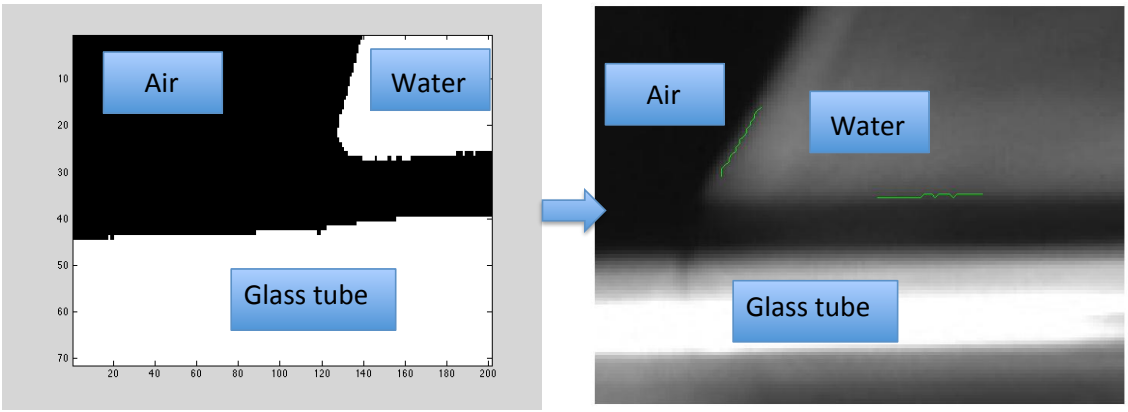

Figure 5.S5. Boundary tracing. The Matlab function 'bwtraceboundary' is used to trace the interfacial boundary. Left figure is binary picture showing interfaces and right figure has green lines drawn by 'bwtraceboundary' command.

In the images, about 20 black points were traced and made by fitting straight line using:

$$\sigma^2 = \sum_{1}^{n} \left(y_n - \left(a_2 \cdot x_n + a_1 \right) \right)^2 \qquad (5.S7)$$

Here, σ is the standard deviation, a_1 & a_2 are the slope and the intercept on y-axis of an arbitrary linear equation. By differenciating the standard deviation respect to a_1 and a_2, the best linear fit was obtained, Fig. 5.S6.

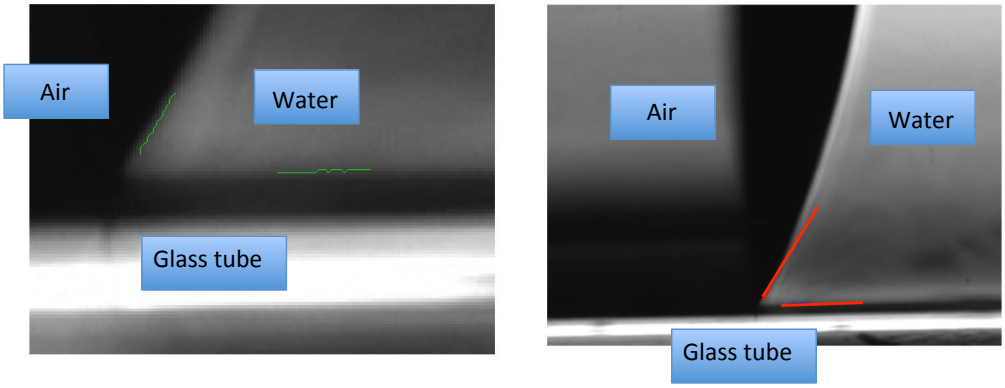

Figure 5.S6. Linear fit. Green lines drawn by 'bwtraceboundary' are altered to linear squared fir lines on right figure.

Contact angles were determined using a dot product between the vectors for the contact line and the surface with which it was in contact using *Image J*, Fig. 5.S7, and were found to be accurate to within 3%.

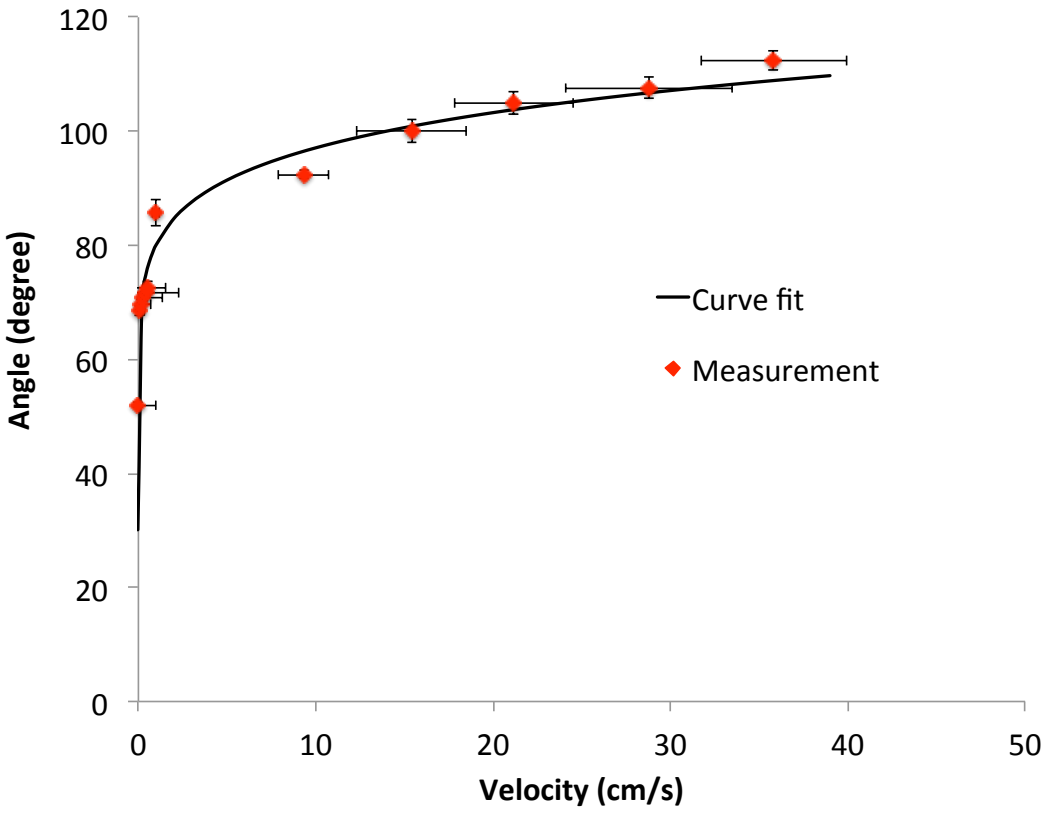

Figure 5.S7. Velocity dependent contact angle. The curve fit is ø = 30 + 50.08 v $^{0.13}$, where velocity is in {cm/s}.

Dynamic term. The functional form of the coefficient τ in the dynamic term on the right hand side of Eq. (5.9) is a matter of debate. However, Dahle et al. [145] proposed using a relationship by Stauffer [144] to estimate its magnitude:

$$\tau = \frac{\varepsilon\mu\beta}{k\lambda}\left(P_b\right)^2 \qquad (5.S8).$$

Here ε is porosity, μ is the viscosity of fluid, and β is 0.1 [145]. The coefficients λ and P_b come from fitting the Brook-Corey relationship [146] to the equilibrium capillary pressure data shown in Fig. 5.S1, and are 2.45 and 0.01 {cm}, respectively. The intrinsic permeability, *k* was obtained from measurements for the hydraulic conductivity of this medium presented in [147]. Figure 5.S8 shows $\tau\, d\theta/dt$ as a function of saturation.

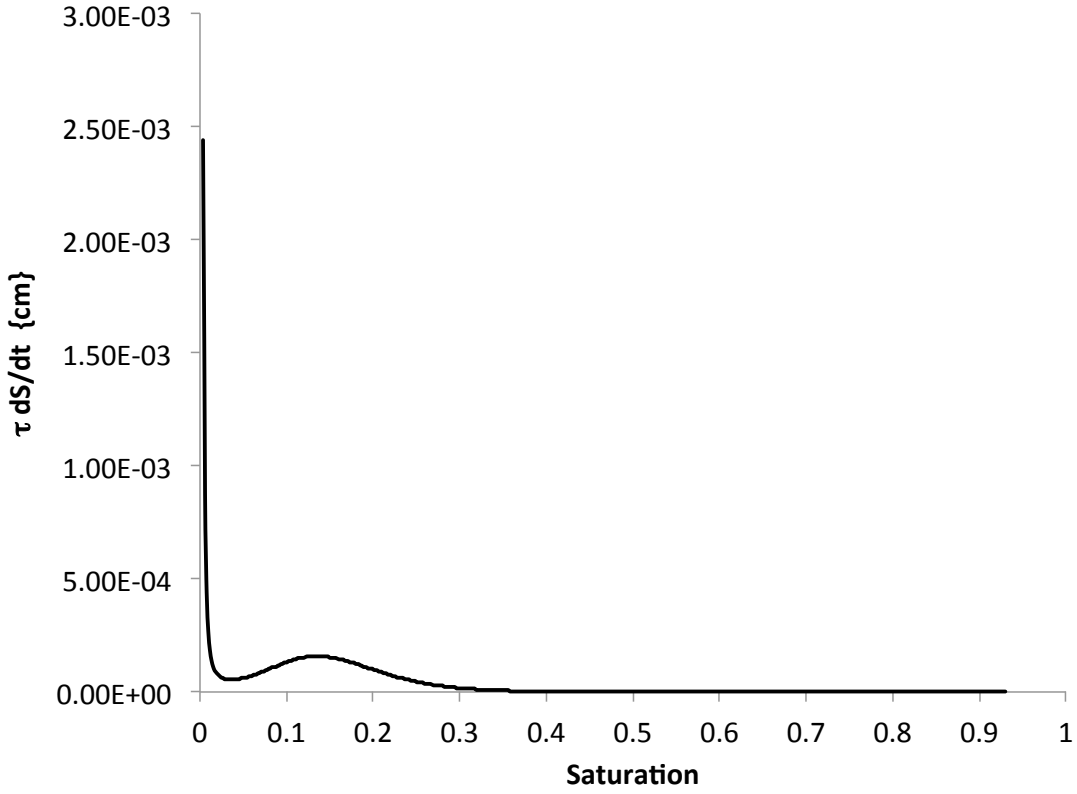

Figure 5.S8. Calculated τdS/dt vs. Saturation.

Chapter 6. Conclusion

The work presented in this dissertation explored the effect of surface tension on the origins of non-equilibrium capillary pressures in porous systems and on changes to the latent heat of phase change in nanoscale substances.

Classical thermodynamic models were used to explain how surface tension affects the latent heat of melting for hydrocarbons confined in nano-pores, and of free-standing nanoparticles with different surface structures. The results were calculated with thermodynamic models for the latent heat of melting for materials confined in nano pores. The predicted changes to the latent heats at nanoscale showed strong agreement with existing experimental results (R^2 values of 0.99, 0.96, and 0.98 for benzene, heptane, and naphthalene, respectively). In addition, a model for the latent heat of melting for free-standing metallic nano particles predicted the change in the latent heat of melting and comparisons with published experimental results (R^2 values of 0.97 and 0.93 for tin and aluminum, respectively.

The same thermodynamic approach was used to predict how the latent heat of vaporization of liquids, specifically water, would change with scale. In order to verify the prediction of the change in latent heat of vaporization of water confined in nano pores, the experiment using thermogravimetric analysis and controlled pore

glass was conducted, and we proved that the prediction and the experimental results have strong correlation each other.

In addition, a model was also derived and analyzed for how non-equilibrium capillary in porous systems depend on contact angle dynamics. The model presented correlated well with published data for non-equilibrium capillary pressures measured in the wetting front region of a preferential flow field.

The developed thermodynamic models explained scale effects on the change of the latent heat of melting and evaporation and they can be applied to predict the phase change in nano scale near surface energy budgets, thermal transport around nuclear repositories, and the development of preferential flow paths around nuclear storage sites. Also, the developed model here explained the origin of non-equilibrium capillary pressure in porous media and has direct application to understanding phase stability in the storage of carbon dioxide in geological media.

Bibliography

1. Sellers, P.J., et al., *Modeling the exchanges of energy, water and carbon between continents and the atmpospher.* Science, 1997. **275**: p. 502-509.
2. Kar, A. and J. Mazumder, *Mathematical model for laser ablation to generate nanoscale and submicrometer-size particles.* Physical Review E, 1994. **49**(1): p. 410.
3. Li, C., et al., *Nanostructured Copper Interfaces for Enhanced Boiling.* Smaa, 2008. **4**(8): p. 1084-1088.
4. Thomson, W., *On the equilibrium of vapour at a curved surface of liquid.* Philosophical Magazine, series 4, 1871. **42**(282): p. 448-452.
5. Jackson, C.L. and G.B. McKenna, *The melting behavior of organic materials confined in porous solids.* Journal of Chemical Physics, 1990. **93**(12): p. 9002-9011.
6. Findenegg, G.H., et al., *Freezing and melting of water confined in silica nanopores.* Chemphyschem, 2008. **9**(18): p. 2651-9.
7. Lai, S.L., et al., *Size-Dependent Melting Properties of Small Tin Particles: Nanocalorimetric Measurements.* Physical Review Letters, 1996. **77**: p. 99-102.
8. Sun, J. and S.L. Simon, *The melting behavior of aluminum nanoparticles.* Thermochimica acta, 2007. **463**.
9. Defay, R. and I. Prigogine, *Surface tension and adsorption*. 1966, New York: Wiley.
10. Deinert, M.R., J.-Y. Parlange, and K.B. Cady, *Silplified thermodynamic model for equilibrium capillary pressure in a fractal porous medium.* Physical Review E, 2005. **72**: p. 041203.
11. Hassanizadeh, S.M. and W.G. Gray, *Thermodynamic Basis of Capillary Pressure in Porous media.* Water resource research, 1993. **29**(10): p. 3389-3405.
12. Weitz, D.A., et al., *Dynamic Capillary Pressure in Porous Media: Origin of the Viscous-Fingering Length Scale.* Physical Review Letters, 1987. **59**(26): p. 2967-2970.
13. Washburn, E.W., *The Dynamics of Capillary Flow.* Physical review, 1921. **17**: p. 273.

14. Stroock, A.D. and T.D. Wheeler, *The transpiration of water at negative pressures in a synthetic tree.* Nature, 2008. **455**: p. 208-212.
15. Deinert, M.R., J.Y. Parlange, and K.B. Cady, *Capillary pressure in a porous medium with separate pore volume and pore surface fractal dimensions.* Physical Review E, 2008. **77**: p. 021203.
16. Perrier, E., et al., *Models of the water retention curve for soils with fractal pore size distriubutions.* Water Resources Research, 1996. **32**(10): p. 3025-3031.
17. Rieu, M. and G. Sposito, *Fractal Fragmentation, Soil Porosity, and Soil-Water Properties .1. Theory.* Soil Science Society of America Journal, 1991. **55**(5): p. 1231-1238.
18. Tyler, S.W. and S.W. Wheatcraft, *Fractal processes in soil water retention.* Water Resources Research, 1990. **26**(5): p. 1047-1054.
19. Deinert, M.R., J.Y. Parlange, and K.B. Cady, *Simplified model for equilibrium capillary pressure in a fractal porous medium.* Physical Review E, 2005. **72**: p. 041203.
20. Hassanizadeh, S.M. and A.Y. Beliaev, *A theoretical model for hysteresis and dynamic effects in the capillary relations for two-phase flow in porous media.* Transport in Porous media, 2001. **43**: p. 487-510.
21. Hassanizadeh, S.M. and W.G. Gray, *Mechanics and thermodynamics of multiphase flow in porous media including interphase boundaries.* Advances in Water Resources, 1990. **13**: p. 169-186.
22. Deinert, M.R. and J.Y. Parlange, *Effect of pore structure on capillary condensation in a porous medium.* Physical Review E, 2009. **79**: p. 053901.
23. Fisher, L.R., R.A. Gamble, and J. Middlehurst, *The Kelivin equation and the capillary condensation of water.* Nature, 1981. **290**: p. 575-576.
24. Yin, Y., *Adsorption isotherm on fractally porous materials.* Lanmuir, 1991. **7**: p. 216-217.
25. Qiao, Y. and H. Christenson, *Direct observationof capillary condensation of a solid.* Physical Review Letters, 2001. **86**(17): p. 3807-3810.
26. Herbert, E., S. Balibar, and F. Caupin, *Cavitation pressure in water.* Physical review E, 2006.

27. Hamada, Y., K. Koga, and H. Tanaka, *Phase equilibria and interfacial tension of fluids confined in narrow pores.* Journal of Chemical Physics, 2007. **127**: p. 084908.
28. Coasne, B., et al., *Freezing of mixtures confined in silica nanopores: Experiment and molecular simulation.* Journal of Chemical Physics, 2010. **133**: p. 084701.
29. Mraw, S.C. and D.F. O'Roarke, *Water in poal pores: low-temperature heat capacity behavior of the moisture in wyodak coal.* Science, 1979. **31**: p. 901-902.
30. Christenson, H., *Confinement effects on freezing and melting.* Journal of Physics: Condensed Matter, 2001. **13**: p. R95-R133.
31. Pawlow, P., *Uber die Abhängigkeit des Schmelzpunktes von der Oberflächenenergie eines festen Körpers.* Zeitschrift für Physikalische Chemie 1909. **65**: p. 545.
32. Bogdan, A., M. Kulmala, and N. Avramenko, *Reduction of enthaply of fusion and anamolies during phase transitions in finely divided water.* Physical Review Letters, 1998. **81**(5): p. 1042-1045.
33. Mu, R. and V.M. Malhotra, *Effects of a surface and physical confinementon the phase transitions of cyclohexne in porous silica.* Physical Review B, 1991. **44**: p. 4296-4303.
34. Roduner, E., *Size matters: why nanmaterials are different.* Chemical Society Reviews, 2006. **35**: p. 583-592.
35. Lai, S.L., et al., *Size-Dependent Melting Properties of Small Tin Particles: Nanocalorimetric Measurements.* Physical Review Letters, 1996. **77**(1): p. 99-102.
36. Tolman, R.C., *The effect of droplet size on surface tension.* Journal of Chemical Physics, 1949. **17**(3): p. 333-337.
37. Hill, T.L., *Thermodynamics of Small Systems*. Frontiers in Chemistry. Vol. 1,2. 1963-1964: W.A Benjamin.
38. Tolman, R.C., *The effect of droplet size on surface tension.* The Journal of Chemical Physics, 1949. **17**: p. 333.
39. Reif, F., *Fundamentals of Statistical and Thermal Physics* 1965: mcGraw-Hill.
40. Kondepudi, D. and I. Prigogine, *Modern Thermodynamics*. 1998, West Sussex: John Wiley & Sons Ltd.

41. Anisimov, M.A., *Divergence of Tolman's length for a droplet near the critical point.* Physical Review Letters, 2007. **98**(3): p. 035702.
42. Findenegg, G.H., et al., *Freezing and Melting of Water Confined in Silica Nanopores.* ChemPhysChem, 2008. **9**(18): p. 2651-2659.
43. Endo, A., et al., *Characterization of Nonfreezable Pore Water in Mesoporous Silica by Thermoporometry.* Journal of Physical Chemistry, 2008. **112**(24): p. 9034-9039.
44. Jones, H., *The solid-liquid interfacial energy of metals: calculations versus measurments.* Materials Letters, 2002. **53**: p. 364-366.
45. Digilov, R.M., *Semi-empirical model for prediction of crystal melting interfacial tension.* Surface Science, 2004. **555**: p. 68-74.
46. *TRC Thermodynamic Tables: Hydrocarbons*, 1998, Thermodynamics Research Center, Texas A&M University.
47. Block, H., *Uberdie Volumenanderung beim Schmelzen von Kristallen und die Warme-Ausdehnung der Kristalle und ihrer Schmeltzen.* Zeitschrift für Physikalische Chemie, 1912. **78**: p. 385.
48. Dunning, W.J., in *Physics and Chemistry of the Organic Solid State*, D. Fox, Editor. 1963, Interscience: New York, New York.
49. Huffman, H.M., et al., *Low temperature thermodynamic properties of six isomeric heptanes.* Journal of Physical Chemistry, 1961. **65**(3): p. 495-503.
50. McCullough, J.P., et al., *The Low-Temperature Thermodynamic Properties of Napthalene, 1-Methylnapthalene, 2-Methylnapthalene, 1,2,3,4 Tetrahydronapthalene, trans-Decahydronapthalene and cis-Decahydronapthalene.* Journal of Physical Chemistry, 1957. **61**(8): p. 1105-1116.
51. Oliver, G.D., M. Eatin, and H.M. Huffman, Journal of American Chemical Society, 1948. **70**(4): p. 1502-1504.
52. information., S.
53. Lu, H.M. and Q. Jiang, *Size-Dependent Surface Energies of Nanocrystals.* Journal of Physical Chemistry B, 2004. **108**: p. 5617-5619.
54. Lei, A.L., et al., *The Tolman length: Is it positive or negative?* Journal of American Chemical Society, 2005. **127**: p. 15346-15347.

55. Crassous, J., E. Charlaix, and J.L. Loubet, *Capillary Condensation between High-Energy Surfaces. An Experimental study with a Surface Force Apparatus.* Europhysics Letters, 1994. **28**(1): p. 37.
56. Watts, R.J. and S.J. Strickler, *Fluorescence and Internal Conversion in Naphthalene Vapor.* Journal of Chemical Physics, 1966. **44**(6): p. 2423.
57. Pfeifer, P. and D. Avnir, *Chemistry in Noninteger Dimensions between 2 and 3 .1. Fractal Theory of Heterogeneous Surfaces.* Journal of Chemical Physics, 1983. **79**(7): p. 3558-3565.
58. Iwamatsu, M., *The surface tension and Tolman's length of a drop.* Journal of Physics: Condensed Matter, 1994. **6**: p. L173-L177.
59. Graziano, G., *Significance of the Tolman length at the molecular level.* Chemical Physics Letters, 2010. **497**: p. 33-36.
60. Jones, H., *The solid-liquid interfacial energy of metals: calculations versus measurements.* Materail letters, 2002. **53**: p. 364-366.
61. Digilov, R.M., *Semi-empirical model for prediction of crystal-melt interfacial tension.* Surface Science, 2004. **555**(1-3): p. 68-74.
62. Dunning, W.J., *Physics and chemistry of the organics solid state*. Vol. 1. 1963, New York: Interscience Publishers.
63. Oliver, G.D., M. Eaton, and H.M. Huffman, *The heat capacity, Heat of fusion and Entropy of Benzene.* Journal of the American chemical society, 1948. **70**(4): p. 1502-1505.
64. ThermodynamicsResearchCenter, *TRC thermodynamics tables: Hydrocarbons*. Vol. 1. 1986: Thermodynamic Reseach Center, Texas Engineering Experiment Station, The Texas A&M University System.
65. Huffman, H.M., et al., *Low temperature thermodynamic properties of six isomeric heptane.* The Journal of Physical Chemistry, 1961. **65**(3): p. 495-503.
66. McCullough, J.P., et al., *The low-temperature thermodynamic properties of naphthalene, 1-methylnaphthalene, 2-methylnaphthalene, 1,2,3,4-tetrahydronaphthalene, trans-decahydronaphthalene and cis-decahydronaphthalene.* The Journal of Physical Chemistry, 1957. **61**(8): p. 1105-1116.

67. Block, H., *Uberdie Volumenanderung beim Schmelzen von Kristallen und die Warme-Ausdehnung der Kristalle und ihrer Schmeltzen.* Zeitschrift fur Physikalische, 1912. **78**: p. 385.
68. Pruppacher, H.R. and J.D. Klett, *Microphysics of Clouds and Prescription*. 1978, Dordrecht:Holland/Boston:USA, London:England: D.Reidel Publishing Company.
69. Jackson, F.I., *The death of Mozart.* J R Soc Med, 1990. **83**(12): p. 813.
70. Laby, T.H. and G.W.C. Kaye, *Tables of Physical and Chemical Constants and some mathematical functions (Kaye & Labys)*. 16 ed. 1995, Harlow, Essex, England: Longman Scientific &Technical.
71. Crassous, J., E. Charlaix, and J.-L.Loubet, *Capillary Condensation between Heigh-Energy Surfaces. An Experimental Study with a surface force apparatus.* Europhysics letters, 1994. **28**(1): p. 37.
72. Watts, R.J. and S.J. Strickler, *Fluorscence and Internal Conversion in Naphthalene Vapor.* The Journal of Chemical Physics, 1966. **44**(6): p. 2423.
73. Graziano, G., *On the size dependence of hydrophobic hydration.* Journal of the Chemical Society, Faraday Transactions, 1998. **94**: p. 3345-3352.
74. Endo, A., et al., *Charaterization of Nonfreezable Pore Water in Mesoporous Silica by Thermoporometry.* Journal of Physical Chemistry C, 2008. **112**(24): p. 9034-9039.
75. Lu, H.M. and Q. Jiang, *Size-Dependent Surface Tension and Tolman's length of Droplets.* Langmuir, 2005. **21**: p. 779-781.
76. Bowen, H.J.M., J. Donohue, and D.G. Jenkin, *Table of interatomic distances and configuration in molecules and ions*, ed. L.E. Sutton, A.D. Mitchell, and L.C. Cross. 1958, London: The chemical society.
77. Shin, J.-H., J.-Y. Parlange, and M. Deinert, *Scale effects in the latent heat of melting in nanopores.* Journal of Chemical Physics, 2013. **139**: p. 044701.
78. Nowak, D., et al., *Thermodynamic and kinetic supercooling of a liquid in a wedge pore.* Journal of Chemical Physics, 2008. **129**: p. 154509.
79. Sahouli, B., S. Blacher, and F. Brouers, *Fractal surface analysis by using nitrogen adsoprtion data: The case of the capillary condensation regime.* Langmuir, 1996. **12**: p. 2872-2874.

80. Lai, S.L., J.R.A. Carlsson, and L.H. Allen, *Melting point depression of Al clusters generated during the early stages of film growth: Nanocalorimetry measurements.* Applied Physics Letters, 1998. **72**(9): p. 1098-1100.
81. Schebarchov, D. and S.C. Hendy, *Superheating and solid-liquid phase coexistence in nanoparticles with nonmelting surfaces.* Physical Review Letters, 2006. **96**: p. 256101.
82. Sun, J. and S.L. Simon, *The melting behavior of aluminum nanoparticles.* Thermochimica Acta, 2007. **463**(1-2): p. 32-40.
83. Zhang, M., et al., *Size-dependent melting point depression of nanostructures: Nanocalorimetric measurements.* Physical Review B, 2000. **62**(15): p. 10548-10557.
84. Eckert, J., et al., *Melting behavior of nanocrystalline aluminum powders.* Nanostructured materials, 1993. **2**: p. 407-413.
85. Jiang, Q. and H.M. Lu, *Size dependent interface energy and its applications.* Surface Science Reports, 2008. **63**: p. 427-464.
86. Defray, R. and I. Prigogine, *Surface tension and adsorption*. 1966, New York, New York: Wiley.
87. See supplemental material.
88. Sarou-Kanian, V., F. Millot, and J.C. Rifflet, *Surface tension and density of oxygen-free liquid aluminum at high temperature.* International Journal of Thermodynamics, 2003. **24**(1): p. 277-286.
89. Passerone, A., E. Ricci, and R. Sangiorgi, *Influence of oxygen contaimination on the surface tension of liquid tin.* Journal of Materials Science, 1990. **25**: p. 4266-4272.
90. Tyson, W.R. and W.A. Miller, *Surface free energies of solid metals: estimation form liquid srface tension measurements.* Surface Science, 1977. **62**: p. 267-276.
91. Jeurgens, L.P.H., et al., *Thermodynamic stability of amorphous oxide films on metals: Application to aluminum oxide films on aluminum substrates.* Physical Review B, 2000. **62**(7): p. 4707-4719.
92. McHale, J.M., et al., *Surface energies and thermodynamic phase stability in nanocrystalline aluminas.* Science, 1997. **277**: p. 788-791.

93. Nikolopoulos, P., *Surface, grain-boundary and interfacial energies in Al2O3 and Al2O3-Sn, Al2O3-Co systems.* Journal of Materials Science, 1985. **20**: p. 3993-4000.
94. Chatain, D., L. Coudurier, and N. Eustathopoulos, *Wetting and interfacial bonding in ionocovalent oxide-liquid metal systems.* Revue de Physique Appliquee, 1988. **23**: p. 1055-1064.
95. Hoang, V.V., *Molecular dynamics study on structure and properties of liquid and amorphous Al2O3.* Physical Review B, 2004. **70**: p. 134204.
96. Assael, M.J., et al., *Reference data for the density and viscosity of liquid aluminum and liquid iron.* Journal of Physical Chemistry Reference Data, 206. **35**: p. 285-300.
97. Assael, M.J., et al., *Reference Data for the Density and Viscosity of Liquid Aluminum and Liquid Iron.* Journal of Physical Chemistry Reference Data, 2006. **35**: p. 285.
98. *Comprehensive Inorganic Chemistry*, ed. J.C. Bailar, et al. Vol. 4. 1973, New Jergy: Pergamon.
99. *Gmelin handbook of inorganic chemistry*. 1934, Berlin, Germany: Verlag Chemie.
100. Alchagirov, B.B. and A.M. Chochaeva, *Temperature dependence of the density of liquid tin.* High temperature, 2000. **38**(1): p. 48-52.
101. Nayar, A., *The Metal Databook*. 1997, New York: McGraw-Hill Co.
102. Wronski, C.R.M., *The size dependence of the melting point of small particles of tin.* British Journal of Applied Physics, 1967. **18**: p. 8.
103. *CRC handbook of Chemistry & Physics*. 87th ed, ed. D.R. Lide. 2006: CRC press.
104. Chatain, D., L. Coudurier, and N. Eustathopoulos, *Wetting and interfacial bonding in ioncovalent oxide-liquid metal systems.* Revue de Physique Appliquee, 1988. **23**: p. 1055-1064.
105. Sarou-Kanian, V., F. Millot, and J.C. Rifflet, *Surface Tension and Density of Oxygen-Free Liquid Aluminum at High temperature.* International Journal of Thermophysics, 2003. **24**(1): p. 277.
106. Slater, J.C., *Atomic Radii in Crystals.* The Journal of Chemical Physics, 1964. **41**(10): p. 3199.

107. Hasnaoui, A., et al., *Molecular dynamics simulations of the nano-scale room-temperature oxidation of aluminum single crystals.* Surface science, 2005. **579**: p. 47-57.
108. Buch, A., *Pure Metals Properties: Ascientific-Technical Handbook*, ed. A. International. 1999: ASM International
109. Ruff, O. and M. Konschak, Zeitschrift fuer Elektrochemie, 1926. **32**: p. 518.
110. Jeurgens, L.P.H., et al., *Thermodynamic stability of amorphous oxide films on metals: Application to aluminum oxide films on aluminum substrates.* Physical Review B, 2000. **62**(7): p. 4707.
111. McHale, J.M., et al., *Surface Energies and Thermodynamics Phase Stability in Nanocrystalline Aluminas.* Science, 1997. **277**: p. 788.
112. Das, R.N., A. Bandyopadhyay, and S. Bose, *Nanocreystalline α-Al2O3 Using sucrose.* Jounal of the American Ceramic Society, 2001. **84**(10): p. 2421.
113. Trunov, M.A., et al., *Effect of polymorphic phase transformations in Al2O3 film on oxidation kinetics of aluminum powders.* Combustion and Flame, 2005. **140**: p. 310-318.
114. La Mer, V.K. and R. Gruen, *A direct test of Kelvin's equation connecting vapour presure and radius of curvature.* Transactions of the Faraday Society, 1952. **48**: p. 410-415.
115. Sundquivst, H., *A parameterization scheme for non-convective condensation including prediction of cloud water content.* Quarterly Journal of the Royal Meteorological Society, 1978. **104**: p. 677-690.
116. Fairall, C.W., J.D. Kepert, and G.J. Holland, *The effect of sea spray on surface energy transport over teh ocean.* The Global Atmosphere and Ocean System, 1994. **2**: p. 121-142.
117. Milly, P.C.D., *Potential Evaporation and Soil Moisture in General Circulation Models.* Journal of Climate, 1992. **5**: p. 209–226.
118. Holyst, R. and M. Litniewski, *Heat Transfer at the Nanoscale: Evaporation of Nanodroplets.* Physical Review Letters, 2008. **100**: p. 055701.
119. Andreas, E.L., *The temperature of evaporating sea spray droplets.* Journal of Atmospheric Sciences, 1995. **52**(7): p. 852-862.

120. Hock, C., et al., *Calorimetric Observation of the Melting of FreeWater Nanoparticles at Cryogenic Temperatures.* Physical Review Letters, 2009. **103**: p. 073401.
121. Shin, J.-H., J.Y. Parlange, and M. Deinert, *Effect of interfacial surface tension on the heat of vaporization in drops.* In review, 2011.
122. Rossi, M.P., et al., *Environmental Scanning Electron Microscopy Study of Water in Carbon Naopipes.* Nano Letters, 2004. **4**(5): p. 898-993.
123. Malyshenko, S.P. and D.O. Dunikov, *On the surface tension corrections in nonuniform and nonequilibrium liquid-gas systems.* International Jounal of Heat and Mass transfer, 2002. **45**: p. 5201-5208.
124. Kell, G.S., L. Haar, and J.S. Gallagher, *NBS/NRC Steam Tables. Thermodynamic and Transport Properties and Computer Programs for Vapor and Liquid States of Water in SI units*. 1984, Washington: Hemisphere Publishing Corporation.
125. D'Arrigo, J.S., *Screening of membrane surface charges by divalent cations: an atomic representation.* American Journal of Physiology, 1978. **235**: p. C109-C117.
126. Knoll, G.F., *Radiation Detection and Measurement*. 4th ed. 2010, Hoboken, NJ: John Wiley & Sons, Inc.
127. DiCarlo, D.A., *Stability of gravity-driven multiphase flow in porous media: 40 years of advancements.* Water resource research, 2013. **49**: p. 4531-4544.
128. Deinert, M., et al. *Real-time measurement of water profiles in a sand using neutron radiography*. in *Procedding of Hydrology Days*. 2002.
129. Selker, J., J.Y. Parlange, and S.T. Steenhuis, *Fingered Flow in Two Dimensions 2. Predicting Finger Moisture Profile.* Water Resources Research, 1992. **28**(9): p. 2523-2528.
130. Glass, R.J. and M.J. Nicholl, *Physics of gravity fingering of immiscible fluids within porous media: An overview of current understanding and selected complicating factors.* Geoderma, 1996. **70**(2-4): p. 133-163.
131. Selker, J., et al., *Fingered Flow in Two Dimensions 1. Measurement of Matric Potential.* Water Resources Research, 1992. **28**(9): p. 2513-2521.
132. Van Duijn, C.J., G.J.M. Pieters, and P.A.C. Raats, *Steady Flows in Unsaturated Soils Are Stable.* Transport in Porous Media, 2004. **57**: p. 214-244.

133. Dautov, R.Z., et al. *Simulation of two-dimensional gravity-driven unstable flow*. in *Proceedings of the XIV International Conference on Computation Methods in Water Resources*. 2002. Delft, Netherlands.
134. DiCarrlo, D.A., *Nonmonotonic travleing wave solutions of infiltration into porous media.* Water Resources Research, 2008. **44**.
135. Elliassi, M. and R.J. Glass, *On the continuum-scale modeling of gravity driven fingers with standard monotonic consituative relations and hysteretic equations of state.* Water Resources Research, 2001. **37**: p. 2019-2035.
136. Deinert, M.R., *Scale dependent energy conservation and its connection to flow field instability in porous media* Water Resources Research, 2014. **In press**.
137. Deinert, M., et al. *Real-time measurement of water profiles in sand using neutron radiography*. in *Hydrology Days*. 2002. Fort Collins, Colorado: AGU.
138. Deinert, M.R., et al., *Comment: On the continuum-scale modeling of gravity-driven fingers in unsaturated porous media: The inadequacy of the Richards equation with standard monotonic constitutive relations and hysteretic equations of state by Eliassi and Glass.* Water Resources Research, 2003. **39**: p. 1263.
139. Hoffman, R.L., *A study of the advancing interface. I. Interface shape in liquid-gas systems.* Journal of Colloid and Interface Science, 1975. **50**(2): p. 228-241.
140. Ertas, D. and M. Kardar, *Critical dynamics of contact line depinning.* Physical Review E, 1994. **49**: p. 2532-2535.
141. Stokes, J.P., M.J. Higgins, and A.P. Kushnicik, *Harmonic-generation as a probe of dissipation at a moving contact line.* Physical Review Letters, 1990. **65**: p. 1885-1888.
142. Weitz, D., et al., *Dynamic capillary pressure in porous media: origin of the viscous-fingering length scale.* Physical Review Letters, 1987. **59**(26): p. 2967-2970.
143. Morrow, N.R., *Physics and thermodynamics of capillary action in porous media.* Industrial Engineering and Chemical Research, 1970. **62**: p. 32-56.
144. Stauffer, F., *Time dependence of the relationships between capillary pressure, water content and conductivity during drainage of porous media*, in *IAHR symp. On Scale Effects in Porous Media, IAHR*1978: Madrid, Spain.

145. Dahle, H.K., M.A. Celia, and S.M. Hassanizadeh, *Bundle of Tubes Model for Calculating Dynamic Effects in the Capillary Pressure Saturation Relationship.* Transport in Porous Media, 2005. **58**: p. 5-22.
146. Brooks, R.H. and A.T. Corey, *Hydraulic Properties of Porous Media*. Hydrology Papers. Vol. 3. 1964, Fort Collins, Colorado: Colorado State University.
147. Deinert, M.R., et al., *Measurement of fluid contents and wetting front profiles by real-time neutron radoigraphy.* Journal of Hydrology, 2004. **290**: p. 192-201.
148. Deinert, M.R., et al., *Measurement of fluid contents and wetting front profiles by real-time neutron radiography.* Journal of Hydrology, 2004. **290**: p. 192-201.
149. Deinert, M., et al., *Performance and calibration of a neutron image intensifier tube based real-time radiography system.* IEEE Transactions on Nuclear Science, 2005. **52**(2): p. 349-355.
150. Lago, M. and M. Araujo, *Capillary rise in porous media.* Journal of Colloid and Interface Science, 2001. **234**: p. 35-43.
151. Lu, T.X., J.W. Biggar, and D.R. Nielsen, *Water movement in glass bead porous media 1. Experiments of capillary rise and hysteresis.* Water Resources Research, 1990. **30**(12): p. 3275-3281.
152. Ghazanfari, M.H., et al., *Capillary pressure estimation using statistical pore size functions.* Chemical Engineering Technology, 2007. **30**(7): p. 862-869.
153. Ranabothu, S.R., C. Karnezis, and L.L. Dai, *Dynamic wetting: Hydrodynamic or molecular-kinetic?* Journal of Colloid and Interface Science, 2005. **288**: p. 213-221.
154. Olbricht, W.L., *Pore-scale prototypes of multiphase flow in porous media* Annual Review of Fluid Mechanics, 1996. **28**: p. 187-213.
155. Nimmo, J.R., *Porosity and pores size distribution*, in *Encyclopedia of Soils in the Environment*, D. Hillel, Editor 2004, Elsevier: London. p. 295-303.
156. Friedman, S.P., *Dynamic contact angle explanation of flow rate-dependent saturatio-pressure relationships during transient liquid flow in unsaturated porous media.* Journal of Adhesian Science and Technology, 1999. **13**(12): p. 1495-1518.
157. Genutchen, M.T.v., *A Closed-form Equation for Predicting the Hydraulic Conductivity of Unsaturated Soils.* Soil Science Society of Americal Journal, 1980. **44**: p. 892.